POLITECNICO
DI TORINO

Thesis title:

Multi-Sensor Flood Extent Mapping and FWDET-GEE Water-Depth Estimation in Google Earth Engine: The May 2023 Emilia-Romagna Flood

Supervisor:

Professor Piero Boccardo

Co-supervisors:

Marco Obialero

Sona Guliyeva

Tommaso Destefanis

Written by:

Reza Louni

S328212

2026

Contents

Chapter 1:
Introduction

1.1 Background and Context: Flood Risk and Disaster Risk Management (DRM)

Flooding is the most destructive natural hazard worldwide, causing significant economic, social, and environmental damage. Recent studies show that climate change, altered rainfall patterns, and landscape disturbances have increased both the frequency and severity of floods. Many European regions face a higher risk of flash flooding due to changing rainfall patterns and urban expansion(Bates et al., 2021; Cohen et al., 2018). A European Environment Agency study covering 1980 to 2020 found that flood damage exceeded €200 billion, highlighting Europe's ongoing vulnerability to extreme weather(EEA, 2023). Italy, with its densely populated floodplains, diverse climate, and complex river systems, is especially susceptible. The Emilia-Romagna region in northern Italy has a dense river network and an extensive alluvial plain where hydrological responses are rapid. Low-relief areas are particularly vulnerable, as water can rise quickly and spread during heavy rainfall. Effective flood management requires real-time monitoring tools capable of handling moderate rainfall events. Flood control involves four interconnected stages: recovery, response, preparedness, and prevention, all part of the Disaster Risk Management cycle. Preventive measures include maintaining existing flood defenses, proper land use, and implementing early warning systems. During floods, response actions involve situational monitoring, evacuation coordination, and rapid impact assessments. Recovery focuses on restoring affected systems and learning from past events to reduce future risks. Throughout all phases, timely and reliable information is essential for understanding flood dynamics and allocating resources effectively. Earth Observation (EO) satellites are increasingly crucial in providing such data. Since floods often occur during severe weather, when ground measurements are limited and conditions change rapidly, satellite imagery offers a consistent, unbiased overview of large areas. EO data support the DRM cycle by mapping flood hazards, monitoring hydrometeorological conditions, documenting inundations, and assessing post-event environmental changes. Open-access missions like the Copernicus Sentinel series, along with commercial high-resolution satellites, have expanded access to detailed geospatial data. Copernicus products, including satellite imagery, land monitoring, and emergency mapping services, provide standardized, accessible data used by researchers, civil protection agencies, and public institutions across Europe. This technological foundation underpins this study. Advances in radar, optical, and high-resolution satellite data, combined with cloud-based processing platforms, create new opportunities to observe flood dynamics with finer spatial detail and more consistent temporal coverage. Understanding how EO datasets can define flood extent and behavior is essential for improving monitoring methods and strengthening future flood risk management strategies.

1.2 Flood Mapping from Earth Observation Satellites

Earth Observation (EO) satellites have become an essential tool for flood monitoring because they offer repeated, wide-area coverage that does not rely on ground measurements. By capturing images before, during, and after a flood, EO data helps identify water presence, observe its changes, and pinpoint the most vulnerable areas as conditions evolve. Flood mapping mainly depends on two types of satellite sensors: radar and optical. Radar instruments, such as those on the Copernicus Sentinel-1 mission, transmit microwave signals that can penetrate clouds and operate independently of sunlight. This makes radar particularly useful during the early stages of a flood when heavy rain and cloud cover often block other observation methods. Flooded surfaces usually reflect radar energy away from the sensor, creating a darker signature that enables water detection even in adverse weather. Optical sensors, such as Sentinel-2 and commercial very-high-resolution satellites, record reflected sunlight across different wavelengths. These data provide detailed visual and spectral information that helps distinguish water from vegetation, bare soil, or built-up areas. However, optical satellites need clear skies, which limits their use during heavy rainfall or extended cloud cover. The difference between radar's all-weather capability and optical sensors' dependence on clear conditions is important when choosing datasets for flood mapping. Another key factor in flood monitoring is temporal consistency: floodwaters can rise, spread, or recede quickly, so the usefulness of satellite imagery depends not only on sensor capabilities but also on the timing of data collection. Having radar and optical observations taken in close temporal proximity enhances dataset comparison and helps develop a fuller understanding of flood dynamics. Because each sensor type offers distinct advantages, combining radar and optical data often yields more accurate flood maps. Radar enables continuous monitoring in cloudy or rainy weather, whereas optical imagery provides spatial detail and clarity when conditions are favorable. The growing availability of free satellite missions and advanced cloud-processing platforms has further expanded the role of EO in emergency response, environmental monitoring, and long-term flood risk assessment. These capabilities are central to the multi-sensor approach used in this thesis. Detailed analyses of sensor performance, timing, and methodological choices are presented in later chapters. However, the key point is that satellite observations provide a flexible and robust framework for understanding flood development across various landscapes.

1.3 3D Geospatial Data for Flood Mapping

Understanding how floods spread across the landscape requires not only identifying where water is present but also knowing how the underlying terrain influences its movement. For this reason, 3D geospatial data, primarily represented through Digital Elevation Models (DEMs), play a crucial role in flood analysis. These datasets depict the height and structure of the land surface, enabling researchers to estimate water flow, identify potential areas of accumulation, and determine which regions are naturally more vulnerable. The quality and resolution of elevation data significantly affect the accuracy of flood assessments. High-resolution DEMs obtained from airborne LiDAR, for example, can capture minor terrain variations that impact local drainage patterns, channel connectivity, and floodwater pathways. Conversely, coarser global DEMs may miss subtle topographic features, leading to errors in flow-direction determination or flood-extent estimation. This challenge is especially relevant in low-relief environments, such as the Emilia-Romagna floodplain, where even centimeter-scale elevation differences can influence how water spreads over large areas. Accurate terrain data is also vital for interpreting satellite-based flood maps. Radar and optical images display surface water but do not directly show depth or the topographic conditions that facilitate~~d~~ flooding. When combined with DEMs, however, Earth Observation (EO) data provide a more comprehensive understanding of flood behavior by linking surface water patterns to underlying terrain controls. Advances in data collection and processing from LiDAR campaigns to open-access global DEMs have greatly increased the availability of 3D information for hydrological applications. These resources support better flood mapping, risk assessment, and emergency planning, especially when integrated with multi-sensor satellite data. Later chapters of this thesis build on these ideas to examine how different elevation datasets influence flood extent interpretation and, ultimately, floodwater depth estimation.

1.4 Structure of the Thesis

This thesis is organized into six chapters, each addressing a key component of the study.

Chapter 1: Outlines the broader context of flood risk, the role of the Disaster Risk Management (DRM) cycle, and the importance of Earth Observation data for flood monitoring. It describes the study's motivation and presents the overall structure of the work.

Chapter 2: Provides the research motivation. It describes the characteristics of the Emilia-Romagna floodplain and summarizes the severe flood event that took place in May 2023. The chapter then identifies the main knowledge gaps in current flood-mapping practices and outlines the research questions and objectives that guide the thesis.

Chapter 3 reviews scientific literature on radar- and optical-based flood mapping, multi-sensor analysis, and terrain-dependent flood-depth estimation. It discusses the strengths and limitations of various approaches and explains how these insights shape the methodological choices made in this work.

Chapter 4: Presents the data and methods used in the study. It describes satellite imagery, ancillary datasets, and elevation models, and outlines the processing workflow used to generate flood-extent maps and water-depth estimates. The chapter also explains the accuracy-assessment procedures and how the tools used in the analysis are implemented.

Chapter 5: Reports and discusses the results. It compares the performance of multiple satellite sensors in mapping the May 2023 flood event and evaluates the role of DEM resolution in estimating floodwater depth. The findings are analyzed in relation to the research questions and their implications for operational flood monitoring.

Chapter 6 concludes the thesis by summarizing the primary outcomes, discussing their broader significance, and outlining possible directions for future research, including the integration of advanced modeling and data fusion approaches.

Chapter 2: Research motivation

2. The May 2023 Emilia-Romagna flood event and the CEMS EMSR664 Activation

In May 2023, the Emilia-Romagna region in northern Italy experienced a severe, rapidly developing flood event caused by an unusual sequence of persistent and intense rainfall episodes. The combination of saturated soils, rising river levels, and limited natural water-retention capacity led to widespread flooding across the regional plains. Rivers such as the Lamone, Savio, Montone, and Ronco overtopped their banks, producing extensive inundation that affected both urban areas and agricultural zones. Several municipalities in the provinces of Forlì-Cesena, Ravenna, and Rimini reported significant infrastructure damage, major disruptions to transportation networks, and the evacuation of thousands of residents. The scale and rapid evolution of the event made it one of the most impactful floods in the region's recent history. Due to the severity of the situation and the urgent need for timely, standardized geospatial information to support emergency response, the Copernicus Emergency Management Service (CEMS) was activated under activation code EMSR664. CEMS operates within the framework of the Copernicus Program, the European Union's Earth Observation initiative coordinated by the European Commission in cooperation with the European Space Agency and other partners. The Copernicus Program is structured around six core operational services, Land Monitoring, Marine Environment Monitoring, Atmosphere Monitoring, Climate Change, Security, and Emergency Management, each designed to provide open-access, satellite-based information tailored to specific societal and environmental needs. Within this structure, CEMS is dedicated to disaster risk management and delivers geospatial products to support preparedness, emergency response, and post-event recovery. Following the activation of EMSR664, CEMS produced a series of Rapid Mapping products derived from radar and optical satellite imagery acquired during the unfolding emergency. These flood delineation maps provided an operational overview of inundation extent and were used by national and regional authorities to coordinate emergency response activities and identify critical areas requiring immediate intervention. Because the CEMS Rapid Mapping component follows a standardized methodology and relies on multi-sensor observations, the resulting products also constitute a reliable and transparent reference for scientific evaluation and methodological comparison of flood-mapping approaches.

The May 2023 flood in Emilia-Romagna, therefore, represents a valuable case study for satellite-based flood monitoring. The region's flat topography and dense river network create conditions in which floodwaters can spread over large areas with relatively small elevation differences, making flood delineation particularly sensitive to sensor resolution and methodological choices. At the same time, the availability of multi-temporal satellite imagery, combined with authoritative CEMS flood delineation products, provides a strong and coherent basis for evaluating the performance of different Earth Observation datasets under comparable hydrological conditions. For these reasons, the EMSR664 activation offers a well-documented and consistent benchmark for assessing the accuracy and reliability of EO-based flood extent mapping in this study

2.2 Knowledge Gaps and Rationale

Despite significant advances in flood mapping and hydrological monitoring, several important gaps remain in the accurate, consistent, and transferable use of satellite data for flood detection and water-depth estimation. Open-access missions such as Sentinel-1 and Sentinel-2 have substantially increased the availability of flood-related observations, yet many operational and research workflows still rely on single-sensor analyses (DeVries et al., 2020; Mai Sy et al., 2023). Radar-based methods are particularly valued for their all-weather and day–night imaging capability but can misinterpret signals in urban or densely vegetated areas due to double-bounce effects and volume scattering (Moharrami et al., 2021). Optical systems such as Sentinel-2 provide greater spectral detail for distinguishing water, soil, and vegetation, but are often limited by cloud cover during critical flood phases (Farhadi et al., 2024a; Liou & Hoang, 2024).Although numerous studies have evaluated individual satellite systems for flood mapping, truly synchronous multi-sensor datasets remain uncommon, particularly those combining radar, multispectral optical, and very-high-resolution (VHR) observations within the same short temporal window of a flood event. Here, Very High Resolution (VHR) refers to spatial resolution rather than sensor type, as both radar and optical systems can operate at very fine ground sampling distances. According to the Copernicus spatial resolution classification, VHR imagery is categorized into two classes: VHR1 (≤ 1 m) and VHR2 (> 1 m to ≤ 4 m) (ESA, 2024). In this study, the 0.5 m dataset falls within the VHR1 category.

Although modern VHR satellite constellations provide on-demand tasking capabilities and rapid image acquisition when atmospheric conditions permit, the practical availability of temporally synchronized VHR data alongside open-access imagery remains limited. This limitation poses challenges for conducting systematic comparative analyses under equivalent hydrological conditions. Consequently, the relative performance of VHR products compared to open-access datasets has not yet been comprehensively evaluated within a consistent, event-based framework at the global scale. Another key gap concerns the integration of terrain information into flood-depth estimation. Terrain morphology strongly controls how floodwater flows, accumulates, and recedes, yet many flood-mapping studies continue to rely on coarse global elevation models such as SRTM (30 m) or MERIT (90 m) (Cohen et al., 2022).In low-relief regions such as the Po Valley and the wider Emilia-Romagna floodplain, small vertical inaccuracies can cause significant horizontal shifts in flood boundaries. Recent research shows that LiDAR-derived DEMs greatly improve vertical accuracy in depth estimation and hydrodynamic modeling (Ahmad et al., 2025; Teng et al., 2022a), but these datasets are rarely evaluated alongside multi-sensor flood maps. Additional uncertainty comes from the performance of the Flood Water Depth Estimation Tool (FWDET), a fast method for converting inundation polygons into continuous depth rasters without complex hydraulic models (Cohen et al., 2018, 2022). While widely used, FWDET's accuracy depends heavily on DEM resolution and the type of satellite sensor used to determine flood extent. Most evaluations have been done in North America and Asia (Das et al., 2023; Tran & Nguyen, 2025), leaving limited insight into its use in European lowlands like Emilia-Romagna. Recent work combining FWDET with high-resolution DEMs (Betterle & Salamon, 2024) shows promising improvements but has not yet been tested with multiple, synchronized satellite inputs. Cloud-based platforms like Google Earth Engine (Gorelick et al., 2017) enable large-scale, automated flood mapping; however, few studies have used these platforms to perform comprehensive, event-specific comparisons of radar, optical. Automated tools like GEE4Flood (2023) and Global Flood Mapper (2024) support near-real-time global monitoring, but their effectiveness depends on the chosen sensor configuration and classification algorithm. Recent research suggests that combining advanced spectral indices and machine-learning approaches can improve flood delineation (Liou & Hoang, 2024; Soria-Ruiz et al., 2022), though there is no consensus on the best way to balance automation, accuracy, and sensor-specific traits. Temporal consistency is another ongoing challenge. Floods change rapidly, and even small differences in satellite acquisition times can lead to mismatched flood boundaries and inconsistent depth estimations. Recent studies highlight the importance of aligning data collection across sensors: synchronizing Sentinel-1 and Sentinel-2 within a narrow interval improves mapping reliability, and combining remote sensing data with hydrological information helps reduce misclassification of water extent. The May 2023 Emilia-Romagna flood offers a unique opportunity to address these gaps. It is a representative European flood event with multi-sensor imagery from Sentinel-1, Sentinel-2, and SkySat, along with high-resolution LiDAR terrain data, all collected within a short, coherent time frame. Additionally, the availability of the CEMS EMSR664 Delineation 3 reference map enables an objective assessment of each sensor's performance under consistent hydrological conditions.

In this context, the present study focuses on three main knowledge gaps:

1. The limited availability of cloud-free HR and VHR optical data in the immediate aftermath of flood events.
2. the limited validation of DEM-dependent flood-depth estimation methods such as FWDET in European low-relief regions using LiDAR-based elevation models, and
3. the insufficient understanding of how sensor resolution and terrain models' accuracy jointly influence flood-extent delineation and water-depth estimation.

By addressing these gaps, the research aims to refine the integration of EO datasets within Copernicus and Google Earth Engine workflows, improving both the spatial accuracy of flood delineation and the vertical reliability of depth estimation. The goal is to contribute toward rapid, reproducible, and transferable satellite-based flood-monitoring methods suitable for managing the kind of emergencies.

2.2 Research Questions and Objectives

The research gaps identified earlier led to two main questions guiding this thesis. These questions examine the comparative performance of multi-sensor satellite imagery for flood mapping and how terrain model resolution affects water-depth estimation in low-relief floodplains like Emilia-Romagna.

RQ1. How accurately can Sentinel-1 SAR, Sentinel-2 optical, and SkySat very-high-resolution imagery delineate flood extent when analysed independently within Google Earth Engine and validated against the Copernicus CEMS EMSR664 Delineation 3 reference map?

This question addresses the limited empirical evidence comparing open-access and commercial satellite data under strictly synchronous flood conditions. Previous studies highlight the complementary strengths of radar and optical sensors, but their relative performance varies depending on spatial resolution, acquisition timing, and landscape characteristics. The rare availability of SkySat VHR imagery during the May 2023 Emilia-Romagna flood enables an evaluation of whether sub-metre imagery meaningfully improves detection accuracy and spatial detail in heterogeneous environments.

RQ2. How much do different elevation datasets, coarse global DEMs, and high-resolution LiDAR-derived DTMs impact the accuracy of water-depth estimates produced by the Flood Water Depth Estimation Tool (FWDET)?

This question emphasizes the vertical aspect of flood analysis. Existing research consistently demonstrates that DEM quality is a key factor in depth estimation, especially in low-relief areas where minor elevation differences influence water distribution. By using FWDET with both standard DEMs and LiDAR-derived terrain models, this study evaluates how topographic accuracy affects the reliability of water-depth mapping in flat alluvial regions. To address the research questions, this study pursues the following objectives:

- To systematically evaluate the ability of Sentinel-1 SAR, Sentinel-2 optical, and SkySat VHR imagery to delineate flood extent under synchronized hydrological conditions, using a consistent processing framework in Google Earth Engine.
- To evaluate the accuracy and reliability of each sensor's flood-extent map by comparing it with the Copernicus CEMS EMSR664 Delineation 3 reference, analyzing differences in spatial detail, omission and commission errors, and detection performance.
- To investigate how terrain model resolution affects water-depth estimation by using FWDET with both coarse global DEMs and high-resolution LiDAR-derived DTMs.
- To analyze the combined effects of sensor resolution and elevation accuracy on flood-extent mapping and depth estimation in low-relief environments such as the Emilia-Romagna floodplain.
- To offer methodological insights and recommendations for combining open-access and commercial satellite data with high-resolution terrain models in future European flood-monitoring workflows, especially within Copernicus and cloud platforms.

The study’s main goal is to develop a consistent and reproducible framework that measures how satellite features and terrain data quality together affect the accuracy of flood extent mapping and water depth estimation. In doing so, it helps improve rapid-mapping protocols in Europe and offers insights useful for both scientific research and operational flood risk management.

Chapter 3: Literature Review

3.1 Radar-Based Flood Mapping

Radar-based remote sensing has become a key component of satellite flood mapping because it enables consistent observations regardless of daylight and atmospheric conditions. Floods are often associated with heavy rainfall and persistent cloud cover, which significantly limit the effectiveness of optical sensors during the most critical flooding periods. Synthetic Aperture Radar (SAR) systems overcome these issues by actively transmitting microwave signals and receiving the reflected response from the Earth's surface, enabling flood detection under all weather conditions (DeVries et al., 2020; Lan & Wang, 2025). In this context, the Sentinel-1 mission of the Copernicus Program has become the central SAR platform for both operational and scientific flood monitoring. Most Sentinel-1 flood-mapping methods depend on the radiometric contrast between flooded and non-flooded areas. Open water bodies generally exhibit low backscatter due to specular reflection, whereas surrounding land cover produces more substantial and more varied returns. As a result, multi-temporal change-detection techniques, such as backscatter differencing or ratioing between pre-flood and post-flood images, form the basis of many radar-based flood mapping methods (Moharrami et al., 2021; Vekaria et al., 2023). These methods are usually combined with adaptive thresholding strategies to distinguish flooded pixels from background variability, balancing simplicity and reliability (Vanama et al., 2020). From a methodological perspective, different SAR processing strategies entail trade-offs. Backscatter differencing, as used by DeVries et al. (2020), emphasizes rapid execution and operational reliability, making it suitable for emergency response. On the other hand, ratio-based methods are less affected by changes in soil moisture or incidence-angle effects, thereby improving detection across diverse surface conditions (Vekaria et al., 2023). However, ratio methods can increase speckle noise and often need extra filtering steps, which may reduce spatial detail. An additional important distinction concerns single- and dual-polarization Sentinel-1 data. While many operational systems mainly rely on VV polarization due to its higher signal-to-noise ratio, research on agricultural floodplains shows that VH polarization is more sensitive to shallow or vegetation-covered floods (Ghouri et al., 2024). This heightened sensitivity can reduce missed detections in farmland but may also increase false alarms in rough or complex terrain. (Mai Sy et al., 2023) addressed this issue by combining VV and VH data with spatial filtering, resulting in improved performance in mixed urban-rural landscapes. Despite its benefits, radar-based flood mapping has some well-known limitations. In cities, double-bounce scattering between buildings and the ground can produce high backscatter, concealing flooded streets and courtyards and leading to systematic misses (Composto et al., 2025). In vegetated floodplains, volume scattering within crop canopies can conceal the radar signature of shallow flooding, especially early on (Ghouri et al., 2024). Wet soils after heavy rain may also exhibit reduced backscatter, similar to open water, increasing the risk of misclassification (Moharrami et al., 2021). These issues are particularly significant in low-relief areas like Emilia-Romagna, where subtle elevation differences and intensive land use complicate flood detection. To address these limitations, recent studies have explored improvements such as morphological filtering, the incorporation of additional data (e.g., land cover or slope), and the use of machine learning classifiers. (Composto et al., 2025) demonstrated that adding contextual variables into supervised models can significantly reduce missed detections in dense urban settings. However, these methods require additional training data and are less readily transferable across regions, limiting their use in rapid emergency mapping. Therefore, operational systems tend to prefer simpler, transparent SAR workflows that prioritize reliability and quick delivery over fine-scale accuracy (Hamidi et al., 2023; Meyer et al., 2022). Overall, the literature consistently confirms that Sentinel-1 SAR provides a robust foundation for flood extent mapping, particularly during active flood phases when optical data are unavailable (DeVries et al., 2020; Lan & Wang, 2025). At the same time, its shortcomings in urban and vegetated areas underscore the need for complementary data from optical and very-high-resolution sensors. These factors motivate a comparative multi-sensor evaluation framework in which radar-based flood maps are systematically compared with optical and VHR data under the same hydrological conditions. This approach directly guides the methodology used in this thesis.

3.2 Optical-Based Flood Mapping

Optical remote sensing has long been vital for flood mapping because it captures detailed spectral information related to surface water, soil moisture, vegetation, and urban areas. Multispectral satellite systems such as Sentinel-2 and Landsat provide high radiometric sensitivity across the visible, near-infrared (NIR), and shortwave infrared (SWIR) bands, enabling effective discrimination between flooded and non-flooded surfaces under clear-sky conditions. Unlike SAR systems, optical sensors do not rely on backscatter signals but instead leverage the strong absorption properties of water in the NIR and SWIR regions, which underpin most optical flood-detection methods (Mehmood et al., 2021; Shan et al., 2025). The most common optical flood-mapping techniques use spectral water indices, especially the Normalized Difference Water Index

(NDWI) and its variants. NDWI-based thresholding has proven reliable for flood delineation when cloud-free images are available shortly after flooding events (Shan et al., 2025; Tripathy & Malladi, 2022). However, studies show that traditional NDWI often struggles to distinguish shallow water from wet soil or saturated vegetation, particularly in agricultural floodplains. To address this, alternative indices incorporating Short-Wave Infrared (SWIR) bands have been developed. (Farhadi et al., 2024a, 2024b) demonstrated that custom spectral indices such as Flood/Water Extraction Index (FWEI) and Sentinel-2 Flood Mapping Index (SFMI) improve water soil separation and increase detection accuracy compared with Normalized Difference Water Index (NDWI)(S.K.McFEETERS,1996) and Modified Normalized Difference Water Index (MNDWI)(Xu, 2006), particularly in cropland-dominated areas. These findings highlight the potential of Sentinel-2's spectral capabilities to customize flood-mapping strategies by land-cover type. Beyond single-date flood mapping, dense optical time series enable detailed analysis of flood persistence and inundation patterns. (Liu et al., 2022) showed that multi-temporal Sentinel-2 images can track changes in inundation duration and hydroperiods, thereby supporting long-term monitoring of floodplains and wetlands. Similarly, Landsat-based studies find that combining multiple optical missions enhances the continuity of flood hazard assessments over longer periods (Mehmood et al., 2021). While these methods are less suitable for real-time emergency response, they provide valuable context for understanding flood recurrence and post-flood recovery. A key limitation of optical flood mapping is its reliance on cloud-free conditions, which often delays data collection during peak flooding. Several studies have therefore positioned optical imagery as a complementary, rather than primary, data source during flood emergencies(Lan & Wang, 2025) demonstrated that Sentinel-2 NDWI products are highly effective for validating SAR-derived inundation maps after cloud cover clears, improving boundary accuracy and reducing false detections. Similar conclusions were reached by Suab et al. (2022), who showed that Sentinel-2 refinement significantly enhances SAR-based flood products by distinguishing between permanent water bodies and temporary inundation. Advances in very high resolution (VHR) optical imagery have expanded the capabilities of optical flood mapping. Commercial platforms such as SkySat and PlanetScope offer sub-meter to a few-meter spatial resolution, enabling the detection of fine-scale inundation patterns that medium-resolution sensors cannot resolve. (Aati & Avouac, 2020) demonstrated that SkySat imagery achieves sub-meter horizontal accuracy and supports precise geometric reconstruction in floodplain environments. (Johansen et al., 2022)

Further showed that VHR optical data can capture rapid, localized water-level changes during short-duration floods, providing insights into flood propagation at parcel and infrastructure scales. These capabilities are beneficial for validating flood extents in heterogeneous landscapes and urban–agricultural mosaics, such as those in Emilia-Romagna. Despite their spatial detail, VHR optical datasets are constrained by narrower swath widths, higher costs, and lower revisit frequencies than those from open-access missions. As a result, their use has mainly been for post-event analysis and targeted validation rather than large-scale operational mapping (Kussul et al., 2023; Szabó et al., 2021). Machine-learning methods that integrate multispectral features show promise for improving optical flood detection, especially when combining data from multiple resolutions and sensors (Bentivoglio et al., 2022; Soria-Ruiz et al., 2022). However, these methods often require extensive training data and may be less interpretable, limiting their immediate use in rapid mapping scenarios. Overall, the literature indicates that optical satellite systems provide high spectral and spatial detail for flood delineation and impact assessment when atmospheric conditions permit observation. Sentinel-2 strikes an ideal balance between spatial resolution, spectral richness, and open access, making it suitable for regional-scale flood mapping and post-event analysis (Esposito & Ravanelli, 2024). Meanwhile, VHR optical imagery offers critical fine-scale information that complements both Sentinel-1 and Sentinel-2 products. These features support the inclusion of optical and VHR datasets as independent components within a multi-sensor framework, enabling a systematic assessment of their strengths and limitations under consistent hydrological conditions, as pursued in this thesis.

3.3 Multi-Sensor Comparison

While radar and optical satellite systems have independently demonstrated strong capabilities for flood mapping, recent literature increasingly emphasizes the importance of evaluating their relative performance under consistent hydrological conditions. Rather than focusing solely on sensor fusion, several studies emphasize the need for a systematic comparison across sensors to understand how acquisition modality, spatial resolution, and timing influence flood-detection accuracy. This distinction is crucial in operational contexts, where sensor selection often depends on data availability across different flood stages. Comparative analyses consistently show that radar-based approaches, especially those using Sentinel-1 SAR, provide the most reliable flood detection during active flooding, when cloud cover and precipitation limit optical observations.

Studies comparing Sentinel-1 and Sentinel-2 products indicate that SAR-derived flood maps typically capture most inundated areas at peak flood extent, although boundary accuracy is reduced in urban and vegetated areas (Lan & Wang, 2025; Suab et al., 2022). Conversely, optical maps derived from Sentinel-2 imagery tend to yield sharper flood boundaries and better discrimination between water and wet soil once cloud-free conditions return, making them particularly useful for post-event assessment and validation. Several authors have explicitly contrasted radar-only and optical-only flood products. (Lan & Wang, 2025) reported that Sentinel-2 NDWI maps increased overall accuracy by a few percentage points when used to validate Sentinel-1 classifications, mainly by reducing false positives and correcting boundary errors. Similarly, Gašparovič & Klobučar (2021) showed that optical indices effectively refine SAR-derived inundation masks in areas affected by radar artifacts, such as layover and shadow. These findings suggest that radar and optical sensors are not interchangeable but rather offer complementary views of flood extent, with their relative usefulness varying across the flood lifecycle. Spatial resolution is another key factor in multi-sensor comparison. Medium-resolution sensors like Sentinel-1 (10 m) and Sentinel-2 (10–20 m) are suitable for regional-scale flood mapping but may miss fine-scale inundation patterns in diverse landscapes. Very-high-resolution (VHR) optical imagery from platforms such as SkySat and PlanetScope can resolve narrow flow paths, flooded roads, and small agricultural parcels that remain unseen at coarser resolutions (Aati & Avouac, 2020; Johansen et al., 2022). Studies indicate that VHR imagery can significantly improve local flood delineation, especially in urban–agricultural mosaics, but its limited coverage and higher costs restrict its use for large-area mapping. Importantly, several studies warn that higher spatial resolution does not automatically mean better flood mapping. (Kussul et al., 2023) found that VHR optical imagery improved detection only when paired with suitable spectral features and classification strategies. Likewise, (Szabó et al., 2021) noted that increased spatial detail can boost classification noise if not carefully filtered or contextualized. These findings highlight the need to evaluate sensor performance based on both spatial resolution and methodological robustness, not just resolution alone. Temporal alignment among datasets is also a crucial factor in multi-sensor comparison. Floodwaters can change rapidly, and even short delays between acquisitions may cause apparent differences between sensor-derived maps. Studies comparing radar and optical flood products show that timing mismatches can lead to significant differences in flood extent detection, regardless of sensor performance (Esposito & Ravanelli, 2024; Lan & Wang, 2025). Therefore, analyses using consistently timed datasets are vital for isolating sensor effects from hydrological variability. Overall, the literature indicates that no single sensor is universally best for flood mapping. Radar offers robustness and timeliness, optical provides spectral clarity and boundary accuracy, and VHR imagery delivers detailed local information. Instead of promoting a single “best” method, recent research favors comparative evaluation frameworks that assess how various sensors perform under the same conditions and processing environments. This approach aligns with the current study's goal of systematically comparing flood extents derived from Sentinel-1, Sentinel-2, and SkySat images acquired within a narrow time window during the May 2023 Emilia-Romagna flood. By focusing on comparison rather than fusion, this work aims to highlight the strengths, limitations, and trade-offs of each sensor type. Such analysis provides a transparent basis for selecting appropriate data sources for flood response and post-event analysis. It sets the stage for exploring how sensor-derived flood maps relate to terrain representation in floodwater-depth estimation, as discussed next.

3.4 LiDAR

While flood-extent mapping provides essential information on the spread of flooding, accurately estimating flood-water depth depends on a reliable representation of terrain shape. The topography influences how floodwaters move across the landscape, and Digital Elevation Models are therefore crucial for accurate depth measurement. This is especially true in low-relief floodplains, where small vertical errors in elevation data can lead to large horizontal shifts in flood boundaries and unrealistic depth estimates. Early flood-depth studies often used global DEMs like the Shuttle Radar Topography Mission (SRTM) DEM(Farr et al., 2007) and the Multi-Error-Removed Improved-Terrain (MERIT) DEM(Yamazaki et al., 2017) because they offer wide coverage and are easy to access. These datasets allowed for flood analysis at continental and global scales but have limitations due to coarse spatial resolution and vertical uncertainty. Several comparative studies found that such DEMs smooth out detailed terrain features, resulting in less accurate flood connectivity and depth estimates over flat areas (Ahmad et al., 2025; Cohen et al., 2022). In places like the Po Plain in Emilia-Romagna, even decimetre-level elevation errors can cause significant distortions in flood-depth patterns. To address these issues, the Flood Water Depth Estimation Tool (FWDET) was developed by (Cohen et al., 2018) as an efficient method for converting flood-extent polygons into continuous water-depth rasters using a DEM as the primary input (Cohen et al., 2018). FWDET estimates water depth by interpolating water-surface elevations from the flood boundary inward, thereby avoiding the need for complex hydrodynamic models. Its simplicity makes FWDET well-suited to large-scale and rapid-response applications in which speed and reproducibility are key. Follow-up evaluations consistently show that FWDET's accuracy depends heavily on the quality of the elevation model. (Cohen et al., 2022) showed that replacing SRTM-based DEMs with LiDAR data cut depth-estimation errors by more than half in multiple tests. Similarly, Das, Jensen et al. (2023) combined Sentinel-1 inundation masks with a 5 m LiDAR Digital Terrain Model (DTM), achieving sub-meter agreement with real water levels. These studies suggest that FWDET itself is not the limiting factor; rather, the accuracy of flood-depth estimates is controlled by terrain representation, especially in flat floodplains. The Digital Terrain model (DTMs) provides a major improvement over global elevation products by capturing fine details such as levees, drainage channels, and subtle elevation changes that influence floodwater movement and retention. Reviews of multiple flood-depth studies consistently show that LiDAR-based terrain models have the lowest vertical errors and produce the most realistic depth patterns, particularly in agricultural and urban floodplains (Ahmad et al., 2025; Wedajo, 2017). In contrast, coarse DEMs tend to oversimplify terrain, creating artificially smooth and exaggerated flood-depth maps. Recent research also highlights that flood-depth uncertainty results from the interaction between flood-extent accuracy and DEM resolution. In low-slope areas, small errors in satellite-derived flood boundaries can lead to large errors in depth when combined with coarse elevation models (Teng et al., 2022a). This sensitivity underscores the importance of assessing flood-extent mapping and depth estimation jointly rather than separately. Hybrid methods that combine SAR- or optical-based inundation masks with LiDAR terrain data have emerged as effective compromises between physical accuracy and computational speed (Das et al., 2023). Several studies have proposed expanding FWDET by adding extra constraints or data-driven improvements. (Bryant et al., 2022) showed that interpolating water levels from known river elevations improves depth continuity. In contrast, (Liou & Hoang, 2024) demonstrated that machine-learning models combining SAR backscatter features with DEM metrics can reduce depth errors relative to FWDET alone. Although these approaches improve accuracy, they also increase complexity and data requirements, which may limit their use in rapid operational settings. Recent work has increasingly used cloud computing platforms, such as Google Earth Engine, to run FWDET and DEM-based workflows. Cloud platforms enable efficient processing of large flood extents by combining satellite-inundation masks with multiple elevation datasets without requiring local computing resources. (Cohen et al., 2022; Das et al., 2023) showed that FWDET performs well in cloud-based workflows, enabling rapid testing of different DEM resolutions and flood scenarios. Cloud computing also improves reproducibility, facilitates sensitivity analysis, and supports operational scalability important for Copernicus flood-monitoring projects. Overall, the literature indicates that accurate floodwater depth estimation largely depends on terrain modeling, particularly in flat floodplains such as Emilia-Romagna. LiDAR-derived DTMs substantially improve FWDET's performance relative to global DEMs, yielding more realistic and reliable depth estimates. At the same time, depth accuracy remains closely linked to the quality and timing of satellite flood extent data. These findings support the approach used in this study, which evaluates FWDET using flood maps from various satellite sensors and compares depth estimates derived from global DEMs and high-resolution LiDAR DTMs within a consistent cloud-based processing system.

3.5 Google Earth Engine (GEE) applications for hydrological monitoring

The increasing availability of Earth Observation data has fundamentally transformed how hydrological processes are monitored and analyzed. Modern flood studies increasingly depend on extensive satellite archives, multiple sensor types, and frequent observations, which demand processing environments capable of efficiently handling large data volumes. In this context, Google Earth Engine (GEE) has become a widely adopted cloud-based platform for hydrological applications, providing direct access to long-term satellite records, global ancillary datasets, and scalable computing resources within a single unified environment. These features make GEE particularly suitable for studying hydrological phenomena that change dynamically in space and time, such as surface-water fluctuations, flood events, and landscape responses after flooding. In hydrological research, GEE is extensively used to support the systematic analysis of surface-water extent, inundation dynamics, and temporal variability. By providing access to dense time series from the Sentinel-1 SAR and Sentinel-2 optical missions, the platform enables continuous monitoring of water bodies across various atmospheric and seasonal conditions. Radar-based workflows benefit from GEE's ability to efficiently process large SAR archives, enabling multi-temporal change-detection approaches that are essential for tracking flood onset, peak conditions, and recession phases, particularly when clouds obscure optical imagery (DeVries et al., 2020;

Hamidi et al., 2023). Optical-based analyses leverage GEE's built-in cloud masking, compositing, and spectral-index tools to study surface-water patterns and post-flood impacts once clear-sky observations are available. Beyond simple flood delineation, GEE increasingly supports the integration of satellite-derived inundation maps into a broader hydrological context. Several studies combine flood-extent products with precipitation data, land-cover information, soil-moisture proxies, and elevation models to improve interpretation of flood processes and support hydrological decision-making (Chen & Zhao, 2022; Slagter et al., 2020). Integrating these diverse datasets within a consistent spatial and temporal framework enhances understanding of how rainfall, terrain, and land use collectively influence flood behavior. One of GEE's main advantages for hydrological monitoring is its support for reproducible and scalable workflows. Analysis scripts can be applied consistently across different regions and time periods, enabling comparisons between events or sensors without variations in preprocessing or analytical steps. This consistency is particularly important for comparative and operational studies, where controlling for sensor characteristics, acquisition timing, or terrain representation is critical. Several large-scale flood-monitoring frameworks demonstrate that GEE-based workflows significantly reduce processing time while maintaining reliable accuracy, making them suitable for near-real-time emergency applications (Ahmed et al., 2025; Vanama et al., 2020). GEE also facilitates the integration of satellite-derived flood products with elevation data and downstream hydrological models. Combining flood-extent maps with multiple DEM sources within the same cloud environment allows systematic assessment of how terrain resolution influences hydrological metrics like water depth and flood volume. This capability is especially important in low-relief floodplains, where small vertical differences in elevation can cause large changes in flood extent and depth. Cloud-based processing additionally supports sensitivity testing and scenario analysis that would be computationally intensive in traditional desktop workflows. Despite these benefits, the literature highlights that effective GEE use in hydrological monitoring requires careful methodological planning. Fully automated workflows may oversimplify local hydrodynamics, and generic thresholds or classifiers might not accurately capture region-specific characteristics, especially in urbanized or vegetated floodplains. Therefore, several studies emphasize the importance of event-specific parameter selection and independent validation using authoritative reference datasets to ensure the reliability and interpretability of GEE-derived hydrological products (Betterle & Salamon, 2024; Composto et al., 2025). Overall, Google Earth Engine offers a powerful and flexible platform for hydrological monitoring by allowing multi-sensor data integration, large-scale time-series analysis, and reproducible processing within a cloud-based environment. Its broad use in flood and surface-water studies underscores its suitability for both scientific research and operational applications. In this thesis, GEE acts as the common processing environment through which radar, optical, and elevation datasets are consistently analyzed, supporting an objective assessment of flood extent and water-depth estimation during the May 2023 Emilia-Romagna flood.

Chapter 4: Materials and Methods

4.1 Study Area

The study area is situated in the Emilia–Romagna region of northern Italy, which experienced severe flooding during the May 2023 hydrometeorological event. Emilia–Romagna is characterized by a large alluvial plain that extends from the Apennine Mountains to the Adriatic coast and is traversed by numerous rivers and artificial canals, making it highly prone to flooding. The regional context and the specific Area of Interest (AOI) selected for this thesis are illustrated in Figure 4-1. In this regional setting, the AOI focuses on the municipality of Ravenna, located in the northeastern part of Emilia–Romagna at approximately 44.42°N, 12.20°E. Ravenna lies about 8 to 10 kilometers inland from the Adriatic Sea and is connected to the coast via the Candiano Canal. The city has an estimated population of around 156,000 residents, making it one of the largest urban centers in the region. The surrounding terrain features low-lying areas, minimal elevation variation, and a mix of agricultural, peri-urban, and industrial land uses. Hydrologically, the area is crossed by several rivers, including the Montone, Ronco, and Lamone, which converge near Ravenna before flowing into the Adriatic Sea. The combination of flat terrain, regulated waterways, and intense rainfall during the 2023 event led to widespread surface water accumulation and flooding in this area. These features make Ravenna an ideal location for testing flood-mapping algorithms and water-depth estimation techniques using multi-sensor satellite data. The AOI with an area of 79264740 m^2 (79.2 km^2) used in this study corresponds to the spatial overlap of all satellite datasets (Sentinel-1, Sentinel-2, and SkySat) and was mapped during the emergency by the Copernicus Emergency Management Service (CEMS). This approach ensures methodological consistency and enables reliable comparison between satellite-derived flood maps and authoritative reference data.

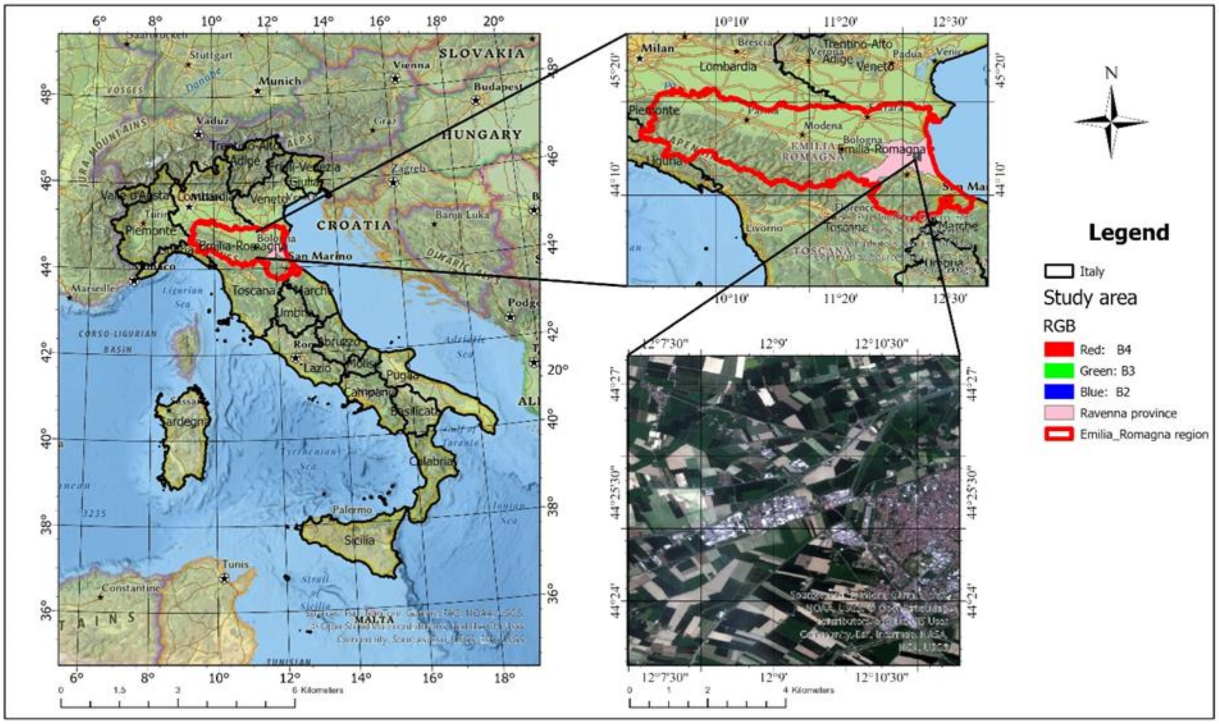

Figure 4-1 Study area: the Emilia–Romagna region, Ravenna province

4.2 Datasets and Tools

This study combines multi-sensor satellite imagery, high-resolution elevation models, and authoritative flood-delineation data to map the 2023 Emilia–Romagna flood and estimate water depth. All processing steps were carried out using Google Earth Engine (GEE), which offers direct access to global satellite archives and cloud-based computational resources, enabling an efficient and reproducible workflow.

4.2.1 Sentinel-1 SAR

Sentinel-1 is a C-band Synthetic Aperture Radar (SAR) mission operated by the European Space Agency under the Copernicus Programme. Thanks to its all-weather and day–night imaging capabilities, Sentinel-1 is widely used for rapid flood assessment, particularly when cloud cover prevents the use of optical sensors. In SAR imagery, open water typically appears as very dark pixels due to specular reflection, especially in VH polarization, making it a reliable indicator for flood mapping. In this study, pre-event and post-event Sentinel-1 Interferometric Wide (IW) Ground Range Detected (GRD) images were obtained directly through the Google Earth Engine (GEE) platform. GEE provides access to the full Sentinel-1 archive, enabling efficient filtering of acquisitions by date, orbit direction, polarization, and geographic region. The selected pre-event image, acquired on April 28, 2023, represents baseline conditions prior to flooding, while the post-event image, acquired on May 23, 2023, corresponds to the period when inundation was observed. These two images are shown in Figures 4-2 and 4-3, respectively. The main technical characteristics of the Sentinel-1 dataset used in this study, including spatial resolution, revisit time, acquisition mode, polarization, and processing level, are summarized in Table 4-1.

Table 4-1 – Technical characteristics of the Sentinel-1 SAR dataset

Feature	Description
Mission	Sentinel-1A / Sentinel-1B
Operator	European Space Agency (ESA) under the Copernicus Programme
Sensor type	C-band Synthetic Aperture Radar (SAR)
Central frequency	5.405 GHz (C-band)
Acquisition mode	Interferometric Wide Swath (IW)
Product type	Ground Range Detected (GRD)
Polarization	VH (cross-polarization)
Spatial resolution	~10 m (ground range)
Swath width	~250 km
Revisit time	~6 days (combined constellation)
Imaging capability	Day-night, all-weather
Processing level	Level-1 GRD
Access platform	Google Earth Engine (GEE)

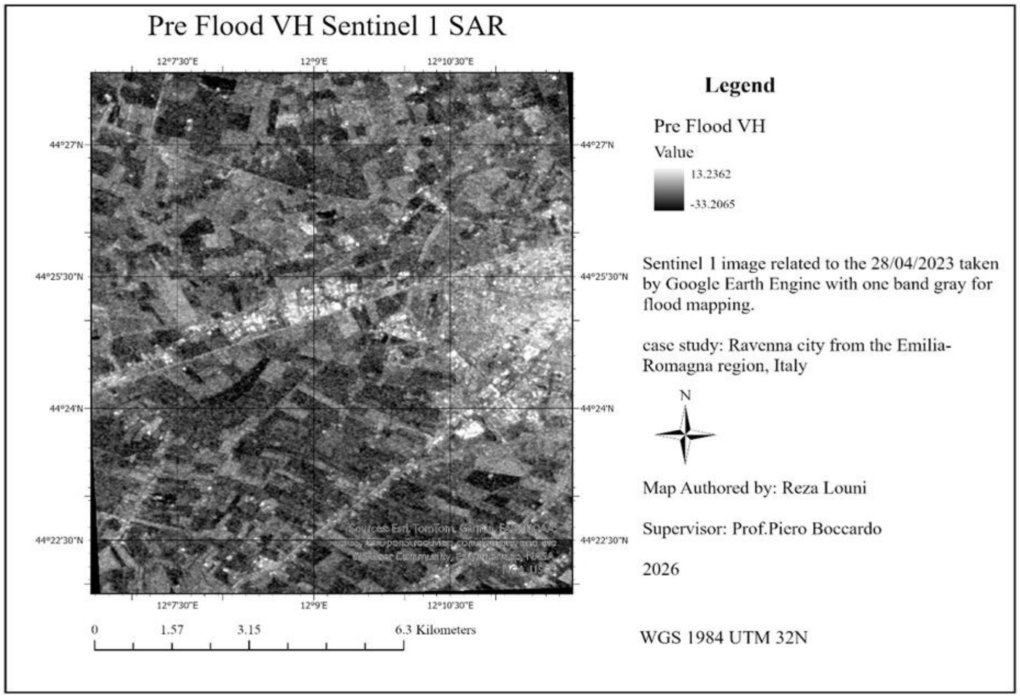

Figure 4-2. Pre-flood Sentinel-1 VH SAR image acquired on 28 April 2023, showing baseline backscatter conditions over the study area.

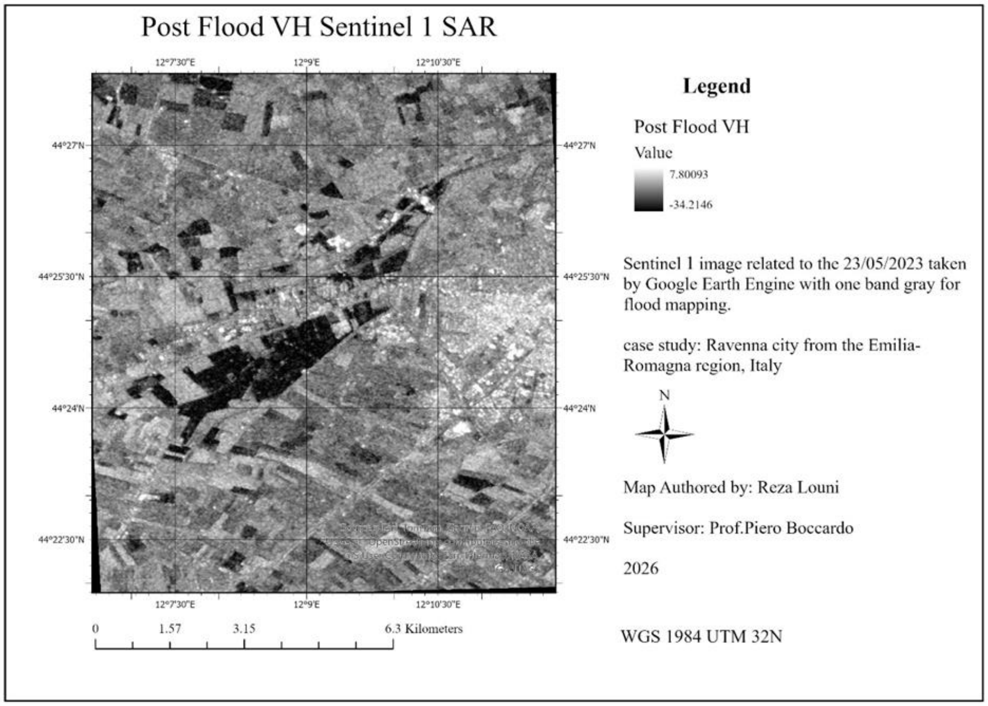

Figure 4-3. Post-flood Sentinel-1 VH SAR image acquired on 23 May 2023, showing reduced backscatter associated with flooded areas.

4.2.2 Sentinel-2

Sentinel-2 is an optical multispectral mission operated under the Copernicus Programme, equipped with the MultiSpectral Instrument (MSI), which captures high-resolution imagery across 13 spectral bands. Its 10-meter visible and near-infrared bands make Sentinel-2 particularly well suited for monitoring surface water conditions. Flooded areas can be effectively identified using spectral indices such as the Normalized Difference Water Index (NDWI), in which water typically exhibits high reflectance in the green band and strong absorption in the near-infrared (NIR) region. The Sentinel-2 constellation provides a global revisit frequency of approximately 5 days at the equator, which allows frequent observation of flood evolution when cloud-free conditions are available. In this study, pre-event and post-event Sentinel-2 Level-2A images were obtained directly from the Google Earth Engine (GEE) platform. The pre-event image, acquired on April 28, 2023, represents baseline land-surface conditions prior to inundation, while the post-event image, acquired on May 23, 2023, captures conditions immediately after peak flooding. These two scenes are displayed in Figures 4-4 and 4-5, respectively. The main spectral characteristics of the Sentinel-2 MSI sensor, including band wavelengths and corresponding spatial resolutions, are summarized in Table 4-2.

Table 4-2 – Sentinel-2 MSI spectral bands and spatial resolution

Band	Band name	Central wavelength (nm)	Bandwidth (nm)	Spatial resolution (m)	Typical use
B1	Coastal aerosol	443	20	60	Atmospheric correction
B2	Blue	490	65	10	Water, atmospheric effects
B3	Green	560	35	10	Water mapping (NDWI)
B4	Red	665	30	10	Vegetation, land cover
B5	Red Edge 1	705	15	20	Vegetation analysis
B6	Red Edge 2	740	15	20	Vegetation analysis
B7	Red Edge 3	783	20	20	Vegetation analysis

Band	Band name	Central wavelength (nm)	Bandwidth (nm)	Spatial resolution (m)	Typical use
B8	NIR	842	115	10	Water detection, NDWI
B8A	Narrow NIR	865	20	20	Vegetation monitoring
B9	Water vapor	945	20	60	Atmospheric correction
B10	SWIR, Cirrus	1375	30	60	Cloud masking
B11	SWIR 1	1610	90	20	Water, soil moisture

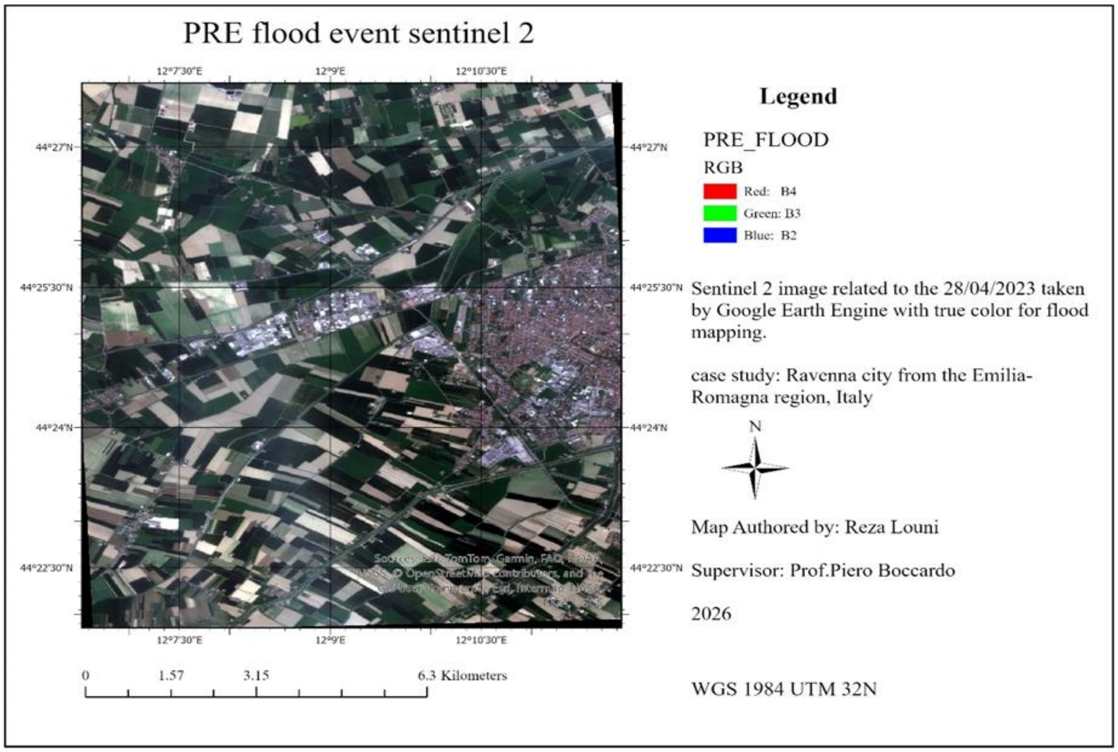

Figure 4-4 Pre-flood event Sentinel 2

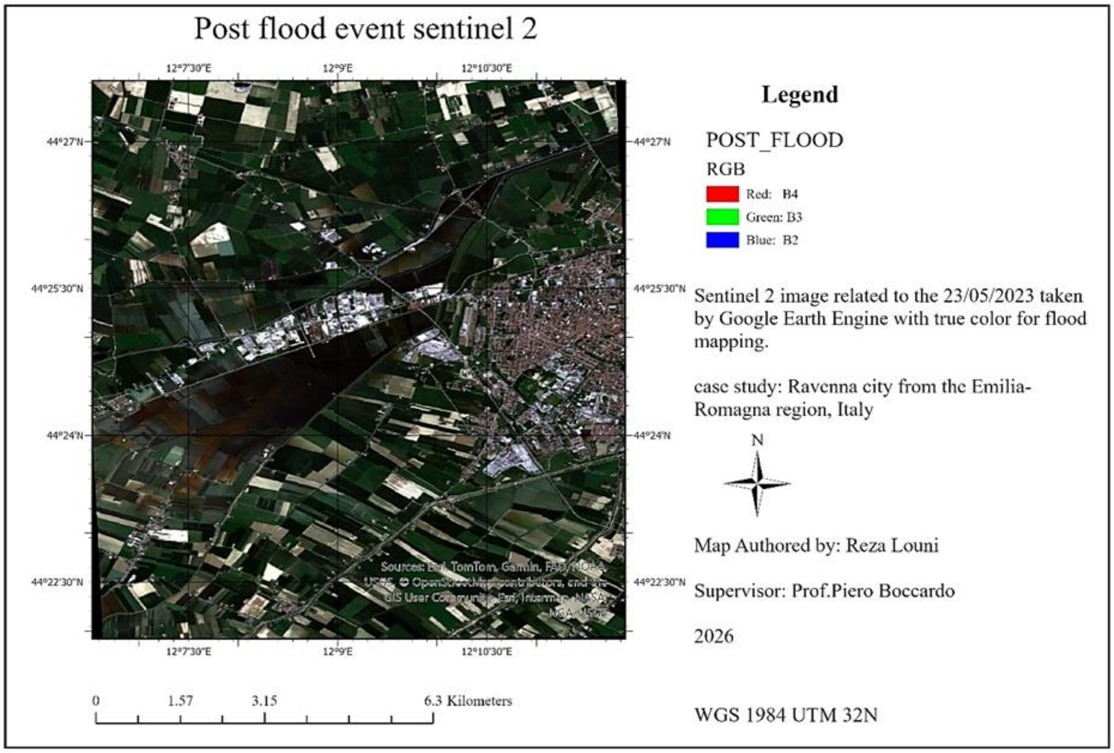

Figure 4-5 Post-flood event Sentinel 2

4.2.3 SkySat

SkySat is a commercial constellation of high-resolution optical satellites operated by Planet Labs, capable of acquiring imagery at sub-meter spatial resolution. This very fine spatial detail enables the identification of small-scale hydrological features such as flooded roads, inundated agricultural fields, and narrow drainage channels that are often unresolved in medium-resolution satellite data. The constellation also provides high temporal flexibility through on-demand tasking, allowing rapid image acquisition over targeted areas under suitable viewing and weather conditions. In this study, both pre-event and post-event SkySat images were available for the May 2023 flood event. The pre-event image, acquired on 17 January 2022, corresponds to an analytic Surface Reflectance (SR) product and represents typical land-surface conditions prior to flooding. This dataset was used to extract permanent water bodies through NDWI thresholding, generating a binary mask of stable rivers and channels existing before the event. The post-event image, acquired on 21 May 2023 under emergency acquisition, corresponds to a pan-sharpened multispectral product. The pansharpened dataset enhances spatial detail and improves delineation of flood boundaries. NDWI was computed from the post-event image to identify water surfaces after the flood. To isolate newly inundated areas, the permanent water mask derived from the pre-event image was removed from the post-event water classification. Flood extent was therefore defined as post-event NDWI-derived water, excluding pre-existing permanent water bodies. Due to differences in radiometric processing and measurement units between the analytic SR pre-event product and the pansharpened post-event product, a change-detection approach was not adopted. Instead, flood delineation relied on post-event spectral indices combined with spatial masking of permanent water, ensuring radiometric consistency while exploiting the very high spatial resolution of SkySat imagery. The pre-event and post-event images are shown in Figures 4-6 and 4-7, respectively. The main spatial, spectral, temporal, and processing characteristics of the SkySat dataset used in this study are summarized in Table 4-3.

Table 4-3 – Technical characteristics of the SkySat dataset

Feature	**Description**
Mission	SkySat constellation
Operator	Planet Labs PBC
Sensor type	Optical multispectral
Spectral bands	Blue, Green, Red, Near-Infrared (NIR)
Spatial resolution	~ 0.5–0.8 m (pan-sharpened)
Swath width	~5 km
Temporal resolution	Sub-daily (on-demand tasking)
Imaging capability	Daytime, cloud-limited
Processing level	Orthorectified and pansharpened multispectral
Radiometric correction	Applied
Geometric correction	Orthorectified
Data access	Commercial (Planet Labs)

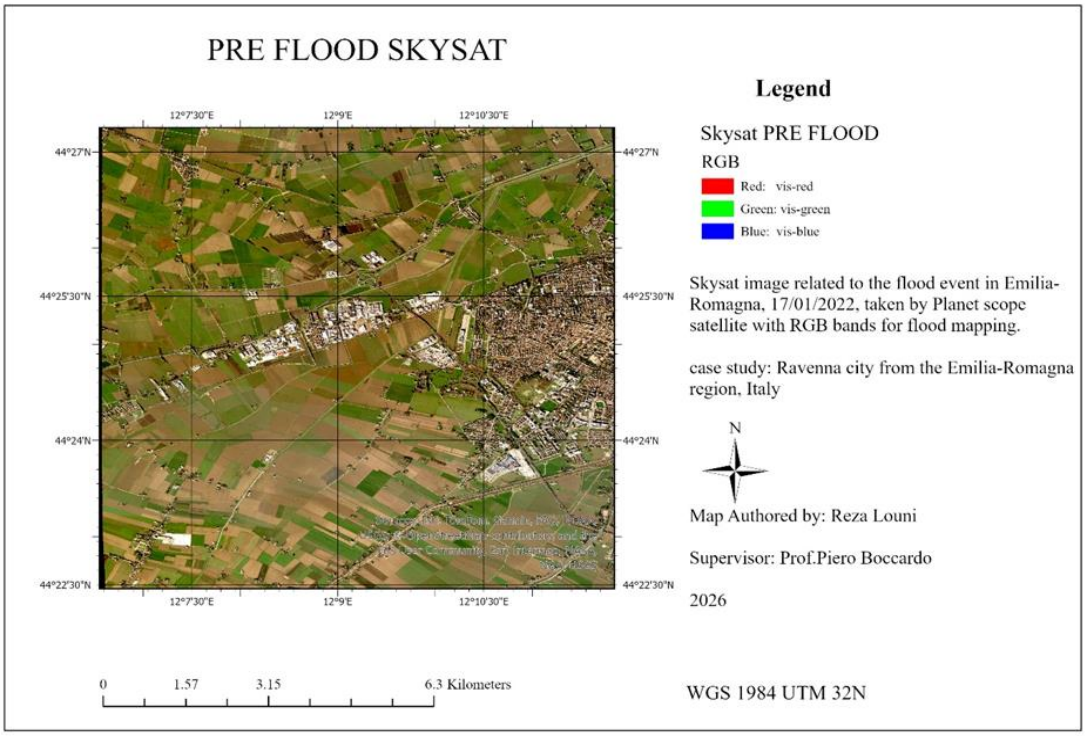

Figure 4-6 Pre-flood Skysat

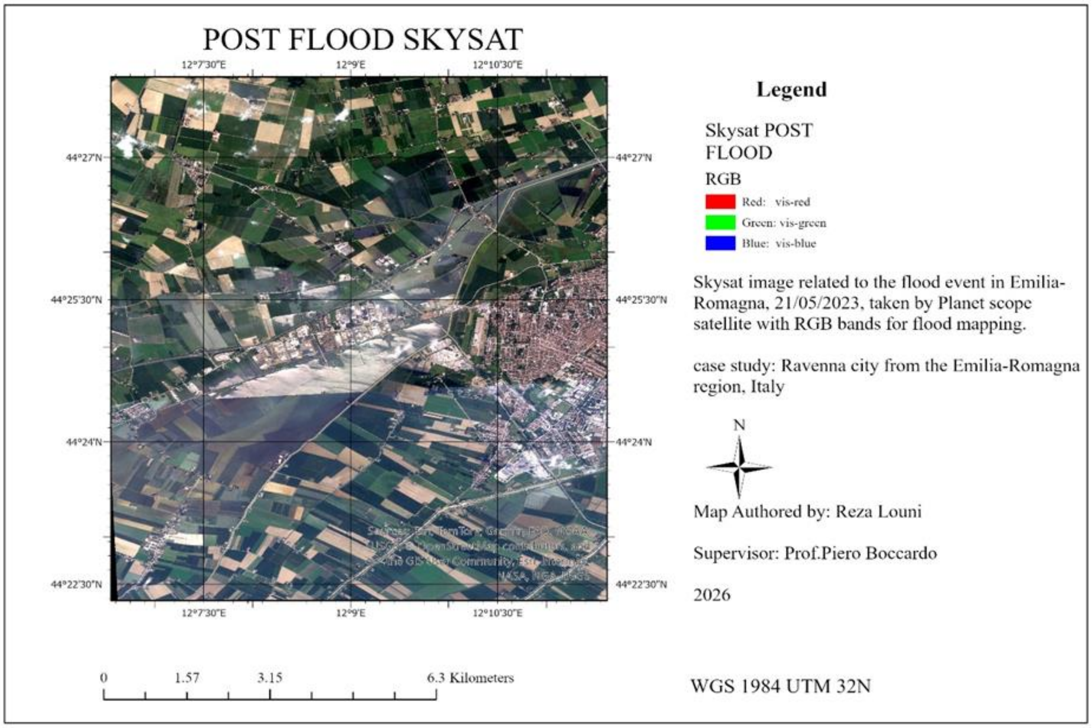

Figure 4-7 post flood skysat

4.2.4 Copernicus CEMS EMSR664 products

The Copernicus Emergency Management Service (CEMS) provides rapid, standardized geospatial data to support emergency response and recovery following natural disasters. Within CEMS, the Rapid Mapping component produces event-specific products from satellite Earth Observation data shortly after a hazard occurs. These products are widely used in scientific research as independent reference datasets for disaster assessment and validation because of their operational reliability, transparent methodology, and consistent mapping standards. In this study, flood extent products from the CEMS Rapid Mapping activation EMSR664 were used as an external reference to validate satellite-based flood maps derived from Sentinel-1 SAR, Sentinel-2 optical imagery, and very-high-resolution (VHR) SkySat data. EMSR664 was activated in response to the May 2023 extreme flooding event in the Emilia-Romagna region (northern Italy), which was caused by persistent heavy rainfall that led to widespread river overflows, surface flooding, and severe impacts on urban and agricultural areas. Only the Delineation monitoring 3 – Observed Event product was used in this study. This dataset provides vector polygons delineating areas identified as flooded at the time of satellite acquisition on 21 May 2023, thereby capturing the flood's peak extent. The product was generated within the Copernicus Emergency Management Service (CEMS) Rapid Mapping framework using COSMO-SkyMed X-band Synthetic Aperture Radar (SAR) imagery, acquired on 21 May 2023 at 16:50 UTC, with a spatial resolution of 5 m. Owing to its operational derivation and independent processing chain, the dataset was considered a suitable reference for the quantitative validation of the derived flood maps. The corresponding map is shown in Figure 4-8.

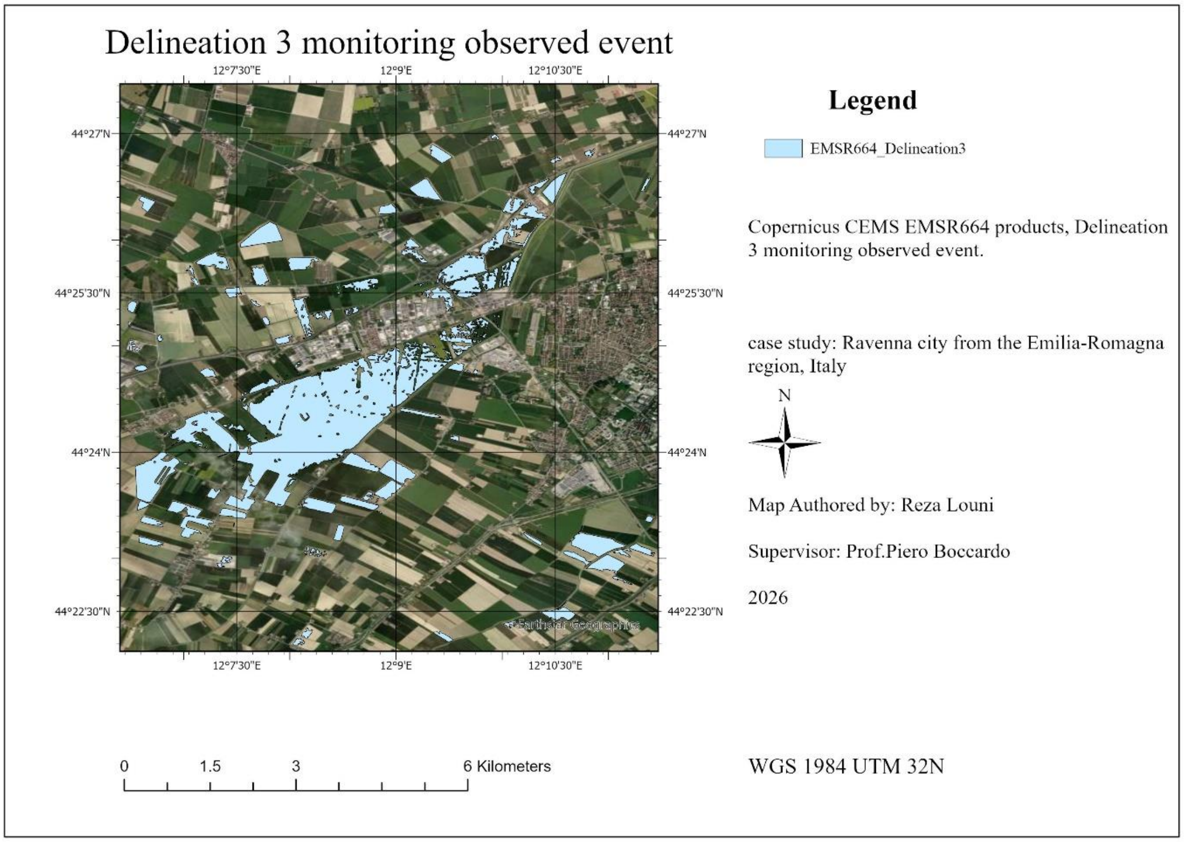

Figure 4-8 Copernicus CEMS EMSR664 product

4.2.5 Copernicus EMSN-154 water-depth product

The Copernicus Emergency Management Service (CEMS) Risk and Recovery Mapping (RRM) component provides standardized geospatial products to support post-event analysis and recovery planning following major natural disasters. Within this framework, the EMSN-154 activation ("Flood in Emilia-Romagna, Italy") was initiated after the May 2023 flood event to deliver detailed flood delineation and water-depth products for the affected region. In this study, the P04 Flood Delineation water-depth product generated under EMSN-154 was used as an independent reference dataset for the validation of FWDET-derived flood-depth estimates. The P04 product combines Sentinel-1 SAR imagery acquired on 22 and 23 May 2023 with a 5 m Digital Terrain Model (DTM) provided by the Regione Emilia-Romagna geoportal to derive both flood extent and corresponding water depth values. Water depth was estimated through a DTM-based percentile approach applied within delineated flood polygons, resulting in a single-band raster where pixel values represent water depth in meters. Owing to its operational derivation, standardized processing chain, and documented quality control procedures, the EMSN-154 water-depth product was considered a suitable independent benchmark for quantitative comparison with the FWDET-based depth maps produced at different spatial resolutions (30 m, 5 m, and 0.5 m). The dataset was retained in its native spatial resolution and projection to avoid introducing distortions associated with resampling during validation.(CEMS, 2023)

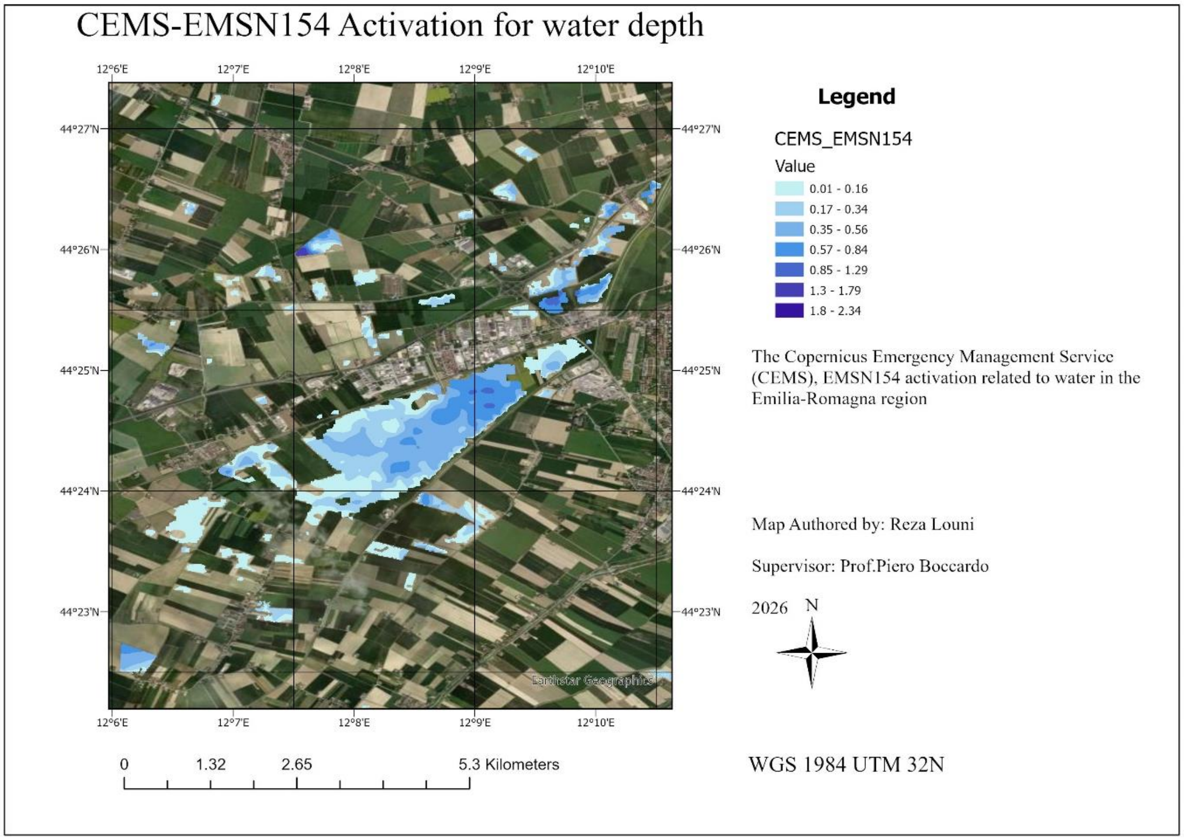

Figure 4-9 Copernicus CEMS EMSR664 product

4.2.6 Global and LiDAR-derived elevation models.

Elevation data are a critical component of flood analysis, as surface topography directly controls water flow paths, inundation extent, and floodwater depth. In this study, multiple elevation datasets with different spatial resolutions and origins were used to examine the sensitivity of floodwater-depth estimates to terrain representation and to evaluate the benefits of progressively higher-resolution topographic data. A global Digital Elevation Model (DEM) with a spatial resolution of 30 × 30 m was initially employed to represent regional-scale terrain conditions. Specifically, the Shuttle Radar Topography Mission (SRTM) DEM was used, which is derived from spaceborne C-band radar interferometry and released by NASA and the USGS. Global DEMs such as SRTM provide near-continuous spatial coverage and are widely used in large-scale hydrological and flood-mapping applications. However, their relatively coarse spatial resolution and limited vertical accuracy restrict their ability to capture fine-scale terrain features such as embankments, roads, drainage channels, and subtle elevation gradients, particularly in low-relief floodplain environments. To better represent local terrain variability while maintaining computational efficiency, a medium-resolution Digital Terrain Model (DTM) with a spatial resolution of 5 × 5 m was also utilized. This dataset was derived from airborne LiDAR surveys conducted over the study area and represents bare-earth elevations obtained after the removal of vegetation and built structures. Compared to global DEMs, the 5 m LiDAR-derived DTM provides substantially improved vertical accuracy and resolves smaller morphological features, making it well suited for flood-depth estimation in semi-urban and agricultural landscapes. Finally, a very-high-resolution LiDAR-derived DTM with a spatial resolution of 0.5 × 0.5 m was included to capture detailed local topography. This dataset enables an accurate representation of micro-topographic features such as levees, curbs, small channels, road embankments, and local depressions, all of which strongly influence floodwater distribution and depth in flat floodplain areas. Very-high-resolution LiDAR DTMs are particularly valuable for detailed flood impact assessments and for identifying the limitations of coarser elevation datasets. All elevation models were incorporated into the Google Earth Engine platform and used as terrain inputs for the Floodwater Depth Estimation Tool (FWDET). By applying FWDET to SRTM DEMs and DTMs of increasing spatial resolution, this study systematically evaluates how terrain detail influences floodwater-depth estimates and emphasizes the importance of high-resolution elevation data for accurate flood hazard assessment. The main technical characteristics of the elevation datasets used in this study are summarized in Table 4-4. The resulting flood-depth maps are presented in Figures 4-10, 4-11, and 4-12.

Table 4-4 – Technical characteristics of elevation datasets

Feature	Global DEM	Medium-resolution DTM	Very-high-resolution DTM
Dataset name	SRTM DEM	Regional LiDAR DTM	High-resolution LiDAR DTM
Data type	Digital Elevation Model	Digital Terrain Model	Digital Terrain Model
Acquisition mode	Spaceborne C-band InSAR	Airborne LiDAR	Airborne LiDAR
Releasing authority	NASA / USGS	Regional authority (Emilia-Romagna)	Regional authority (Emilia-Romagna)
Spatial resolution	30 m	5 m	0.5 m
Vertical accuracy (RMSE)	~10 m	~0.15–0.30 m	~0.05–0.15 m
Coverage	Near-global	Regional	Local / sub-regional
Surface representation	Includes vegetation and structures	Bare earth	Bare earth
Ability to resolve micro-topography	Low	Moderate	High

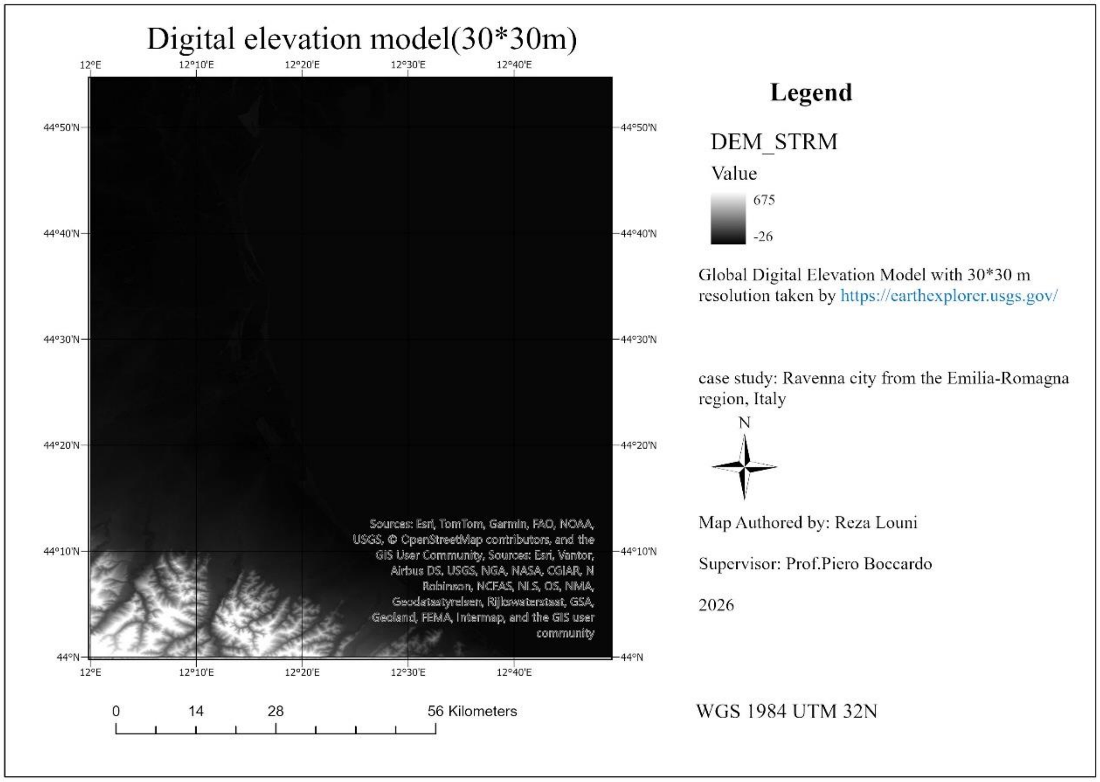

Global Digital Elevation Model with 30*30 m resolution taken by https://earthexplorer.usgs.gov/

case study: Ravenna city from the Emilia-Romagna region, Italy

Map Authored by: Reza Louni

Supervisor: Prof.Piero Boccardo

2026

Sources: Esri, TomTom, Garmin, FAO, NOAA, USGS, © OpenStreetMap contributors, and the GIS User Community, Sources: Esri, Vantor, Airbus DS, USGS, NGA, NASA, CGIAR, N Robinson, NCEAS, NLS, OS, NMA, Geodatastyrelsen, Rijkswaterstaat, GSA, Geoland, FEMA, Intermap, and the GIS user community

Figure 4-10 Global Digital Elevation Model (30*30m)

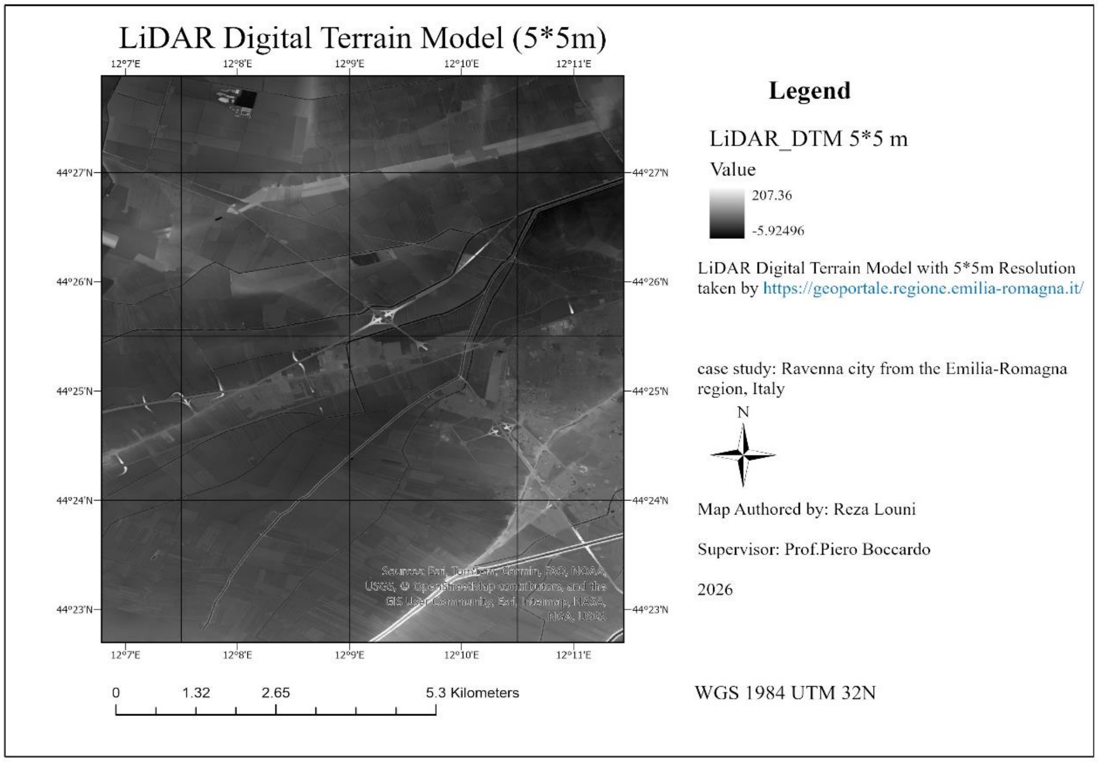

LiDAR Digital Terrain Model with 5*5m Resolution taken by https://geoportale.regione.emilia-romagna.it/

case study: Ravenna city from the Emilia-Romagna region, Italy

Map Authored by: Reza Louni

Supervisor: Prof.Piero Boccardo

2026

Sources: Esri, TomTom, Garmin, FAO, NOAA, USGS, © OpenStreetMap contributors, and the GIS User Community, Esri, Intermap, NASA, NGA, USGS

Figure 4-11 LiDAR Digital Terrain Model (5*5m)

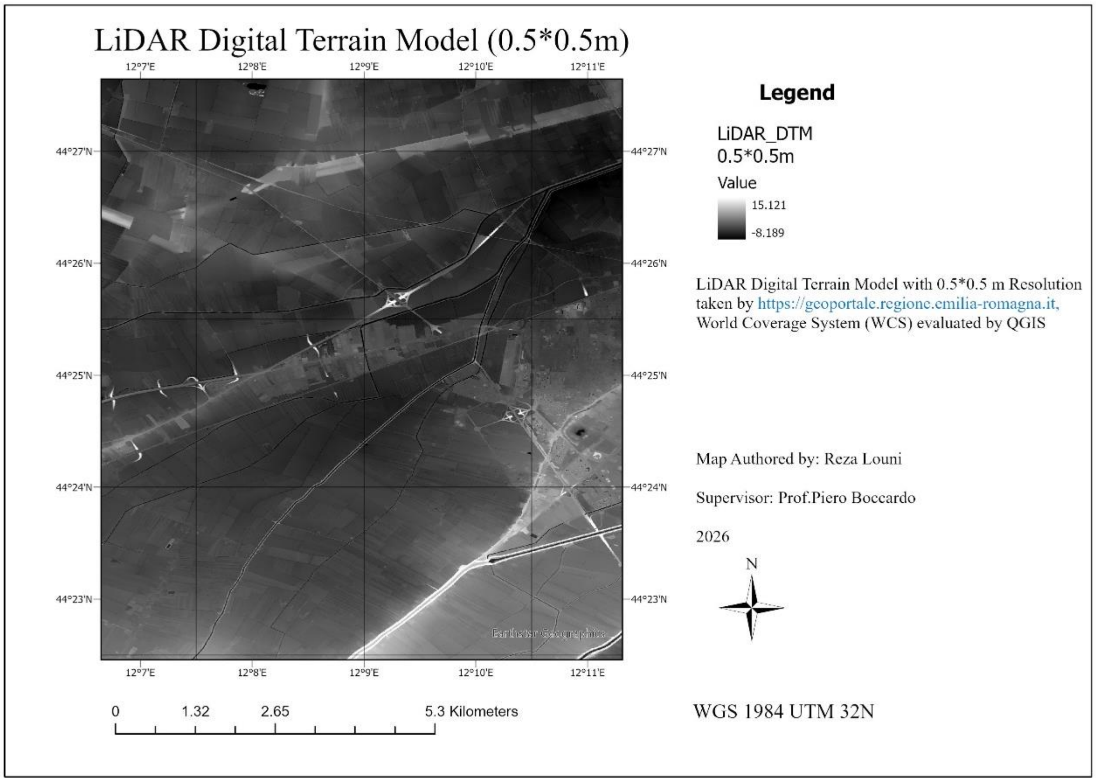

Figure 4-12 LiDAR Digital Terrain Model (0.5*0.5m)

4.2.7 Google Earth Engine (GEE) and other tools

Google Earth Engine (GEE) is a cloud-based geospatial analysis platform that enables large-scale processing of satellite imagery and geospatial datasets. Its architecture allows computations to be executed on remote servers, eliminating the need to download and store large volumes of data locally. In this study, GEE is used as the primary environment for satellite-based processing, including image preprocessing, spectral index calculation, threshold-based flood-extent mapping, flood-water depth estimation using FWDET, and the export of raster products. GEE provides native access to Sentinel-1 SAR, Sentinel-2 MSI, and several global digital elevation models, and also supports the integration of externally uploaded datasets such as SkySat imagery and LiDAR-derived Digital Terrain Model (DTM) tiles. The scripting environment, based on the JavaScript API, enables the implementation of reproducible and sensor-specific workflows, ensuring methodological consistency across the multi-sensor analysis. In addition to cloud-based processing in GEE, desktop Geographic Information System (GIS) software was used for selected preprocessing, quality-control, and cartographic tasks. High-resolution LiDAR-derived DTMs were processed using QGIS and ArcGIS Pro to inspect terrain quality, remove noise and elevation artifacts, and prepare consistent terrain datasets prior to their use in flood-depth estimation. ArcGIS Pro was further employed to refine flood maps by removing isolated or irrelevant pixels incorrectly classified as water and to define and verify the common Area of Interest (AOI) shared across all datasets. Finally, ArcGIS Pro was used for map layout design, symbology, and figure production for the maps included in this dissertation.

4.3 Pre-processing

Preprocessing steps were applied to all satellite datasets before flood detection to ensure radiometric consistency, spatial alignment, and suitability for index-based analysis. Because different sensors produce data at varying levels of processing, the preprocessing workflow was adapted accordingly. All operations were performed within Google Earth Engine (GEE), except for SkySat imagery, which was supplied as pre-processed products by the data provider. The following subsections describe the preprocessing steps applied to Sentinel-1, Sentinel-2, and SkySat imagery.

4.3.1 Common preprocessing steps

All satellite images used in this study were clipped to a common Area of Interest (AOI) corresponding to the study area boundary. This operation reduced computational load and ensured spatial consistency across datasets with different spatial resolutions, acquisition geometries, and sensor characteristics. A consistent spatial reference system was adopted for all datasets to allow direct comparison and integration in subsequent analyses.

4.3.2 Sentinel-1 SAR Preprocessing

The Sentinel-1 data used in this study were Level-1 Ground Range Detected (GRD) products accessed through Google Earth Engine (GEE). These products are radiometrically calibrated to sigma-naught (σ^0) backscatter and geocoded to a ground-range projection as part of the standard ESA processing chain. Consequently, no manual radiometric calibration or terrain correction was required. Preprocessing steps specific to Sentinel-1 data were implemented in GEE and included the following:

1. Image filtering and selection:

Pre-event and post-event Sentinel-1 images were selected based on acquisition date, spatial coverage of the Area of Interest, Interferometric Wide (IW) acquisition mode, VH polarization, and orbit direction. These selection criteria follow established practices in SAR-based flood mapping to ensure comparability between pre- and post-event observations.

2. Speckle noise reduction:

A refined Lee speckle filter was applied to both pre-event and post-event images to reduce inherent SAR speckle noise while preserving edges and spatial detail. This step is essential for improving the separability between flooded and non-flooded surfaces, particularly in heterogeneous landscapes.

4.3.3 Sentinel-2 Preprocessing

Sentinel-2 Level-2A surface reflectance (SR) products were utilized in this study. These images were atmospherically corrected before distribution, so no further atmospheric correction was necessary. All preprocessing steps were performed in Google Earth Engine (GEE) and are summarized as follows:

1. Cloud masking:

Cloud- and shadow-affected pixels were removed using the Scene Classification Layer (SCL). Pixels classified as cloud shadow (SCL = 3), medium probability cloud (SCL = 8), high probability cloud (SCL = 9), thin cirrus (SCL = 10), and snow/ice (SCL = 11) were masked out to ensure that spectral calculations relied only on valid surface reflectance data. This masking procedure was applied to the pre-event dataset used to generate the baseline composite.

2. Band extraction and scaling:

Surface reflectance values were scaled by dividing digital numbers by 10,000. The Green (B3) and Near-Infrared (B8) bands required for NDWI computation were extracted at 10 m spatial resolution. Additional bands were retained for visualization purposes but were not modified during preprocessing.

4.3.4 SkySat preprocessing

Very-high-resolution SkySat imagery provided by Planet Labs was used in this study for detailed flood mapping. The SkySat scenes were delivered as analysis-ready orthorectified surface reflectance products (SkySat Ortho Scene), belonging to Planet’s standard SkySat data assets.

These products are generated through Planet’s processing chain, which includes radiometric calibration, band co-registration, geometric correction, and orthorectification to remove terrain-induced distortions, resulting in spatially consistent and geolocated imagery suitable for direct analytical use. For the pre-event dataset, surface reflectance imagery was used in its orthorectified multispectral format without additional spatial enhancement. In contrast, the post-event dataset was derived from the pansharpened multispectral asset, which combines the high-resolution panchromatic band with multispectral bands to enhance spatial detail while preserving spectral characteristics. No additional radiometric or geometric corrections were applied, as the distributed products are provided as analysis-ready data suitable for immediate spectral index computation and flood delineation.

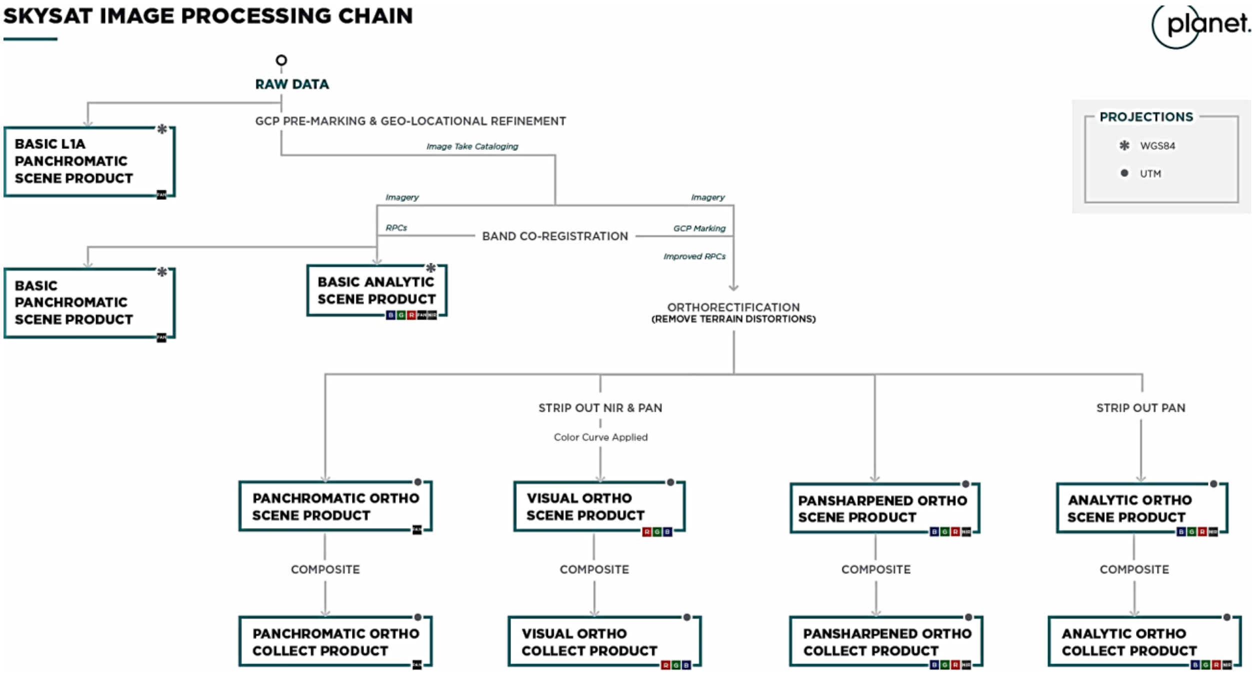

Figure 4-13 Skysat image processing chain

As a result, no additional physical preprocessing was performed in this study. The data preparation steps implemented in Google Earth Engine (GEE) consisted of the following:

1. Cloud filtering for analysis:

   To minimize the impact of residual cloud contamination on flood-mapping results, a straightforward spectral filtering method was used to identify and remove pixels influenced by clouds. This process served only as an analysis-level quality filter and did not modify the underlying radiometric properties of the imagery.

2. Band selection:
   The available Blue, Green, Red, and Near-Infrared bands were used. The Green and Near-Infrared bands were essential for NDWI-based flood detection, while the visible bands were kept for visualization purposes.

4.4 Temporal alignment between sensors

Temporal consistency among satellite observations is essential in multi-sensor flood studies because flood extent and water levels can change rapidly over short periods. In this study, the acquisition dates of all datasets were examined and selected to ensure that different sensors captured comparable stages of the May 2023 Emilia-Romagna flood event. For the pre-event (dry reference) condition, Sentinel-1 and Sentinel-2 images acquired on April 28, 2023, were used. The only available pre-event SkySat imagery corresponded to an analysis-ready orthorectified surface reflectance product (SkySat Ortho Scene) acquired on January 17, 2022. Although these pre-event datasets are not perfectly aligned in time, this does not affect the analysis, as pre-event imagery is used solely to represent typical non-flooded surface conditions rather than dynamic hydrological processes. The post-event period was considered more critical for flood characterization. SkySat imagery acquired on May 21, 2023, was used to represent flooded conditions at very high spatial resolution. The Sentinel-1 and Sentinel-2 post-event acquisitions occurred on May 23, 2023, resulting in a temporal gap of approximately two days. This offset, driven by sensor revisit intervals and data availability, was considered acceptable given the scale of the event and the persistence of inundation during this period. Flood extent products from the Copernicus Emergency Management Service (CEMS) Rapid Mapping activation EMSR664 were also based on satellite data acquired on May 21, 2023, aligning them temporally with the post-event SkySat imagery. These products served as an external reference for validation. All datasets were classified into pre-event and post-event periods, providing a consistent temporal framework for flood-extent mapping, floodwater depth estimation using FWDET, and accuracy assessment. Differences between datasets primarily reflect sensor characteristics and spatial resolution rather than temporal variations in flood conditions.

4.5 Workflow in Google Earth Engine

4.5.1 Sentinel-1 workflow

The Sentinel-1 Synthetic Aperture Radar (SAR) flood-mapping workflow was implemented in Google Earth Engine (GEE) and follows a structured sequence of data selection, preprocessing, backscatter change detection, and threshold-based classification. Sentinel-1 Ground Range Detected (GRD) images were filtered spatially using a common Area of Interest (AOI) and temporally to define pre-event and post-event conditions. Only Interferometric Wide (IW) mode acquisitions in VH polarization were used, as this configuration provides wide coverage and high sensitivity to surface water.

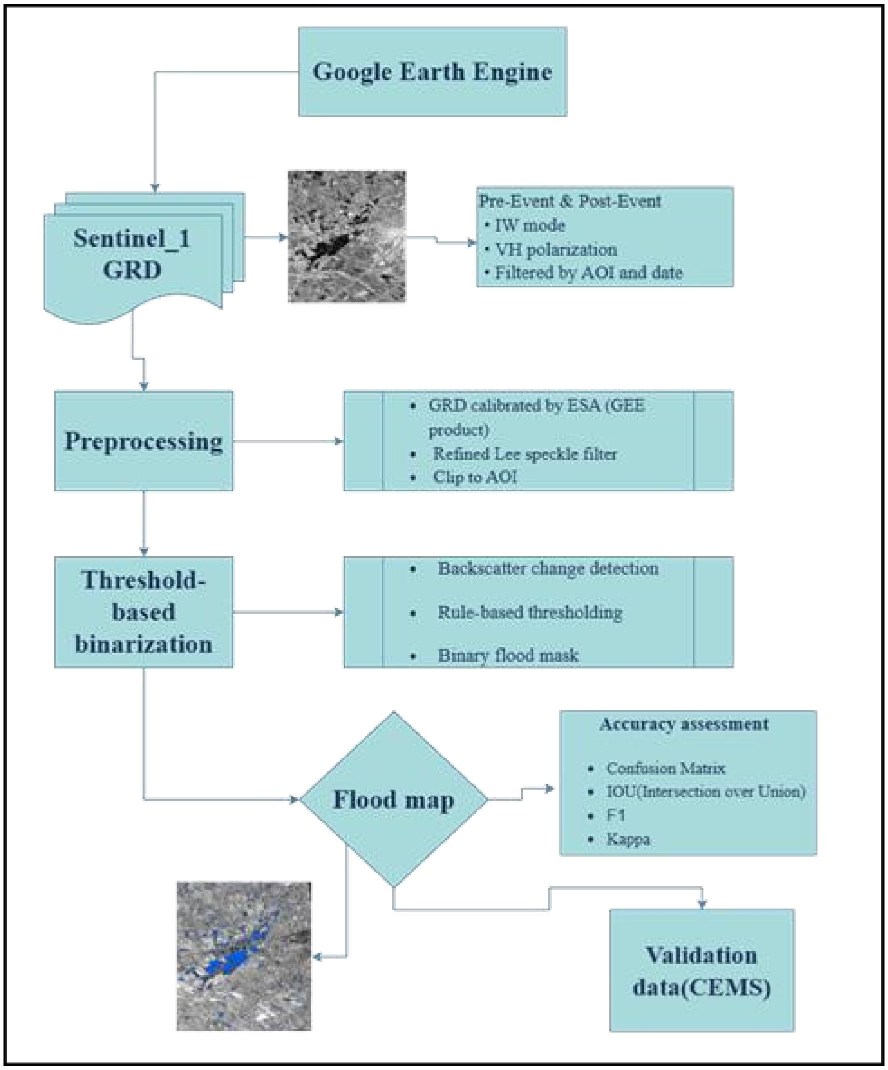

Figure 4-14 Sentinel-1 workflow diagram

1. Definition of the Area of Interest (AOI)

The analysis was conducted over a predefined common Area of Interest (AOI) imported as a GEE asset. The use of a shared AOI ensures spatial consistency across all sensors and processing steps and limits the analysis to the study area relevant to the May 2023 Emilia-Romagna flood event.

2. Sentinel-1 GRD image collection

Sentinel-1 Ground Range Detected (GRD) imagery was accessed from the Copernicus archive available in GEE. The GRD products are radiometrically calibrated to sigma-naught (σ^0) backscatter and terrain-corrected as part of the standard ESA processing chain, ensuring consistent radiometric and geometric properties prior to analysis.

3. Spatial and sensor-specific filtering

In this step, the Sentinel-1 GRD image collection is filtered to include only scenes that intersect the specified Area of Interest (AOI), ensuring full coverage of the study region. Only images captured in Interferometric Wide (IW) swath mode are utilized, as IW is the standard Sentinel-1 acquisition mode over land, offering extensive spatial coverage (around 250 km swath) with a ground resolution appropriate for regional flood mapping. The analysis focuses on VH polarization, where the radar transmits vertically and receives horizontally polarized signals. This cross-polarized channel is highly sensitive to volume scattering and shows significant backscatter reduction over open water and flooded vegetation, making it effective for detecting inundation. Additionally, scenes from both ascending and descending orbits are incorporated. Ascending passes occur from south to north, while descending passes move from north to south. Using both viewing geometries enhances data availability and spatial coverage, while minimizing potential angular effects related to surface orientation and incidence angle.

4. Definition of pre-event and post-event periods

Two temporal subsets were defined to represent reference (pre-flood) and flooded (post-event) conditions. The pre-event period captures normal, non-flooded surface conditions, while the post-event period corresponds to the phase of observed inundation.

5. Image mosaicking and AOI clipping

For each temporal subset, VH-polarized Sentinel-1 acquisitions were mosaicked to generate a single representative pre-event image and a single post-event image covering the AOI. This step ensures spatial completeness and reduces variability associated with individual scene boundaries.

6. Conversion between dB and linear scale

Speckle filtering requires backscatter values expressed in linear power units. Therefore, the mosaicked images were converted from decibel (dB) to a linear scale prior to filtering and converted back to dB after filtering to facilitate interpretation and change detection.

7. Speckle filtering using the Refined Lee filter

In this preprocessing step, speckle noise inherent to Sentinel-1 SAR backscatter imagery was reduced using the Refined Lee filter, an adaptive statistical filter designed explicitly for coherent radar data. Speckle manifests as granular multiplicative noise and can significantly affect pixel-based thresholding and change detection; therefore, speckle filtering was applied prior to computing change metrics and flood masks. The Refined Lee approach estimates local statistical properties, including the mean and variance of backscatter values, within a moving window and adaptively adjusts the degree of smoothing according to the surrounding spatial structure. Homogeneous areas, such as open water or uniform agricultural fields, are smoothed more strongly to suppress noise. In contrast, heterogeneous regions and sharp edges, including riverbanks, levees, infrastructure, and land-water transitions, are preserved through directionally selective filtering that limits blurring across boundaries. In the implemented workflow, the Sentinel-1 VH backscatter was first converted from decibels (dB) to linear units, as the speckle model and Refined Lee estimator operate correctly in linear power space. The Refined Lee filter was then applied using a 7 × 7 moving window, after which the filtered output was converted back to dB for interpretation and for subsequent pre-event and post-event difference calculations.

8. Change detection between pre-event and post-event Sentinel-1 images

After speckle filtering, flood-related surface changes are identified using a backscatter change-detection approach. The filtered pre-event and post-event Sentinel-1 VH images are first harmonized by assigning explicit band names, which facilitates subsequent pixel-wise operations.

A different image is then computed by subtracting the pre-event backscatter from the post-event backscatter in decibels (dB). In SAR-based flood mapping, newly inundated surfaces typically exhibit a marked decrease in backscatter intensity, caused by specular reflection of the radar signal away from the sensor over smooth water surfaces. Consequently, negative values in the difference image indicate locations where a significant backscatter reduction has occurred between the two acquisition periods and are therefore potential indicators of flooding. This change image represents the primary flood-sensitive layer used in the subsequent threshold-based classification step.

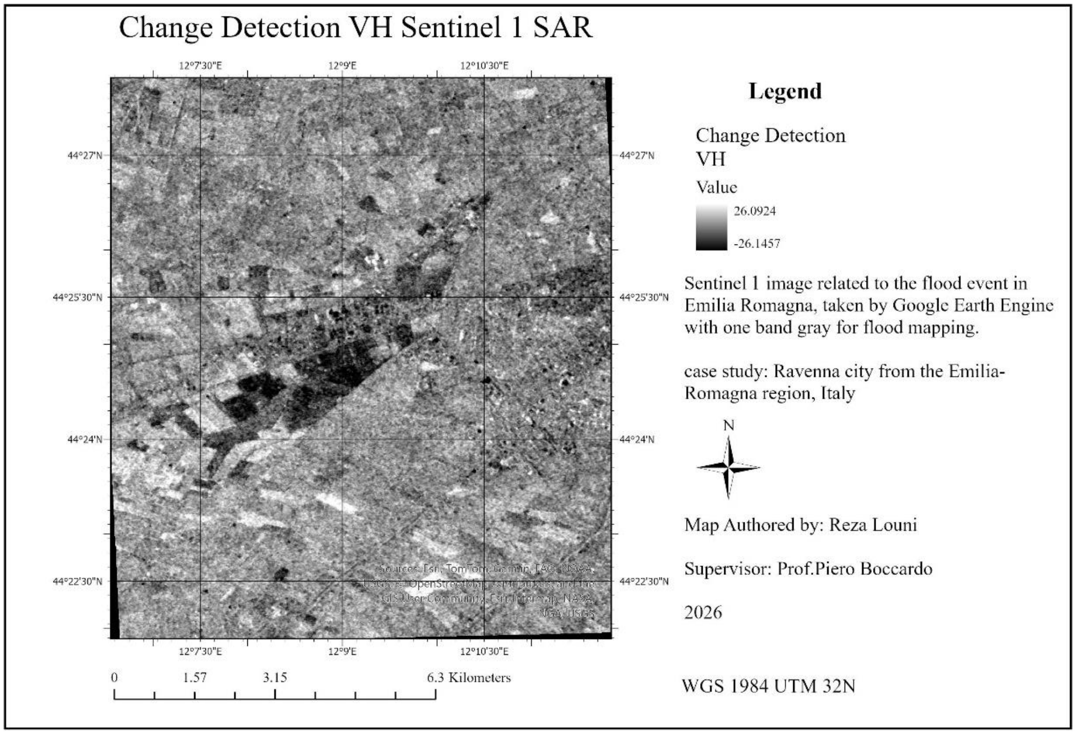

Sentinel 1 image related to the flood event in Emilia Romagna, taken by Google Earth Engine with one band gray for flood mapping.

case study: Ravenna city from the Emilia-Romagna region, Italy

Map Authored by: Reza Louni

Supervisor: Prof.Piero Boccardo

2026

Figure 4-15 Sentinel-1 VH backscatter change detection (ΔVH = VH_ post − VH_ pre) between pre-flood and post-flood acquisitions over the study area. Negative backscatter variations highlight areas affected by inundation, while stable or heterogeneous responses correspond to non-flooded surfaces and complex land-cover types

9. Threshold-based binarization

Flooded areas were identified through a rule-based thresholding scheme applied jointly to the pre-event, post-event, and backscatter difference images. The use of multiple complementary thresholds is motivated by the need to distinguish newly inundated surfaces from permanent water bodies and other persistently low-backscatter features, while minimizing false detections related to speckle noise, land-cover heterogeneity, and non-flood-related backscatter variability.

A post-event backscatter threshold of approximately −19 dB was adopted to identify surfaces exhibiting low absolute radar backscatter values consistent with open water or smooth flooded surfaces. In C-band Sentinel-1 VH polarization, flooded areas typically produce very low backscatter due to specular reflection, with values commonly reported below −18 to −20 dB. This threshold balances sensitivity to inundation with robustness against misclassification of wet but unflooded land surfaces. To exclude permanent water bodies, an additional absolute backscatter threshold of approximately −22 dB was applied simultaneously to both pre-event and post-event images. Pixels that remain extremely dark in both periods are unlikely to represent flood-induced change and are instead associated with stable hydrological features such as rivers, channels, and lakes. Flood-induced surface change was further constrained using a backscatter difference threshold of approximately −1.5 dB, computed as the difference between post-event and pre-event VH backscatter. This threshold represents a statistically meaningful decrease in backscatter intensity that exceeds typical short-term radiometric variability and residual speckle effects and is physically consistent with the transition from rough land surfaces to smoother water-covered conditions. The specific threshold values were determined through an iterative empirical calibration process, in which multiple candidate thresholds were tested. The final values were selected based on visual inspection of intermediate flood maps, comparison with very-high-resolution SkySat imagery, and consistency checks against Copernicus Emergency Management Service (CEMS) Rapid Mapping flood extent products. The selected thresholds provided the best balance between omission and commission errors while preserving spatial coherence of the mapped inundation patterns.

10. Spatial post-processing and noise removal

The initial binary flood mask from threshold-based binarization may contain isolated pixels and small, fragmented patches, which are common artifacts in SAR classification caused by residual speckle, local radiometric variability, and mixed land-cover responses. To improve the spatial coherence of the mapped inundation pattern, a post-processing step is applied to eliminate false detections and produce a clearer flood-extent product. First, a connected-component analysis is performed using a connected pixel count that measures the size of contiguous flooded clusters. Flood detections smaller than the minimum mapping unit are removed by masking connected components below a user-defined pixel threshold. This step effectively suppresses isolated noise and retains only spatially meaningful inundated features. Finally, an optional focal mode operation is applied as a light spatial smoothing step to reduce salt-and-pepper effects and enforce local majority consistency, while preserving the overall geometry of the flood extent.

11. Binary flood mask

After spatial refinement, the flood map was stored as a binary raster (0 = non-flooded, 1 = flooded), ensuring a consistent data structure for subsequent analysis and validation.

12. Export of the Sentinel-1 flood map and flooded area estimation

After creating the final binary flood mask, the Sentinel-1 flood-extent product is exported from Google Earth Engine for use in later analyses and integration with other datasets. The flood mask is exported as a raster at the native spatial resolution of Sentinel-1 GRD (10 m) over the shared AOI. Additionally, the total flooded area is calculated by summing the area of pixels classified as flooded within the AOI.

4.5.2 Sentinel 2 workflow

The Sentinel-2 flood-mapping workflow was implemented in Google Earth Engine (GEE) using Sentinel-2 Level-2A Surface Reflectance (SR) imagery. Flood detection was performed using the Normalized Difference Water Index (NDWI) and its temporal change between pre-event and post-event conditions. The workflow explicitly exploits NDWI change detection (ΔNDWI) to identify newly inundated areas, while pre-event NDWI is used to exclude permanent water bodies. The entire workflow is summarized in Figure 4-16.

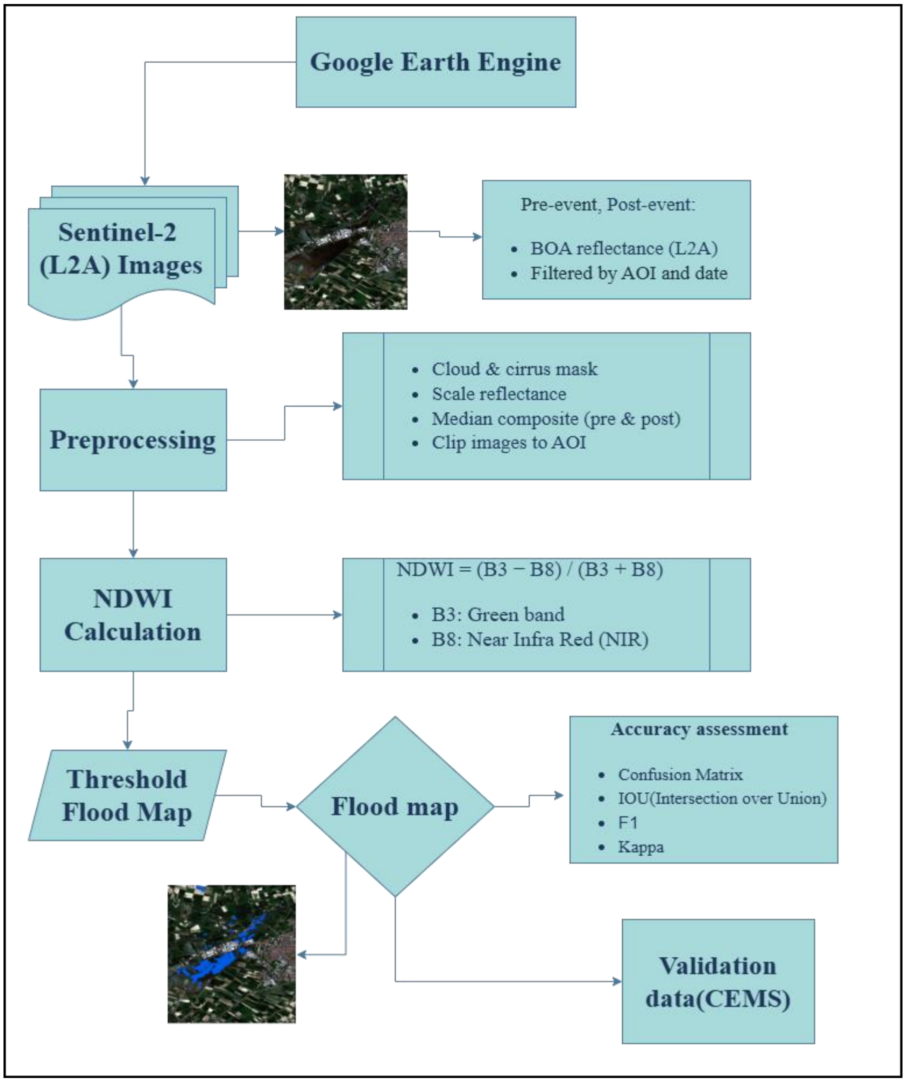

Figure 4-16 Sentinel 2 workflow diagram

1. Definition of the Area of Interest (AOI)

All Sentinel-2 image collections and derived products were spatially constrained to a common Area of Interest (AOI) imported as a project asset in GEE. Using a shared AOI ensures spatial consistency across all processing steps and enables direct comparison with flood products derived from other sensors.

2. Cloud masking

Cloud contamination was addressed using the Scene Classification Layer (SCL) provided with the Sentinel-2 Level-2A product. Pixels classified as cloud shadows, medium- and high-probability clouds, cirrus, and snow were masked prior to analysis. The SCL mask was applied consistently to all multispectral bands used in NDWI computation. Surface reflectance values were scaled by dividing by 10,000 according to Sentinel-2 SR specifications.

3. Pre-event and post-event image selection and median compositing

Different temporal strategies were adopted for pre-event and post-event conditions to reflect their distinct analytical roles.

Pre-event condition:

A median composite was generated from Sentinel-2 Level-2A surface reflectance images acquired between 21 April 2023 and 5 May 2023 (±7 days centered on 28 April 2023). Cloud- and shadow-affected pixels were removed using the Scene Classification Layer (SCL) prior to compositing. The median composite provides a stable representation of normal surface conditions and reduces residual cloud contamination and scene-to-scene radiometric variability.

Post-event condition:

A single Sentinel-2 acquisition from 23 May 2023 was used to represent flooded conditions. Median compositing was intentionally avoided for the post-event period to preserve the instantaneous flood signal and avoid temporal smoothing of inundation patterns.

4. NDWI Computation

Flooded surfaces exhibit a characteristic spectral response in optical imagery, with relatively high reflectance in the green band and strong absorption in the near-infrared (NIR) band. This contrast is exploited through the Normalized Difference Water Index (NDWI), computed for both pre-event and post-event images as:

$$\mathrm{NDWI} = \frac{G - NIR}{G + NIR} \qquad (4\text{-}1)$$

where G represents the surface reflectance in the green band (Sentinel-2 B3), and NIR represents the surface reflectance in the near-infrared band (Sentinel-2 B8). NDWI was computed at the native 10 m spatial resolution, which defines the working resolution of the Sentinel-2 flood-mapping workflow. The index is widely used for surface-water detection in optical remote sensing.(S.K.McFEETERS, 1996)

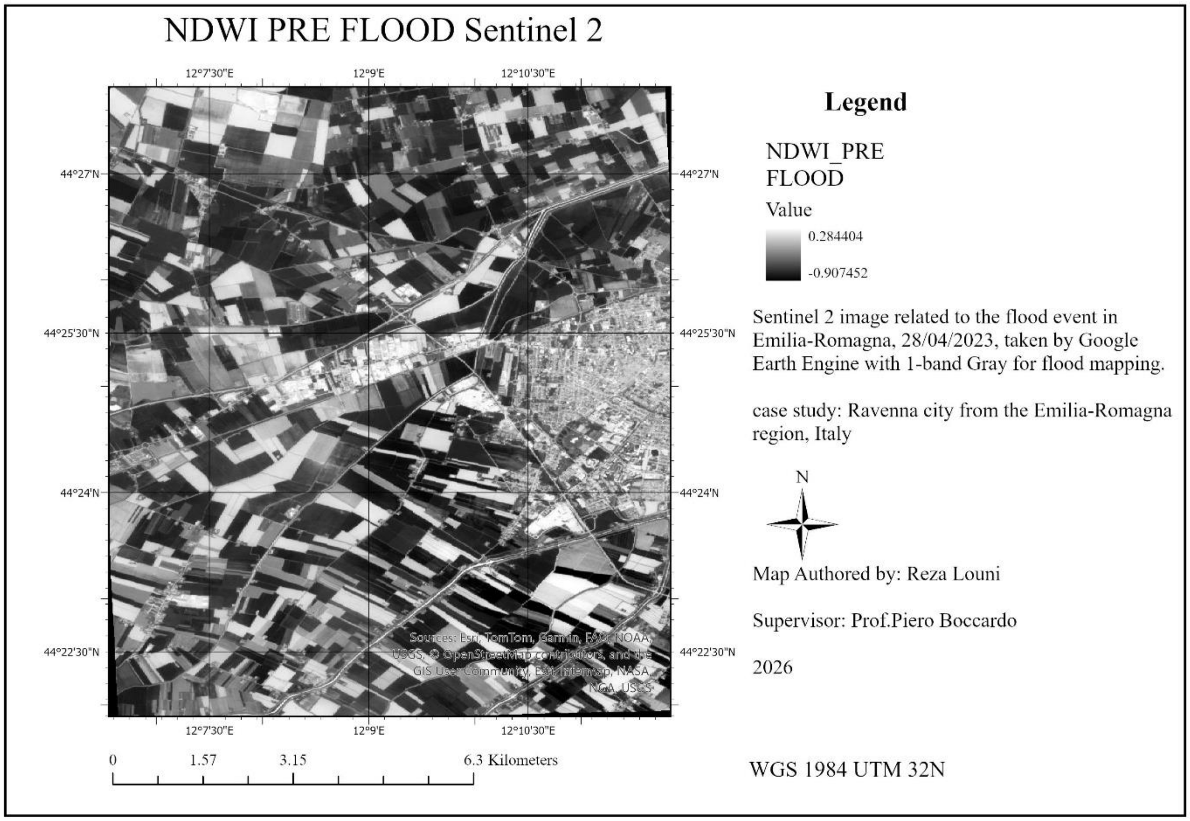

Figure 4-17 NDWI pre-flood

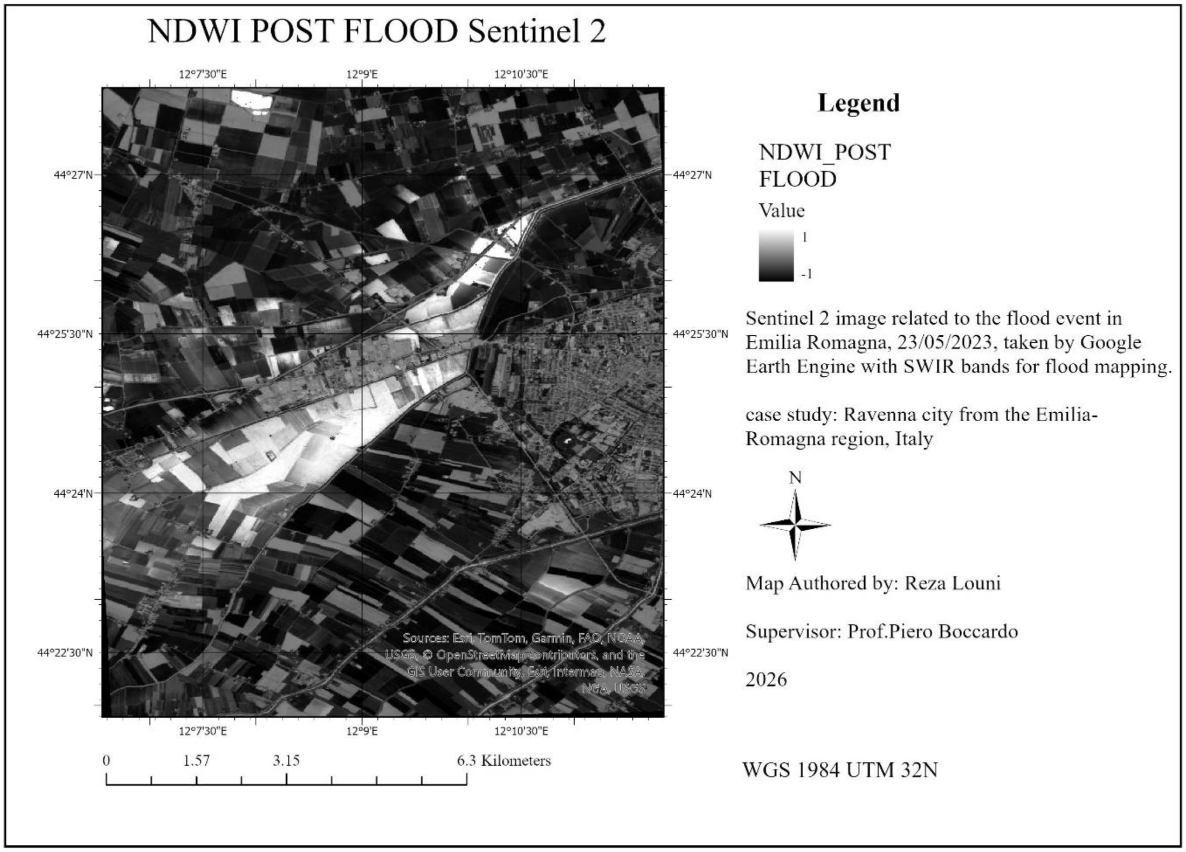

Figure 4-18 NDWI post-flood

5. ΔNDWI computation and threshold-based flood mask generation

Flood extent was delineated using an explicit NDWI change-detection approach, in which newly inundated areas are identified based on the spectral change between pre-event and post-event conditions rather than on absolute NDWI values from a single acquisition. NDWI was computed for both the pre-event reference image and the post-event Sentinel-2 image using the green (B3) and near-infrared (B8) bands in 10-meter spatial resolution. The NDWI difference (ΔNDWI) was then calculated as:

$$\Delta\mathrm{NDWI} = \mathrm{NDWI}_{post} - \mathrm{NDWI}_{pre}$$

The flood classification is primarily driven by ΔNDWI, which captures the spectral transition from land to open water caused by inundation. In optical imagery, flooded surfaces typically exhibit a marked increase in NDWI after the event due to high reflectance in the green band and strong absorption in the near-infrared band. In contrast, non-flooded surfaces show little or no change. Flooded pixels were identified using a rule-based thresholding scheme combining ΔNDWI with auxiliary NDWI constraints:

- ΔNDWI ≥ 0.15, indicating a significant increase in water-like spectral response between pre-event and post-event conditions.
- Post-event NDWI ≥ 0.15, confirming the presence of surface water after the flood.
- Pre-event NDWI < 0.15, excluding pixels that already exhibited water-like spectral characteristics before the event and therefore correspond to permanent or pre-existing water bodies.

Only pixels satisfying all three conditions were classified as flooded. While ΔNDWI represents the core flood-detection criterion, the pre- and post-event NDWI thresholds act as consistency constraints, improving robustness by suppressing false detections over permanent water bodies, moist soil, and vegetated surfaces. The ΔNDWI threshold of 0.15 was selected through an iterative trial-and-error calibration process, given the site-specific flood conditions and land-cover characteristics. Several candidate ΔNDWI thresholds were tested and visually evaluated using Sentinel-2 imagery, NDWI and ΔNDWI maps, very-high-resolution SkySat observations, and Copernicus Emergency Management Service (CEMS) flood-extent products. A value of 0.15 consistently provided the best compromise between omission and commission errors, effectively capturing newly inundated areas while limiting false positives. The auxiliary NDWI thresholds (±0.15) correspond to standard values commonly used to distinguish open water from non-water surfaces in Sentinel-2 imagery and were retained to ensure methodological consistency and physical interpretability. The resulting flood mask was refined using the selfMask() operation and exported as a binary raster for subsequent flooded-area estimation and multi-sensor comparison.

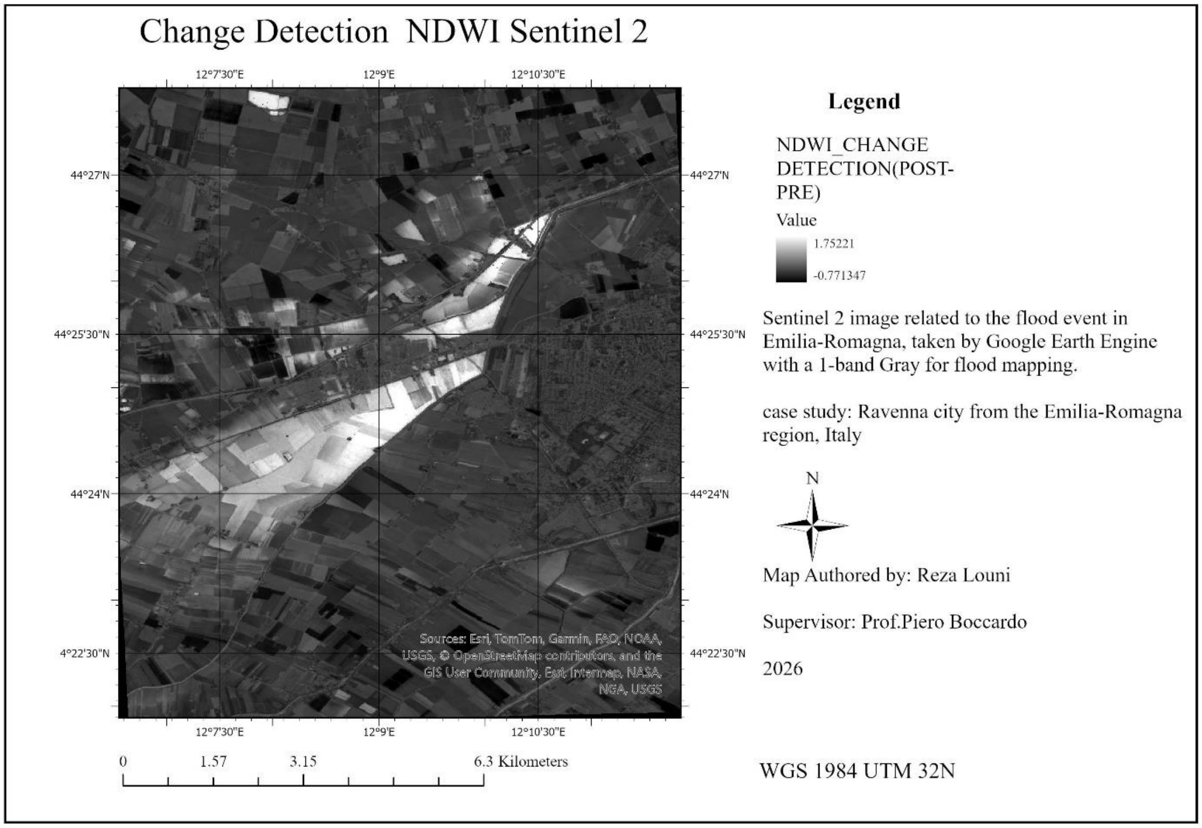

Figure 4-19. Sentinel-2 NDWI change-detection (ΔNDWI) map used for flood delineation, with values above the selected threshold (ΔNDWI ≥ 0.15) indicating newly inundated areas.

6. Visualization layers and map inspection

Visual inspection is an essential step for evaluating the quality and internal consistency of Sentinel-2 flood-mapping results. Visualization layers are generated for both pre-event and post-event conditions to support qualitative assessment of cloud masking performance, NDWI behavior, and the spatial coherence of the detected flood extent. These layers are not used directly in the classification process, but they provide an important diagnostic tool for interpreting the results and identifying potential artifacts. True-color RGB composites are used primarily to verify overall scene quality and cloud masking effectiveness. However, because flooded surfaces often exhibit spectral responses like wet soil or bare ground in visible bands, RGB imagery alone is not sufficient for reliable flood interpretation. For this reason, false-color composites at 10-meter spatial resolution using the Near-Infrared, Red, and Green bands (NIR–Red–Green) are employed as the main visualization product. In this configuration, open water and flooded areas appear distinctly darker due to strong absorption in the NIR band, while vegetation and non-flooded surfaces remain clearly separable. In addition, pre-event NDWI, post-event NDWI, and ΔNDWI layers are visualized to directly inspect water-related spectral changes associated with flooding. The ΔNDWI layer is particularly useful for confirming that detected flood pixels correspond to areas showing a clear increase in water-like spectral response after the event, rather than to permanent water bodies or noise. Finally, the binary flood mask is overlaid on the false-color composites to visually verify its spatial alignment with water-affected areas and to ensure consistency between the spectral indices and the final flood-extent product.

7. Binary flood mask generation and flooded area estimation

After visual inspection, the NDWI-based flood mask is converted into a clear binary raster for consistent data processing, export, and area calculation. In this format, flooded pixels are assigned 1, and non-flooded pixels are assigned 0. This step standardizes the flood product format, enabling direct comparison with flood masks from other sensors. The total flooded area is then calculated by multiplying the binary flood mask by the pixel area and summing these values across the AOI. Pixel area is converted from square meters to square kilometers to give a clear measure of flood extent.

8. Export Flood map

The final Sentinel-2 flood-mapping outputs are exported from Google Earth Engine for archiving and later analysis.

4.5.3 Skysat workflow

The SkySat flood-mapping workflow is implemented in Google Earth Engine (GEE) using very-high-resolution optical imagery acquired before and after the flood event. Pre-event and post-event scenes are imported from project assets and clipped to a common Area of Interest (AOI) to ensure spatial consistency and direct comparability with Sentinel-derived products. The overall processing chain is summarized in the workflow diagram (Figure 4-20).

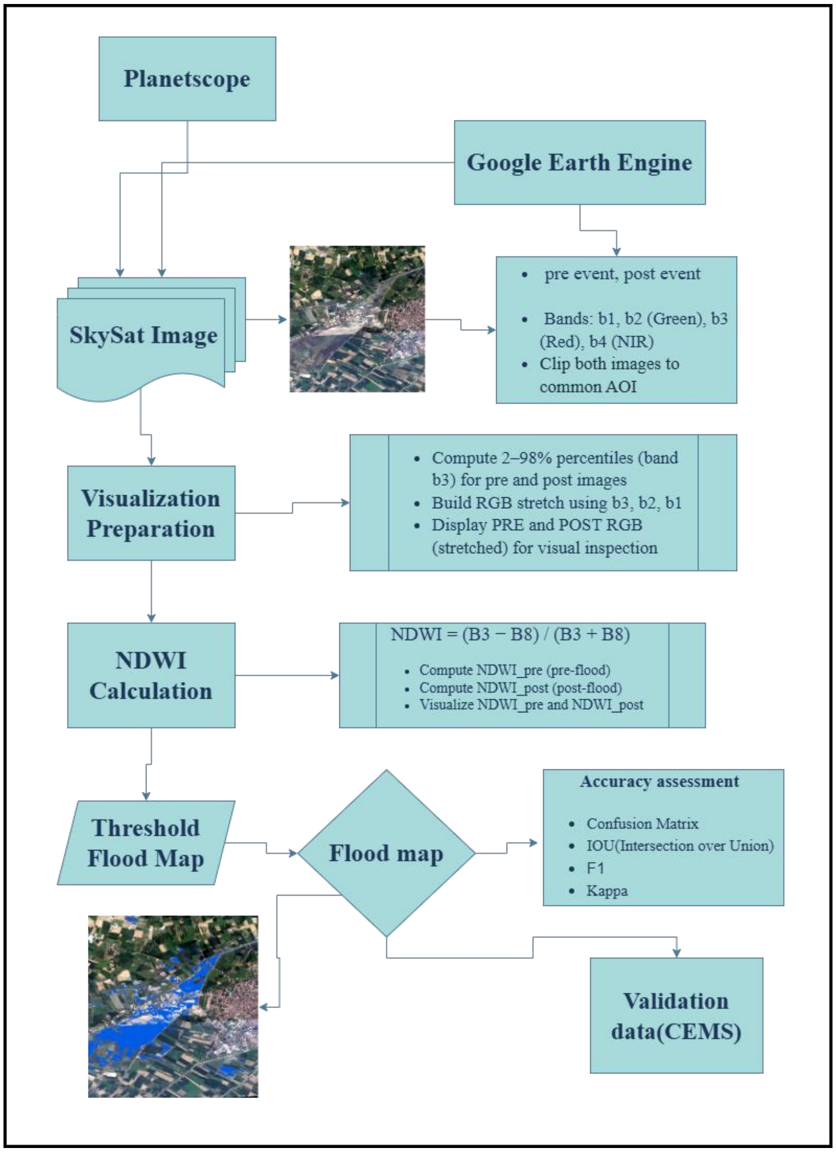

Figure 4-20 Skysat workflow diagram

1. Definition of AOI

The SkySat analysis is limited to the common AOI to ensure that pre-event and post-event products are spatially consistent and directly comparable with other sensor outputs. Pre-flood and post-flood SkySat scenes are provided as project assets and are loaded directly as ee.Image objects in GEE. The band structure is checked to confirm expected spectral channels before further processing.

2. Clipping AOI

Both SkySat scenes are clipped to the common AOI to ensure a consistent spatial extent for visualization, index calculation, and flood classification. Clipping at this stage guarantees that all subsequent statistics (e.g., percentiles), NDWI calculations, and threshold operations are performed only within the study area and are directly comparable between the pre-event and post-event images.

3. Visualization preparation

Visual inspection of very-high-resolution imagery depends on the display stretch applied to reflectance or radiance values. Rendering images without proper stretching can result in images that are too dark or overly saturated, especially when the dynamic range varies between pre-event and post-event acquisitions. To ensure consistent visualization, a robust strategy is used to generate comparable RGB images for inspection and figure creation. First, an automatic stretch is shown for quick quality assessment. Next, robust percentiles (2–98%) are calculated for the red band (b3) over the AOI separately for pre-event and post-event images. These percentile values set the minimum and maximum bounds for RGB visualization (using b3, b2, b1), minimizing the impact of outliers and ensuring consistent images for comparison between the two dates.

4. Permanent water extraction (Pre-event image)

The pre-event SkySat analytic surface reflectance (SR) product was used to identify permanent water bodies existing prior to the flood. The Normalized Difference Water Index (NDWI) was computed using the green (b2) and near-infrared (b4) bands by formula 4-1. A threshold-based classification was applied to the pre-event NDWI image to extract stable rivers and channels representing permanent water surfaces. The resulting binary permanent water mask was retained for subsequent filtering. It is important to note that the pre-event NDWI was used solely to define the spatial footprint of stable water bodies and was not employed for change detection analysis. Figure 4-21 shows the NDWI map for the pre-event condition.

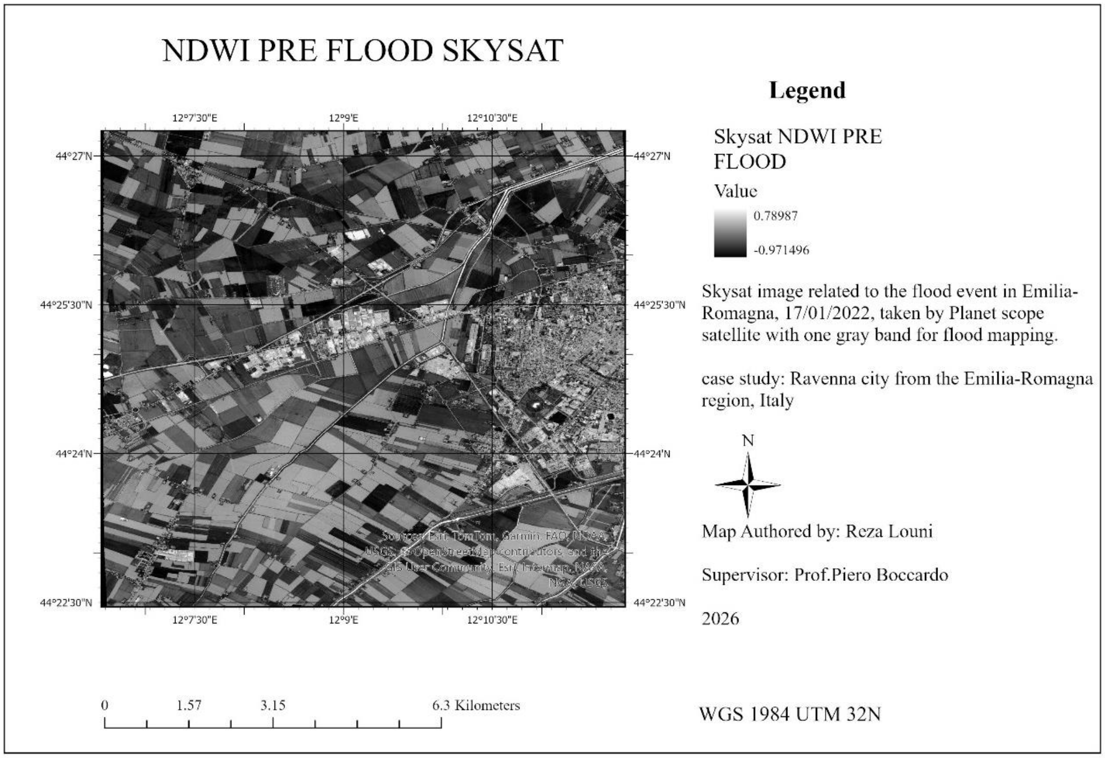

Figure 4-21 NDWI Skysat pre flood

5. Flood detection using post-event NDWI

Flood delineation was performed using the pansharpened multispectral SkySat product acquired after the event. The pansharpened dataset enhances spatial detail and improves the delineation of flood boundaries at sub-meter resolution. NDWI was computed from the post-event image using the same spectral bands (b2 and b4) (Figure 4-22). Flooded pixels were identified using a threshold-based rule applied to the post-event NDWI image. To isolate newly inundated areas, the permanent water mask derived from the pre-event image was removed from the post-event water classification. A pixel was therefore classified as flooded when:

- Post-event NDWI exceeded the calibrated threshold (0.15), and
- The pixel did not belong to the permanent water mask.

This logical masking approach ensures that only newly inundated areas are retained, while stable rivers and pre-existing water bodies are excluded from the final flood map. The threshold value was selected through iterative calibration based on visual inspection and spatial coherence of the resulting flood patterns. Lower thresholds resulted in overestimation due to wet soil and shadowed surfaces, whereas higher thresholds led to omission of shallow inundation zones.

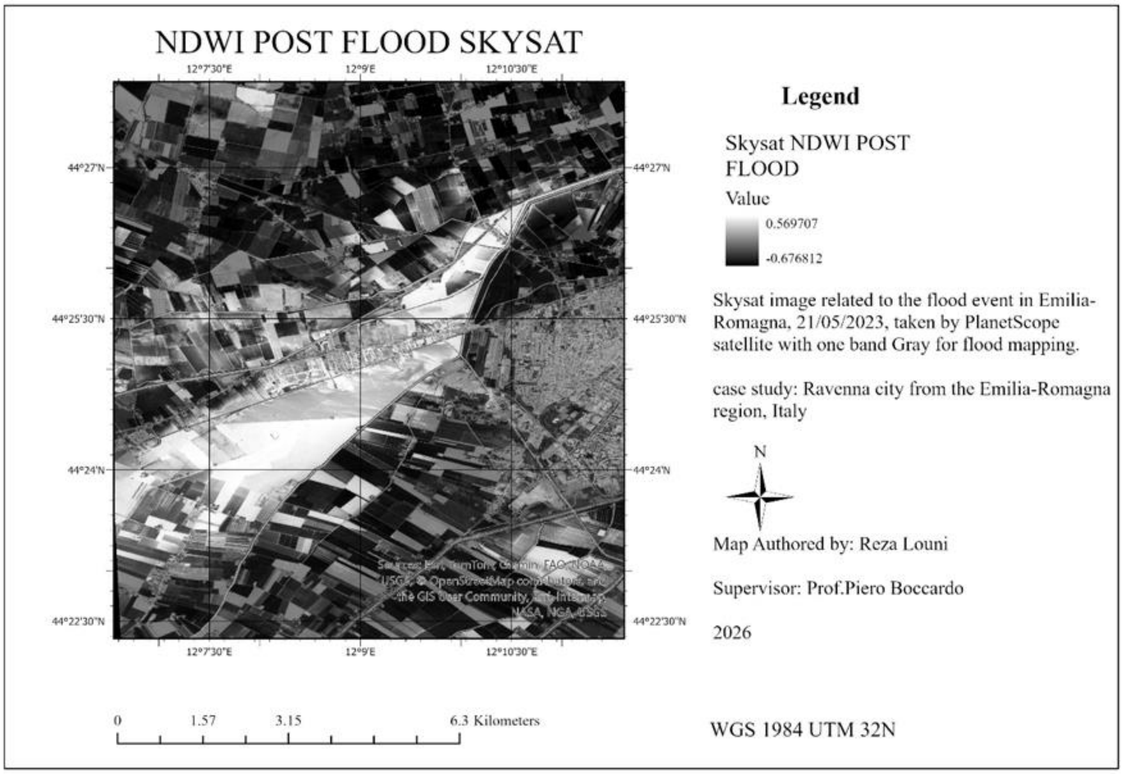

Figure 4-22 NDWI Skysat post flood

6. Export Skysat product

The SkySat outputs are exported from Google Earth Engine to support cartographic production and later analysis. Export operations use the common AOI as the export region and match the spatial resolution of the high-resolution SkySat imagery. Several products are exported to document the flood event and aid in interpreting the classification results. Specifically, three outputs are generated: a visually enhanced RGB rendering of the post-event image using robust percentile stretching for figure preparation; the NDWI layer, which highlights spectral changes caused by flooding; and the threshold-based flood mask derived from NDWI.

7. Binary flood mask and flooded-area estimation

After classifying floods based on thresholds, the flood mask is transformed into a clear binary raster (0/1) for consistent export and quantitative analysis. Flooded pixels receive a value of 1, while non-flooded pixels are assigned a value of 0. The flooded area is then calculated by multiplying the binary flood mask by pixel area and summing the flooded pixels within the AOI. Pixel areas are converted from square meters to square kilometers to provide an understandable measure of inundation extent. Finally, the binary flood mask is exported for future use.

4.6 FWDET (Flood Water Depth Estimation Tool) and volume estimation

Flood-extent maps derived from satellite imagery provide valuable information on the spatial distribution of inundation but do not directly quantify flood severity, which in this study is defined in terms of floodwater depth and associated water volume, rather than damage or event persistence. Areas exhibiting similar flood extents may experience substantially different impacts depending on water depth, which governs flow energy, potential damage to infrastructure, and floodplain storage capacity. To address this limitation, this study employs the Flood Water Depth Estimation Tool (FWDET) to estimate spatially distributed floodwater depth and to derive floodwater volume by combining satellite-based flood masks with terrain elevation data. FWDET is a terrain-based method that requires minimal inputs, a binary flood-extent layer, and a terrain model. Compared to physically based hydrodynamic models (e.g., 1D/2D shallow-water solvers), FWDET is computationally efficient and well-suited for large-scale or data-limited applications, where detailed hydraulic parameters (roughness, boundary conditions, channel geometry) and dense in-situ observations are unavailable. The method is therefore appropriate for regional-scale emergency mapping and comparative analyses, rather than for event-specific hydraulic reconstruction. FWDET assumes that terrain elevations along the boundary between flooded and non-flooded pixels approximate the local floodwater surface elevation. These boundary elevations are interpolated across the flooded area to generate a continuous floodwater surface. Floodwater depth is then calculated by subtracting the underlying terrain elevation from the interpolated water surface elevation at each pixel. In this study, FWDET is applied following the FWDET-GEE framework, enabling efficient processing within a cloud-computing environment and direct integration with satellite-derived flood masks. It is important to note that FWDET is not a dynamic hydraulic model and does not explicitly represent flow velocity, momentum exchange, inflow–

outflow processes, or temporal flood evolution. Its accuracy depends strongly on the quality of the flood mask and the terrain representation. Errors may arise in areas with disconnected flood compartments, complex hydraulic controls, urban drainage networks, or where flood boundaries are poorly defined. These limitations are acknowledged and are partially addressed in this study by systematically evaluating FWDET outputs across terrain datasets of increasing spatial resolution. To investigate the influence of terrain representation on floodwater depth and volume estimates, FWDET is applied using three elevation datasets with different spatial resolutions and characteristics. First, a global SRTM Digital Elevation Model (~30 m resolution) is used as a baseline terrain model, providing consistent regional coverage but limited ability to capture fine-scale floodplain morphology. Second, a LiDAR-derived Digital Terrain Model with 5 m resolution is employed, which better resolves local elevation gradients, riverbanks, embankments, and major anthropogenic features, while remaining computationally manageable for regional analysis. While individual road curbs and narrow linear features are not fully resolved at this resolution, the overall road embankment geometry and associated elevation contrasts are partially represented. Finally, a very-high-resolution LiDAR-derived Digital Terrain Model (0.5 m resolution) is used to capture micro-topographic features such as levees, drainage channels, small embankments, and subtle elevation variations that are often smoothed or entirely missed in coarser models. Using these multiple terrain datasets allows a systematic assessment of how terrain resolution influences FWDET-based floodwater depth patterns and derived floodwater volumes. In addition to spatially distributed depth estimation, FWDET outputs are used to compute floodwater volume as an integrated indicator of flood magnitude. Floodwater volume is calculated by multiplying the estimated depth at each flooded pixel by its corresponding pixel area and summing over the inundated region. Although simplified and dependent on the static flood mask, this approach provides a first-order approximation of floodplain water storage and is commonly adopted in large-scale flood assessments where detailed hydraulic simulations are not feasible. By jointly analyzing flood extent, floodwater depth, and floodwater volume across multiple terrain resolutions, this study provides a comprehensive and internally consistent framework for evaluating the sensitivity of FWDET outputs to terrain representation and for interpreting flood severity beyond inundation extent alone.

4.6.1 FWDET workflow and volume estimation in GEE

Floodwater depth estimation using FWDET is performed by combining a fixed binary flood-extent mask with terrain elevation models at different spatial resolutions. In this study, the flood-extent mask is derived from very-high-resolution SkySat imagery and is used consistently across all FWDET experiments, while the terrain representation is varied to assess the sensitivity of depth and volume estimates to elevation resolution. Specifically, FWDET is applied using a global SRTM Digital Elevation Model at 30 m resolution, a LiDAR-derived Digital Terrain Model at 5 m resolution, and a very-high-resolution LiDAR-derived Digital Terrain Model at 0.5 m resolution. By keeping the flood extent constant and changing only the terrain model, the workflow isolates the influence of terrain resolution on floodwater depth reconstruction. Before FWDET processing, each terrain dataset is clipped to a common Area of Interest and checked for elevation outliers. The flood mask is aligned to each terrain grid using nearest-neighbor resampling to preserve its binary nature. FWDET then extracts terrain elevations along the flood boundary, which are assumed to approximate the local floodwater surface height, and propagates these elevations across the flooded region using a cumulative-cost interpolation approach. Floodwater depth is obtained by subtracting the terrain elevation from the reconstructed water surface, and floodwater volume is computed by integrating depth over the flooded area. Despite the advantages of the FWDET approach, working with flood-extent and terrain datasets at different spatial resolutions introduces unavoidable limitations. Applying a high-resolution flood mask to coarser terrain models (e.g., the SRTM 30 m digital elevation model) may smooth or omit fine-scale topographic controls such as levees, embankments, roads, or drainage features, leading to generalized depth estimates. Conversely, combining coarser flood extents with finer terrain grids can introduce boundary inconsistencies where a single flood pixel spans heterogeneous micro-topography. In this study, these effects are mitigated by maintaining a consistent flood-extent definition and systematically varying only the terrain resolution. Nevertheless, residual discrepancies in floodwater depth near flood boundaries may persist, especially in areas with sharp elevation gradients. As a result, FWDET-derived depths and volumes should be interpreted as first-order approximations of flood severity rather than exact hydraulic reconstructions, with uncertainty increasing where resolution mismatches between flood extent and terrain representation are greatest.

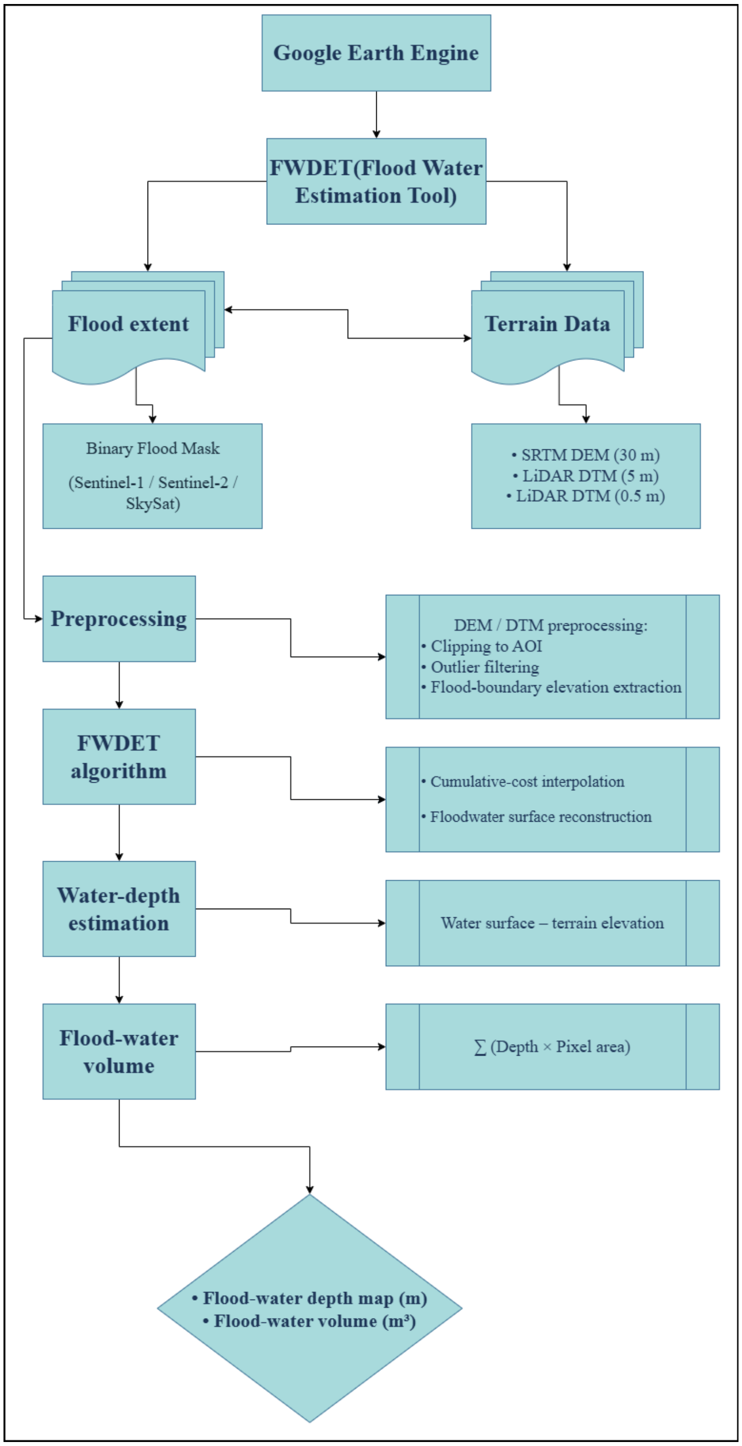

Figure 4-23 FWDET and Volume estimation workflow

1. Definition of input datasets in GEE

The FWDET workflow begins by defining two essential input datasets: the binary flood-extent mask and the terrain elevation model. The flood mask outlines the inundation area and is provided as a raster where flooded pixels are assigned a value of 1, and non-flooded pixels are assigned a value of 0. By masking out non-flooded pixels, all subsequent FWDET calculations are limited strictly to the identified flooded area. Simultaneously, terrain elevation data are specified through a digital elevation or terrain model. In this implementation, the SRTM DEM serves as the baseline elevation dataset, but the same workflow can be applied using LiDAR-derived DTMs at higher spatial resolutions (5 m and 0.5 m). The terrain model provides the ground surface reference necessary for reconstructing floodwater surface elevation and estimating floodwater depth and volume.

2. Definition of processing options and workflow parameters

Before executing the FWDET algorithm, a set of user-defined processing options is specified to manage optional preprocessing steps and output generation. These parameters do not modify the core FWDET methodology, which is based on reconstructing the floodwater surface from boundary elevations, but instead regulate how elevation data are prepared, how specific pixel classes are treated, and which intermediate and final outputs are produced. The selected processing options are partly derived from the original FWDET and FWDET-GEE methodological framework described in the scientific literature, and partly from practical considerations related to the characteristics of the input datasets and the study area. In particular, FWDET implementations commonly include options for elevation outlier filtering, permanent water masking, and zero-depth exclusion to improve numerical stability and reduce artifacts in large-scale applications. These steps are widely adopted in DEM-based flood-depth reconstruction workflows to limit the influence of spurious elevation values, noise at flood boundaries, and non-physical depth estimates. In this study, the parameter settings were refined through exploratory testing to ensure consistent behavior across terrain datasets with different spatial resolutions. Elevation outlier filtering was enabled to remove anomalous height values that could unrealistically propagate into the reconstructed floodwater surface. Permanent water masking was applied to prevent pre-existing water bodies from influencing depth estimation in newly flooded areas, while zero-depth pixels were excluded from volume calculations to avoid bias from marginal or non-inundated cells. By explicitly defining these processing options, the FWDET workflow remains flexible yet reproducible, allowing the same methodological structure to be consistently applied across different terrain representations and spatial scales. This parameterization supports both the transferability of the approach and the systematic evaluation of how terrain resolution influences FWDET-based floodwater depth and volume estimates.

3. Definition of the processing domain

The FWDET processing domain is defined dynamically based on the spatial footprint of the flooded area rather than using a fixed boundary. The geometry of the flood mask is converted into a bounding region and expanded with a buffer to include surrounding non-flooded terrain. This extra area is necessary because FWDET reconstructs the floodwater surface from elevations along the flood boundary and propagates these boundary conditions across the inundated domain. The resulting geometry serves as the common AOI for clipping terrain data and all subsequent spatial calculations.

4. Terrain data loading, clipping, and reference grid definition

After defining the processing area, the terrain elevation model is loaded and prepared for FWDET calculation. The terrain models include the SRTM digital elevation model (DEM, DSM-like 30m) and LiDAR Digital Terrain Models (5 & 0.5 m) of different resolutions that are imported, condensed to a single elevation band, and clipped to the AOI to ensure spatial consistency with the flood extent. The terrain dataset's projection is used as the reference grid for subsequent processing, and its nominal pixel size is extracted to set the working resolution for depth and volume calculations. This step is crucial because all FWDET-derived products are built on the elevation model grid, so the terrain models' resolution directly influences the spatial resolution of the estimated floodwater depth.

5. Optional permanent-water layer and flood-mask formatting for FWDET

Before executing the FWDET core algorithm, two supporting raster layers are optionally prepared to improve the robustness of floodwater depth estimation. First, a permanent-water layer derived from the JRC Global Surface Water (GSW) dataset is used to identify perennial water bodies. The

JRC GSW dataset is a long-term, globally consistent product generated from multi-decadal Landsat observations, which maps the spatial and temporal occurrence of surface water at 30 m resolution. In this study, the permanent-water information is used only as an auxiliary mask to optionally exclude stable, long-standing water bodies such as rivers, lakes, and reservoirs from the flood mask when the focus is on newly inundated areas. This step is not mandatory and is applied only when permanent water is expected to interfere with flood-depth reconstruction, particularly in areas where pre-existing water surfaces could bias the interpolation of floodwater boundary elevations. Second, the binary flood-extent map derived from satellite flood mapping is reformatted into the input structure required by FWDET. The flood mask is converted into a binary raster in which flooded pixels are assigned a value of one and non-flooded pixels are masked out. In this configuration, pixel values themselves are not interpreted as depth or intensity; instead, the mask strictly defines the spatial domain over which FWDET operations are performed. This ensures that floodwater surface interpolation and depth calculations are constrained exclusively to pixels classified as flooded, preventing the algorithm from propagating water surfaces into non-inundated areas. Together, the optional permanent-water masking and standardized flood-mask formatting improve numerical stability and reduce artifacts in FWDET outputs, while preserving flexibility to adapt the workflow to different study objectives and landscape conditions.

6. DEM outlier filtering

Elevation artifacts and abnormal values in terrain elevation models data can transfer into the reconstructed floodwater surface, creating unrealistic depth patterns especially near the flood boundary where FWDET uses its boundary conditions. An optional outlier filtering step is therefore included to stabilize the terrain input before water-surface reconstruction. This approach compares each pixel to a local median surface and detects outliers using a robust deviation metric. Detected anomalies are replaced with neighborhood median estimates. Additionally, a second pass is performed along an expanded flood boundary zone to minimize boundary-related elevation artifacts, which can significantly influence the subsequent interpolation step.

7. FWDET Algorithm

At this stage of the workflow, the floodwater surface elevation is reconstructed within the inundated area. The FWDET method assumes that water levels along the boundary of the flooded region are influenced by the surrounding terrain elevation. These boundary elevations, therefore, serve as reference conditions necessary to estimate the water surface inside the flooded domain. The reconstruction employs a cumulative-cost interpolation approach. Terrain elevations outside the flooded area are treated as source pixels, and their elevation values are propagated across the flooded region through a cost-based distance calculation. This process produces a continuous floodwater surface that smoothly transitions from the flood boundary toward the interior of the inundated area, while preventing unrealistic elevation gaps. The resulting raster displays the estimated floodwater surface elevation and provides the foundation for subsequent floodwater depth calculations.

8. Flood-water depth computation and post-processing

Floodwater depth is computed within the FWDET framework by subtracting the terrain elevation from the reconstructed floodwater surface elevation. The floodwater surface is not derived through an external interpolation tool; instead, it is reconstructed internally by FWDET using a cumulative cost–distance interpolation approach. In this method, terrain elevations at the boundary between flooded and non-flooded pixels are treated as control points that approximate the local floodwater surface height. These boundary elevations are then propagated inward across the flooded area using a least-cost accumulation algorithm, producing a continuous floodwater surface constrained by the flood-extent mask. Once the floodwater surface is reconstructed, water depth is calculated on a pixel-by-pixel basis as the difference between the floodwater surface elevation and the underlying terrain elevation, yielding a continuous depth field expressed in meters. To improve numerical stability and reduce small-scale artifacts introduced by terrain noise and boundary discretization, a light spatial smoothing step inherent to the FWDET post-processing workflow is applied to the depth surface. This operation is intentionally minimal and does not alter large-scale depth patterns or flood extent geometry. Negative depth values, which may arise locally due to interpolation uncertainty or terrain irregularities, are set to zero to ensure physical consistency. Finally, the depth layer is masked using the input binary flood-extent raster so that depth values are retained only within pixels classified as flooded. The resulting product is a spatially coherent flood-water depth map suitable for subsequent volume estimation and comparative analysis across different terrain resolutions.

9. Optional masking

After depth calculation, optional masking steps can be performed based on the analysis goal. Permanent water bodies can be filtered out using the JRC Global Surface Water layer, which prevents FWDET depth values from being assigned to perennial rivers, lakes, or reservoirs. Additionally, pixels with zero estimated depth can be removed to retain only positive water-depth values. Both steps are controlled by user-defined flags and are only applied if enabled.

10. Depth statistics for sanity checking

A basic diagnostic check involves determining the minimum and maximum values of the derived flood-water depth layer within the processing area. This step quickly confirms that the output depth values are reasonable and ensures the depth raster has been created correctly before volume calculation and export.

11. Flood-water volume derivation

Flood-water volume is calculated by adding the flood-water depth across the flooded area. The volume of each pixel is obtained by multiplying the flood-water depth (m) by the pixel area (m^2), giving a volume in cubic meters (m^3). The total flood-water volume is then found by summing all pixel volumes within the region using a regional aggregation method. For reporting, the results are provided both in cubic meters and in millions of cubic meters.

$$V = \sum_{i=1}^{N} h_i \cdot A_i \qquad (4\text{-}2)$$

Where:

- V is the total flood-water volume (m^3),
- $h_i$is the estimated flood-water depth at pixel i(m),
- $A_i$is the area of a pixel i(m^2),
- $N$is the total number of flooded pixels.

12. Visualization and export of FWDET outputs

The final outputs are visualized on the GEE map interface to facilitate qualitative inspection of the flood extent and the derived depth field. The flood mask appears as a binary layer, while floodwater depth is shown as a continuous raster with a graduated color ramp. The primary FWDET depth product is then exported to Google Drive at the terrain dataset's working resolution. Optional intermediate outputs (e.g., reconstructed water surface, terrain elevation model, and filtered terrain elevation raster) can also be exported as needed.

The same FWDET-GEE workflow described above was applied consistently across multiple terrain datasets to assess how elevation model resolution affects flood-water depth and volume estimates. Specifically, the procedure used the SRTM DEM (~30 m) as a baseline global elevation product, a LiDAR-derived DTM (5 m) representing a medium-resolution terrain model, and a very high-resolution LiDAR-derived DTM (0.5 m) capturing detailed floodplain topography. For each terrain dataset, the flood-extent mask and processing domain remained unchanged, while the DEM/DTM input layer, its native projection, and its working spatial resolution served as the reference grid for the FWDET steps. Consequently, differences in the resulting depth and volume outputs mainly reflect variations in terrain representation, including the ability to resolve small elevation gradients and local micro-topographic features that influence floodwater surface reconstruction and depth calculation.

4.7 Accuracy assessment

4.7.1 Accuracy-Assessment Workflow and Accuracy Metrics for flood maps

The accuracy of flood-extent maps derived from Sentinel-1, Sentinel-2, and SkySat imagery was quantitatively assessed using a vector-based accuracy assessment approach against independent reference datasets provided by the Copernicus Emergency Management Service (CEMS). This methodology was adopted to ensure consistency with the vector nature of the CEMS flood products and to avoid rasterization- and resampling-induced artifacts that may arise when comparing flood maps derived from sensors operating at different spatial resolutions.

Flood-extent products from Sentinel-1 and Sentinel-2 were validated against the CEMS Delineation Monitoring 3 (DM3) flood polygons, which were extracted in a semi-automatic manner from COSMO-SkyMed imagery (approximately 5 m spatial resolution). The SkySat flood map, characterized by very-high spatial resolution, was instead validated using the EMSR664 Grading AOI07 dataset, which corresponds to the Ravenna urban area and was manually delineated through photointerpretation from very-high-resolution optical imagery. The SkySat acquisition date was fully consistent with the CEMS delineation timeline, ensuring temporal coherence between prediction and reference datasets. Accuracy assessment was performed through a stratified random point-sampling strategy implemented in Google Earth Engine, conceptually equivalent to the Create Accuracy Assessment Points – Update Accuracy Assessment Points – Compute Confusion Matrix workflow commonly adopted in GIS-based accuracy analysis. Validation points were generated within the real study Area of Interest (AOI), rather than restricting the analysis to the reference flood extent alone, in order to ensure the presence of both flooded and non-flooded areas and to mitigate class-imbalance effects. Each point was labeled according to spatial intersection with the reference flood polygons and the corresponding sensor-derived flood map, and a confusion matrix was constructed for each product. Based on the confusion matrix, standard accuracy metrics were computed, including Overall Accuracy, Cohen's Kappa coefficient, Precision, Recall, F1-score, and Intersection over Union (IoU)(Russell G. Congalton, 1991). These metrics quantify complementary aspects of flood-mapping performance, capturing overall agreement, detection completeness, reliability of flooded-area classification, and spatial overlap between predicted and reference flood extents. Several sources of uncertainty may affect the accuracy-assessment results. Although the vector-based approach avoids rasterization and resampling artifacts by design, differences in geometric representation and boundary delineation between flood products remain a relevant source of uncertainty. The CEMS reference polygons are derived through semi-automatic or manual interpretation and may exhibit spatial generalization when compared with sensor-derived flood maps, particularly for very-high-resolution products such as SkySat. In addition, geometric coregistration uncertainty between datasets acquired by different sensors can lead to local discrepancies along flood boundaries, even when temporal alignment is ensured. Finally, the point-sampling strategy introduces a degree of sampling uncertainty, although the use of stratified sampling reduces its impact. These factors should be considered when interpreting the accuracy metrics, especially boundary-sensitive measures such as Intersection over Union (IoU).

1. Vector-Based Flood Representation

Flood-extent accuracy assessment does not require rasterization when both reference and prediction datasets are available in vector format. In this study, flood extent was represented using polygon geometries, preserving the original delineation of flooded areas and avoiding grid discretization effects. Let Pdenote a flood polygon dataset and let $S_i$represent a validation point with spatial coordinates (x_i, y_i). Each point was assigned a binary flood label based on its spatial relationship with the polygon dataset as:

$$L(S_i) = \begin{cases} 1, & \text{if } S_i \in P \\ 0, & \text{otherwise} \end{cases} \qquad \text{(4-3)}$$

where 1 indicates flooded conditions, and 0 indicates non-flooded conditions. In this study, flood polygons derived from Sentinel-1, Sentinel-2, and SkySat imagery were used directly as prediction layers, while reference flood extents were provided by CEMS Delineation Monitoring 3 for Sentinel-based products and by EMSR664 Grading AOI07 for SkySat. This vector-based representation avoids rasterization, resampling, and scale-locking, ensuring that geometric differences between datasets are preserved during accuracy assessment.

2. Sampling Strategy and Confusion Matrix Construction

Accuracy assessment was conducted using a stratified random point-sampling approach to address class imbalance commonly encountered in flood mapping, where non-flooded areas typically dominate the study area(R. G. Congalton, 1988). A total of 10,000 Validation points were randomly generated within the real Area of Interest (AOI) and stratified to ensure balanced representation of flooded (class 1) and non-flooded (class 0) conditions. For each sampled point, flood labels were independently assigned based on spatial intersection with the reference flood polygons and the corresponding sensor-derived flood polygons. This point-based comparison yielded four possible outcomes: true positives (TP), false positives (FP), false negatives (FN), and true negatives (TN). These outcomes were aggregated into a confusion matrix, which formed the basis for all subsequent accuracy metrics. The use of point-based evaluation allows accuracy to be quantified independently of raster grid resolution and minimizes boundary artifacts associated with pixel-level comparisons. All sampling and labeling operations were implemented in Google Earth Engine, ensuring reproducibility and consistency across all evaluated flood products(Sathyanarayanan, 2024).

- True Positives (TP): validation points located within flooded areas in both the reference dataset and the sensor-derived flood map
- False Positives (FP): validation points located within non-flooded areas in the reference dataset but classified as flooded in the sensor-derived flood map
- False Negatives (FN): validation points located within flooded areas in the reference dataset but classified as non-flooded in the sensor-derived flood map
- True Negatives (TN): validation points located within non-flooded areas in both the reference dataset and the sensor-derived flood map

These quantities serve as the foundation for all subsequent accuracy metrics reported in this study. The structure of the confusion matrix used for evaluation is shown in Table 4.5.

Table 4.5 – Confusion matrix used for flood extent accuracy assessment

Reference (CEMS)	Predicted Flood	Predicted non-flood
Flood	True Positive (TP)	False Negative (FN)
Non-Flood	False Positive (FP)	True Negative (TN)

3. Accuracy Metrics and Mathematical Definitions

All accuracy metrics were derived from the confusion matrix elements TP, FP, FN, and TN, which represent counts of validation points rather than raster pixels. Each metric quantifies a specific aspect of flood-mapping performance and ranges within a defined numerical interval. The combined use of multiple metrics allows a comprehensive evaluation of detection reliability, completeness, and spatial consistency between predicted and reference flood extents.

❖ Overall Accuracy (OA)

Overall Accuracy measures the proportion of all evaluated validation points that are correctly classified, including both flooded and non-flooded classes. It indicates the percentage of correctly classified samples out of the total number of evaluated samples and ranges from 0 to 1.

$$0 \leq \mathrm{OA} \leq 1$$

Higher Overall Accuracy values, approaching 1, indicate that most validation points are correctly classified, whereas lower values, close to 0, indicate a high rate of misclassification. In flood-mapping applications, however, Overall Accuracy can be artificially inflated due to class imbalance, since a large number of correctly classified non-flooded locations may mask poor detection of flooded areas. Therefore, although a high Overall Accuracy is desirable, it should not be interpreted in isolation and must be supported by class-specific and chance-corrected accuracy metrics.(Sathyanarayanan, 2024)

$$\mathrm{OA} = \frac{TP + TN}{TP + TN + FP + FN} \qquad (4\text{-}4)$$

❖ Cohen's Kappa coefficient **(κ)**

Cohen's Kappa coefficient (κ) measures the level of agreement between the predicted flood map and the reference dataset after accounting for agreement that may occur by random chance. Unlike Overall Accuracy, Kappa assesses classification skill by correcting for the influence of class prevalence and random agreement. The coefficient ranges from −1 to 1, where values close to 1 indicate strong agreement beyond chance, values around 0 indicate agreement no better than random classification, and negative values indicate systematic disagreement between prediction and reference.(Foody, 2020)

$$-1 \leq \kappa \leq 1$$

In flood-mapping applications, higher Kappa values are generally desirable because they indicate agreement that is not solely driven by the dominance of non-flooded areas. However, several studies have shown that Kappa can be misleading and strongly affected by class imbalance, particularly in datasets where one class largely dominates the landscape. In such cases, conservative flood-detection strategies with very low false-positive rates may yield low or near-zero Kappa values despite meaningful detection performance. Consequently, Kappa is considered a supporting metric in this study and is interpreted jointly with class-specific measures such as Precision, Recall, F1-score, and Intersection over Union (IoU).

Cohen's Kappa coefficient is computed as:

$$\kappa = \frac{P_o - P_e}{1 - P_e} \qquad (4\text{-}5)$$

where:

- P_o is the observed agreement, defined as the proportion of correctly classified validation points:

$$P_o = \frac{TP + TN}{TP + FP + FN + TN}$$

- P_e is the expected agreement by chance, estimated from the marginal totals of the confusion matrix. For a binary classification (flood / non-flood), P_e is given by:

$$P_e = \frac{(TP + FP)(TP + FN) + (FN + TN)(FP + TN)}{(TP+FP+FN+TN)^2}$$

The terms in the numerator represent the expected agreement for the flooded and non-flooded classes, respectively, under random classification.(Foody, 2020)

❖ Precision (Positive Predictive Value)

Precision quantifies the reliability of flood detections by measuring the proportion of validation points correctly classified as flooded out of all points predicted as flooded. Precision ranges from 0 to 1, where higher values indicate that most locations identified as flooded correspond to truly inundated areas, while lower values indicate a high number of false flood detections.

$$0 \leq \text{Precision} \leq 1$$

In flood-mapping applications, a high Precision value is desirable because it indicates a low false-alarm rate and minimal overestimation of flood extent. Conversely, low Precision values suggest that many non-flooded locations are incorrectly identified as flooded, leading to overestimated flood extents. Precision is primarily sensitive to commission errors (false positives) and therefore emphasizes a method's tendency to overpredict flooding.(Sathyanarayanan, 2024)

$$\text{Precision} = \frac{TP}{TP + FP} \qquad (4\text{-}6)$$

❖ Recall (Sensitivity)

Recall measures the ability of the flood-mapping method to accurately identify flooded areas by calculating the proportion of truly flooded validation points that are successfully detected. Recall ranges from 0 to 1, where higher values indicate that most flooded locations are correctly identified, and lower values indicate that a significant number of flooded locations are missed.

$$0 \leq \text{Recall} \leq 1$$

In flood-mapping applications, a high Recall value is particularly important because it reduces omission errors and lowers the risk of missing inundated areas that may be critical for emergency response and damage assessment. Conversely, low Recall values indicate that many flooded regions are not identified by the flood map, leading to an underestimation of the flood extent. Recall is primarily influenced by omission errors (false negatives) and therefore reflects the completeness of flood detection.(Sathyanarayanan, 2024)

$$\text{Recall} = \frac{TP}{TP + FN} \qquad (4\text{-}7)$$

❖ F1-score

The F1-score provides a balanced measure of flood-mapping performance by combining Precision and Recall through their harmonic mean. The F1-score ranges from 0 to 1, where higher values indicate that both overestimation (false positives) and underestimation (false negatives) are simultaneously low, while lower values indicate a poor balance between these two types of errors. A high F1-score is therefore desirable, as it reflects reliable and comprehensive detection of flooded areas.

$$0 \leq \mathrm{F1} \leq 1$$

In flood-mapping applications, the F1-score is especially useful because it penalizes excessive bias toward either overprediction or underprediction and provides a single summary measure of detection quality. Conversely, a low F1-score indicates that either Precision or Recall (or both) is low, meaning that the flood map exhibits significant commission errors, omission errors, or an unfavorable trade-off between the two.(Sathyanarayanan, 2024)

$$\mathrm{F1} = \frac{2 \cdot \mathrm{Precision} \cdot \mathrm{Recall}}{\mathrm{Precision} + \mathrm{Recall}} \qquad (4\text{-}8)$$

❖ Intersection over Union (IoU)

The Intersection over Union (IoU), also referred to as the Jaccard Index, measures the degree of agreement between the predicted flood extent and the reference flood extent based on the proportion of correctly detected flooded locations relative to all locations classified as flooded in either dataset. IoU ranges from 0 to 1, where higher values indicate stronger agreement between prediction and reference, and lower values indicate limited overlap.

$$0 \leq \mathrm{IoU} \leq 1$$

A high IoU value is desirable because it indicates that flooded locations identified by the prediction closely correspond to those in the reference dataset. Conversely, a low IoU value reflects discrepancies caused by either overestimation (false positives) or underestimation (false negatives) of flood extent. In this study, IoU is computed using the confusion matrix derived from validation points and therefore reflects agreement in flood classification rather than pixel-level spatial correspondence. Intersection over Union is considered a strict metric because it penalizes both commission and omission errors simultaneously. As a result, even moderate imbalances between false positives and false negatives can substantially reduce IoU values. For this reason, IoU provides a robust measure of overall flood-detection consistency and is particularly useful for comparing flood extent products derived from different sensors or spatial supports.(Sathyanarayanan, 2024)

$$\mathrm{IoU} = \frac{TP}{TP + FP + FN} \qquad (4\text{-}9)$$

4. Output and Reproducibility

All steps of the accuracy assessment were executed programmatically within Google Earth Engine, ensuring a fully automated and reproducible workflow. For each flood product, confusion matrix elements and derived accuracy metrics were stored in structured feature collections and exported as CSV files. These outputs enable transparent reporting and facilitate further analysis and visualization outside the GEE environment.

Limitations and Uncertainty of the Accuracy Assessment

Despite the use of a consistent and fully reproducible vector-based accuracy-assessment workflow, several sources of uncertainty and limitations should be acknowledged when interpreting the obtained results. First, co-registration uncertainty between flood products and reference datasets represents an inherent source of error. Flood extent maps derived from different sensors rely on distinct geolocation accuracies, acquisition geometries, and preprocessing chains. Even small horizontal misalignments between sensor-derived flood polygons and reference flood polygons may lead to discrepancies in point-based classification, particularly along flood boundaries. These effects can propagate into confusion matrix metrics and may partially explain mismatches between predicted and reference flood extents. Second, reference data generalization constitutes a key limitation. The CEMS Delineation Monitoring 3 product, used as a reference for Sentinel-1 and Sentinel-2 validation, is generated through semi-automatic procedures at medium spatial resolution. As a result, fine-scale inundation features detectable by higher-resolution sensors may be absent or generalized in the reference dataset. Conversely, the EMSR664 Grading product AOI07, used for SkySat validation, is manually delineated from very-high-resolution optical imagery and therefore captures more detailed flood patterns. These differences imply that accuracy metrics are conditioned not only by sensor performance but also by the spatial detail and interpretation strategy of the reference data. Third, the vector-based, point-sampling approach adopted in this study avoids rasterization and pixel-resampling effects but introduces its own constraints. Accuracy metrics reflect agreement at discrete validation-point locations rather than continuous spatial correspondence across entire flood polygons. Consequently, metrics such as IoU and F1-score quantify classification consistency rather than exact geometric overlap, and small-scale boundary discrepancies may disproportionately affect results depending on point distribution. Finally, class imbalance effects remain relevant despite stratified sampling. Flooded areas typically occupy a smaller proportion of the AOI compared to non-flooded regions, and although stratification mitigates this imbalance, metrics such as Cohen's Kappa may still be sensitive to class prevalence and conservative detection strategies. Overall, these limitations do not invalidate the accuracy assessment but highlight the importance of interpreting results in the context of sensor resolution, reference-map characteristics, and spatial uncertainty. For this reason, the reported accuracy metrics are interpreted comparatively across sensors and are complemented by qualitative analysis of flood delineation behavior.

4.7.2 Accuracy assessment Workflow and Accuracy Metrics for flood-depth

Flood-depth accuracy assessment was implemented entirely within the Google Earth Engine environment using the EMSN-154 water-depth product as an independent reference dataset. All datasets were spatially clipped to a common Area of Interest defined by the AOI geometry. The EMSN-154 depth raster was retained in its native spatial resolution and projection and used as the reference spatial framework for validation. FWDET-derived flood-depth maps produced using different terrain model configurations (30 m, 5 m, and 0.5 m) were geometrically aligned to the EMSN-154 reference grid to enable direct value comparison. This alignment step was applied only to the final FWDET depth outputs and did not involve any resampling or modification of the underlying terrain models used in the FWDET processing chain, nor any aggregation or alteration of the EMSN-154 reference dataset. As such, the reference water-depth product preserves its original spatial characteristics throughout the validation. Validation was restricted to flooded conditions by masking the EMSN-154 dataset to locations with positive water depth values. The comparison domain was further limited to areas where both FWDET-derived and EMSN-154 depths were greater than zero, ensuring that accuracy metrics were computed exclusively over coincident inundated locations. Within this common flooded domain, depth residuals were calculated as the difference between FWDET-derived depths and EMSN-154 reference depths. To derive robust statistical estimates while maintaining computational efficiency, 10,000 random validation points was generated within the common flooded domain. At each validation point, paired reference depth, FWDET-derived depth, and depth residual values were extracted. These residuals formed the basis for computing Bias (mean signed error), Mean Absolute Error (MAE), and Root Mean Square Error (RMSE)(Chai & Draxler, 2014; Cort J. Willmott, 2005; D. N. Moriasi, 2007), allowing assessment of systematic deviations, typical depth errors, and sensitivity to localized extreme discrepancies across the different FWDET depth configurations(Teng et al., 2022b). All metrics were computed programmatically within GEE and stored in structured outputs for subsequent analysis and reporting.

Accuracy Metrics and Mathematical Definitions for Water-Depth Validation

❖ Bias (Mean Error)

Bias quantifies the systematic tendency of the FWDET-derived flood-depth estimates to overestimate or underestimate water depth relative to the reference dataset. It is defined as the mean signed difference between estimated and observed depths and is expressed in meters. Bias values can be either positive or negative, with positive values indicating systematic overestimation and negative values indicating systematic underestimation of flood depth. The metric theoretically ranges from negative infinity to positive infinity, although values close to zero are desirable, as they indicate the absence of systematic error. While Bias is useful for identifying directional tendencies in depth estimation, it does not convey information about the magnitude of errors, since positive and negative deviations may cancel each other out. For this reason, Bias is interpreted in conjunction with absolute error metrics.(D. N. Moriasi, 2007)

$$\text{Bias} = \frac{1}{n}\sum_{i=1}^{n}\left(D_i^{FWDET} - D_i^{EMSN}\right) \qquad (4\text{-}10)$$

- Mean Absolute Error (MAE)

The Mean Absolute Error represents the average magnitude of the differences between FWDET-derived flood depths and the reference depths, irrespective of error sign. MAE is expressed in meters and ranges from zero to positive infinity, with values approaching zero indicating higher accuracy. This metric provides an intuitive measure of the typical expected depth error and is less sensitive to extreme outliers than RMSE. In the context of operational flood mapping, lower MAE values indicate more reliable depth estimates and improved consistency with the reference dataset, making MAE particularly suitable for assessing overall flood-depth performance.(Chai & Draxler, 2014; Cort J. Willmott, 2005)

$$\text{MAE} = \frac{1}{n}\sum_{i=1}^{n} \mid D_i^{FWDET} - D_i^{EMSN} \mid \qquad (4\text{-}11)$$

- Root Mean Square Error (RMSE).

The Root Mean Square Error measures the dispersion of depth errors by giving greater weight to larger deviations through the squaring of individual errors prior to averaging. RMSE is expressed in meters and, like MAE, ranges from zero to positive infinity, with lower values indicating better agreement between estimated and reference depths. Because RMSE penalizes large errors more strongly than MAE, it is especially sensitive to localized discrepancies that may occur near flood boundaries, in areas with steep topographic gradients, or within complex urban environments. RMSE values substantially higher than MAE suggest the presence of localized extreme errors rather than a widespread degradation of depth estimation performance. (Chai & Draxler, 2014; Cort J. Willmott, 2005)

$$\text{RMSE} = \sqrt{\frac{1}{n}\sum_{i=1}^{n}\left(D_i^{FWDET} - D_i^{EMSN}\right)^2} \qquad (4\text{-}12)$$

Limitations and Uncertainty of Water-Depth Accuracy Assessment

The accuracy assessment of FWDET-derived flood-depth estimates is subject to several sources of uncertainty that should be considered when interpreting the results. First, the spatial resolution mismatch between the FWDET outputs and the EMSN-154 reference dataset represents an inherent limitation. While the EMSN-154 water-depth product is provided at 5 m spatial resolution, FWDET depth estimates may be derived using terrain models of different resolutions. As a result, very-high-resolution terrain information can capture fine-scale topographic variability that is not fully represented in the reference dataset, potentially leading to localized discrepancies in depth values. Second, geometric coregistration uncertainty between flood extent boundaries, terrain models, and the reference water-depth product may affect depth comparisons, particularly near flood margins. Small horizontal misalignments between datasets can propagate into vertical depth differences when depth is estimated relative to local terrain, especially in areas with steep elevation gradients or complex urban morphology. Third, the reference water-depth product itself is subject to uncertainty. The EMSN-154 dataset represents an operational emergency mapping product derived from remote sensing and hydraulic assumptions, rather than direct in-situ measurements. Consequently, reference depths may include uncertainties related to sensor limitations, model assumptions, and post-processing procedures, which inevitably influence the validation results. Finally, the validation was restricted to locations where both FWDET and EMSN-154 reported non-zero water depth. While this ensures that comparisons are made only over inundated areas, it limits the assessment to flooded pixels and does not account for uncertainty in flood extent delineation. For these reasons, the reported accuracy metrics should be interpreted comparatively across terrain model configurations rather than as absolute measures of flood-depth correctness.

Chapter 5: Results and Discussion

5.1 Outcomes of the multi-sensor flood-extent mapping

The outcomes of the multi-sensor flood-extent mapping are presented to assess the effectiveness of satellite-based observations in supporting flood emergency management and rapid response activities**.** Flood maps derived from Sentinel-1 SAR, Sentinel-2 optical imagery, and high-resolution SkySat data are analyzed and compared in terms of their spatial representation of inundation, sensitivity to applied thresholds, and agreement with the Copernicus Emergency Management Service reference delineation. The focus is placed on understanding how each sensor contributes to timely flood detection under different observation conditions, with particular attention to data availability, robustness to atmospheric constraints, and spatial detail. By evaluating and comparing these sensors within a consistent framework, this analysis aims to identify their respective strengths, limitations, and complementary roles, thereby informing the selection of appropriate satellite data sources for operational flood monitoring and emergency decision-making.

1. Sentinel 1 SAR Results

Flood extent derived from Sentinel-1 SAR represents the most conservative inundation estimate among the evaluated sensors. The final Sentinel-1 flood mask delineates a total flooded area of approximately 2.08 km², with inundation primarily detected in open, low-lying agricultural areas and along the main floodplain corridors. These zones exhibit a clear SAR water signature, allowing consistent identification of well-defined flooded surfaces. The Sentinel-1 flood-extent map is shown in Figure 5-1. Flooded areas appear as spatially coherent patches concentrated within the floodplain, while detections outside these zones are limited. This spatial pattern reflects the conservative behavior of SAR-based flood mapping, which prioritizes reliable identification of open water surfaces and minimizes false positives through post-processing and spatial filtering.

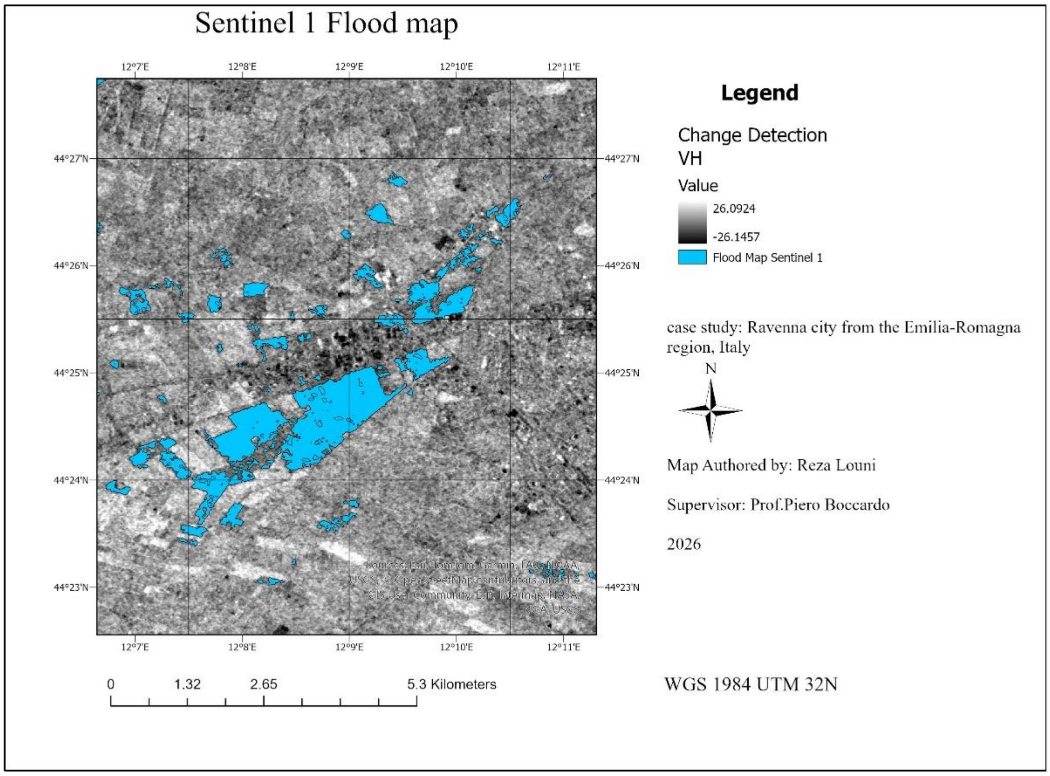

Figure 5-1: Sentinel-1 SAR flood-extent map derived from VH backscatter change detection and threshold-based classification. Flooded areas were identified using a post-event backscatter threshold of −19 dB, a permanent water threshold of −22 dB, and a change-detection threshold of −1.5 dB, with small, isolated clusters removed using connected-pixel filtering.

Validation against the Copernicus Emergency Management Service (CEMS) flood delineation is presented in Figure 5-2. Visual comparison indicates strong spatial agreement in open flooded areas and along major floodplain corridors, confirming reliable detection of clearly inundated surfaces. In contrast, discrepancies are mainly characterized by omission of flooded areas in vegetated, urban, and heterogeneous land-cover environments, where shallow inundation and partial vegetation cover reduce the separability of water surfaces in SAR imagery.

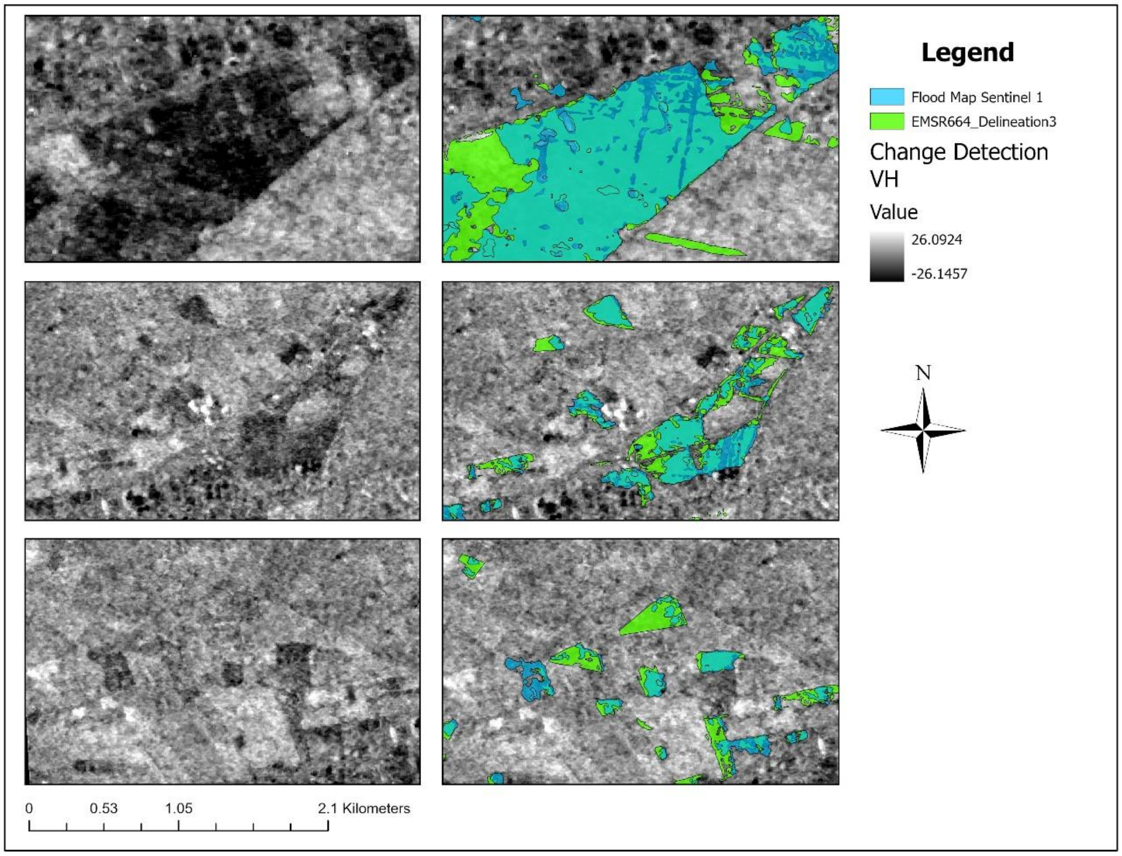

Figure 5-2: Visual comparison between the Sentinel-1 SAR flood-extent map and the Copernicus Emergency Management Service (CEMS) reference flood delineation over the study area. Agreement is strongest in open flooded zones, while discrepancies occur mainly in vegetated and complex land-cover areas.

2. Sentinel-2 Results

Flood extent derived from Sentinel-2 optical imagery shows a substantially larger and more spatially continuous inundation pattern compared to Sentinel-1. The final Sentinel-2 flood mask delineates a total flooded area of approximately 4.97 km^2**,** capturing widespread inundation across agricultural fields, floodplain margins, and secondary drainage features. The Sentinel-2 flood-extent map is shown in Figure 5-3. Flooded areas appear as continuous zones along the main floodplain and extend into shallowly inundated regions that are not fully represented in the SAR-based product. The spatial continuity of the mapped inundation highlights the sensitivity of optical imagery to shallow and spatially connected flooding under cloud-free conditions.

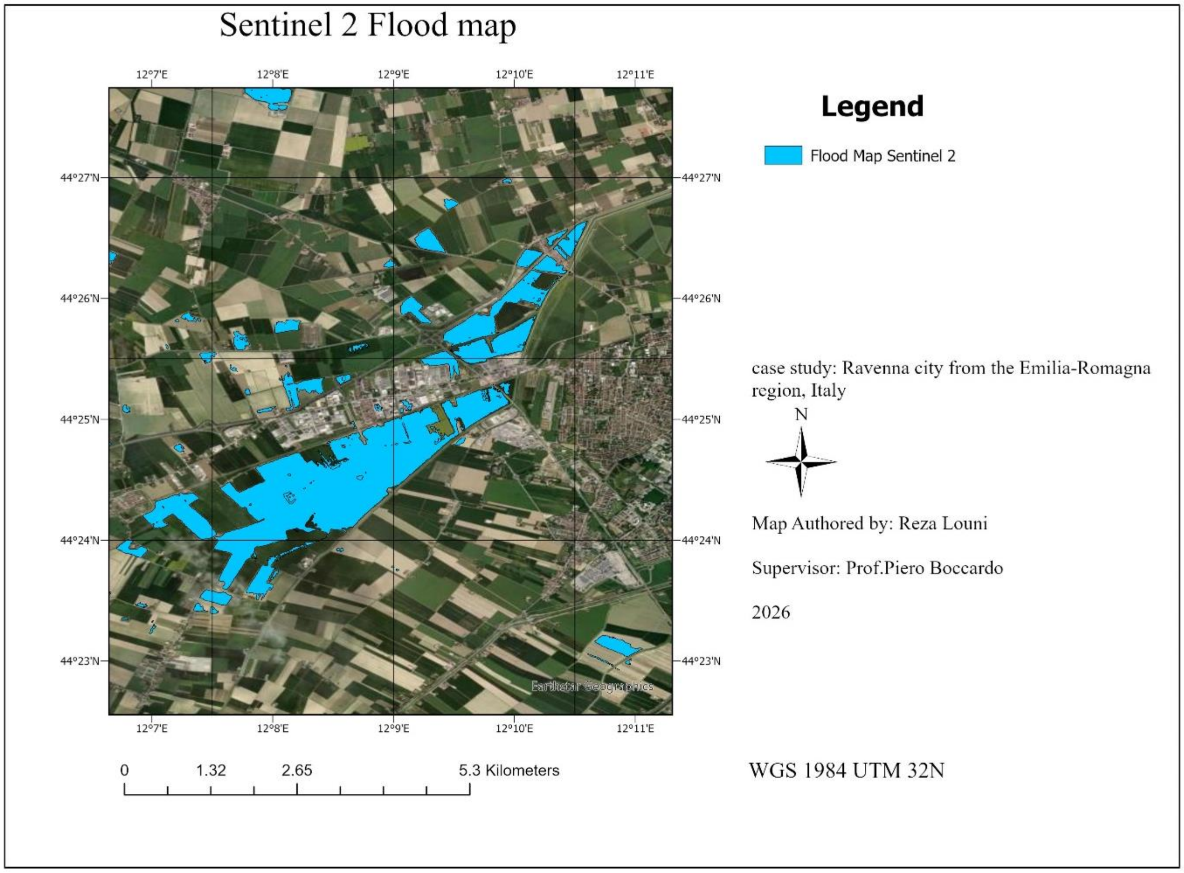

Figure 5-3: Sentinel-2 flood-extent map derived from NDWI change detection using a threshold of ΔNDWI ≥ 0.15. Flooded areas are highlighted based on increased post-event water spectral response.

Validation against the Copernicus Emergency Management Service (CEMS) flood delineation is presented in Figure 5-4. Visual comparison shows strong spatial correspondence across the main inundated areas and along floodplain corridors, with Sentinel-2 capturing a larger fraction of flooded surfaces relative to Sentinel-1. Improvements are particularly evident in shallow inundation zones and flood margins, where omission errors observed in SAR-based mapping are reduced.

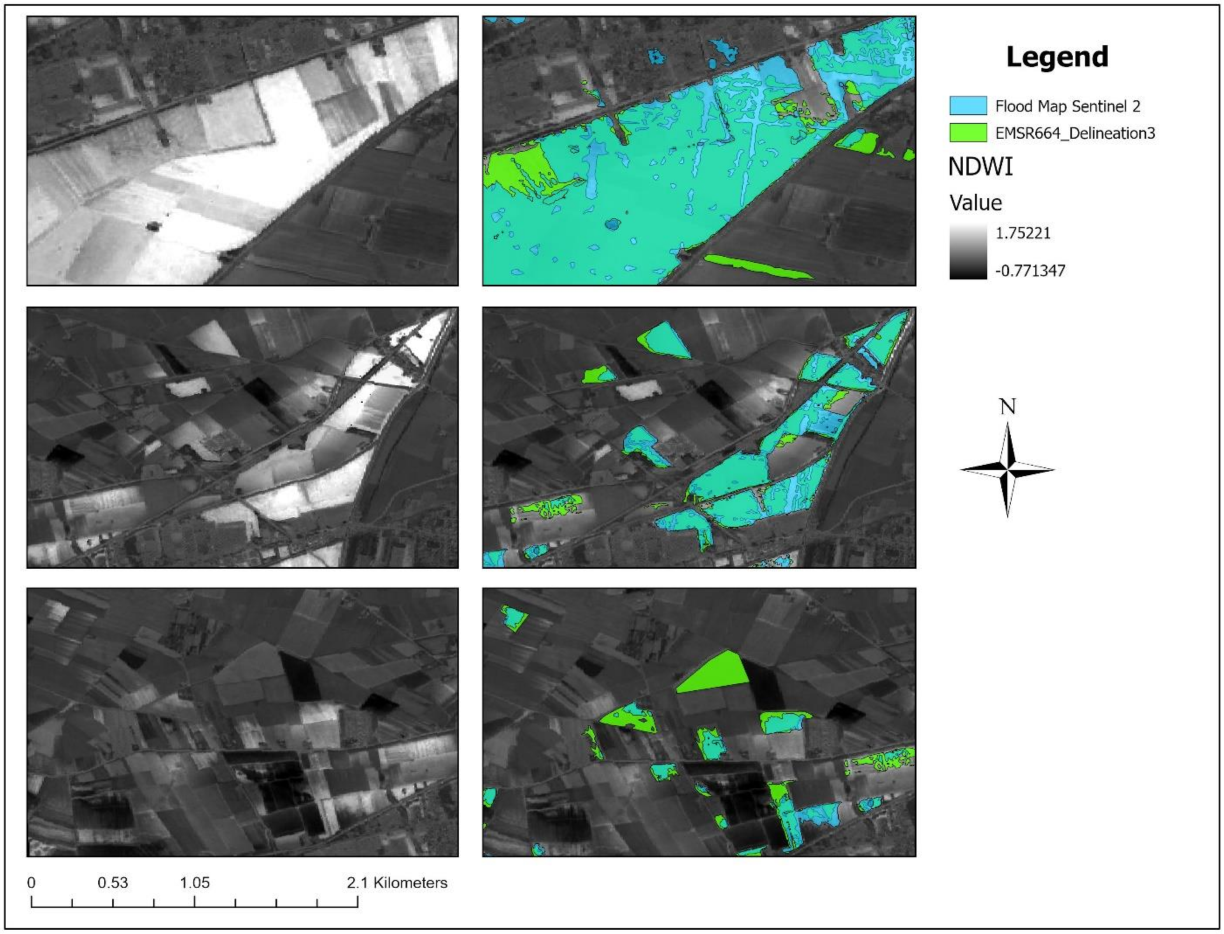

Figure 5-4: Visual comparison between the Sentinel-2 flood-extent map and the Copernicus Emergency Management Service (CEMS) reference flood delineation over the study area, showing strong agreement in open and shallowly inundated areas.

To support detailed visual interpretation, the Sentinel-2 flood extent is shown over different background layers in Figures 5-5 and 5-6. In Figure 5-5, the flood mask is overlaid on the NDWI background, illustrating the spatial correspondence between high water-related spectral response and the mapped inundation. In Figure 5-6, the same flood extent is displayed on the post-event Sentinel-2 optical image, enabling direct visual confirmation of flooding relative to recognizable land-cover features such as agricultural parcels, channels, and built-up areas. These views confirm that the mapped flood extent is spatially consistent with both spectral indicators of water presence and the observed surface conditions.

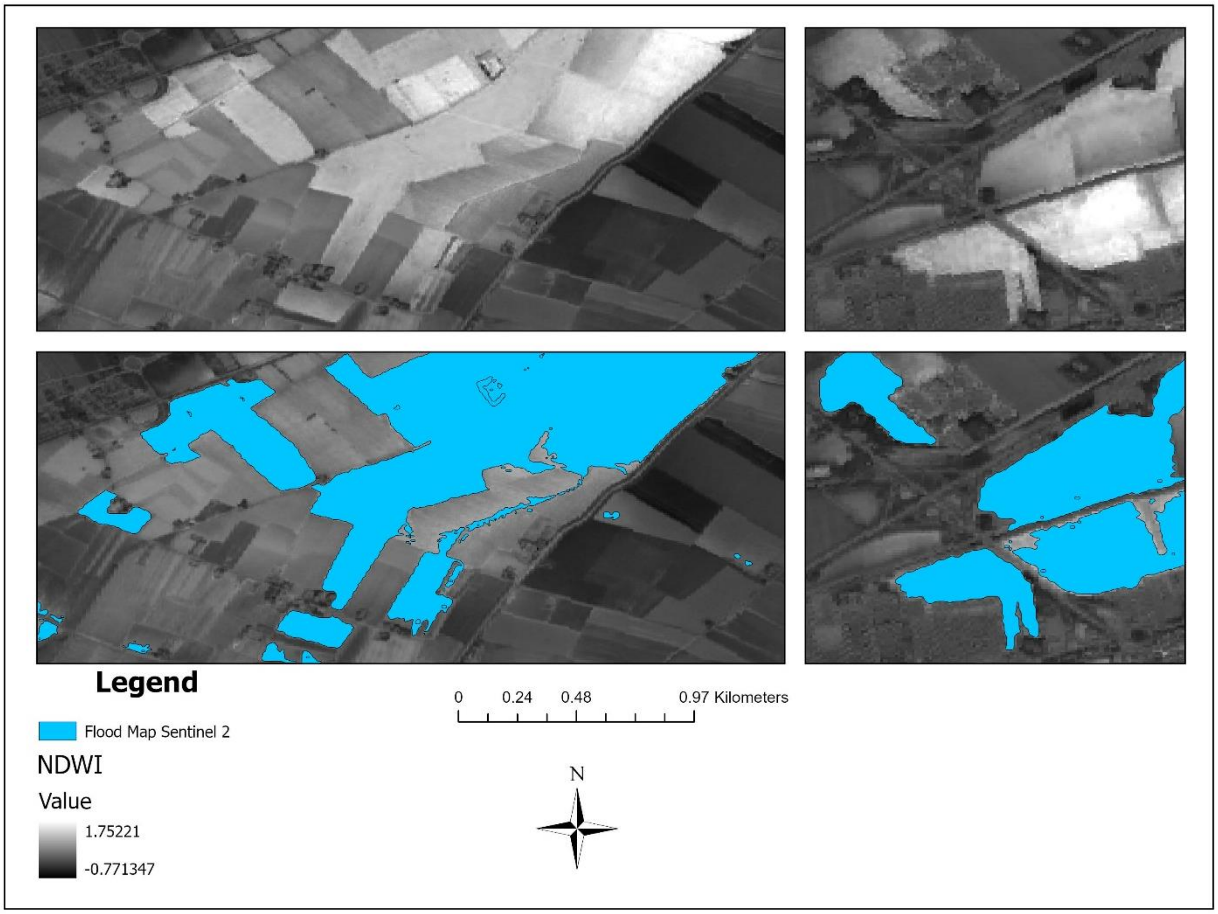

Figure 5-5: Sentinel-2 flood extent (ΔNDWI ≥ 0.15) overlaid on the NDWI background for selected detail areas, illustrating the consistency between elevated NDWI values and the classified inundation.

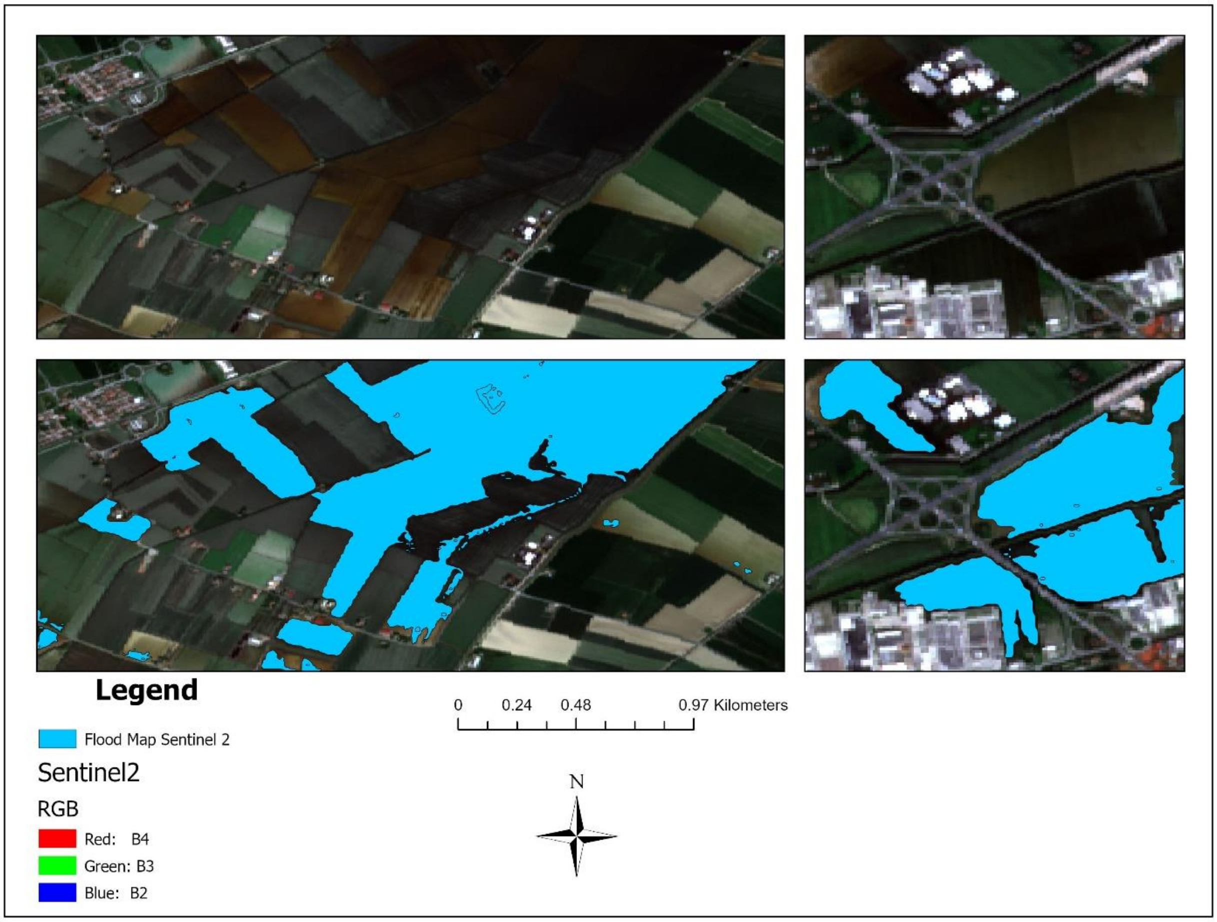

Figure 5-6: Sentinel-2 flood extent (ΔNDWI ≥ 0.15) overlaid on the post-event Sentinel-2 optical background for the same detail areas, supporting visual interpretation of the mapped inundation relative to land-cover features.

3. Skysat Results

Flood extent derived from very-high-resolution SkySat imagery represents the most spatially detailed inundation product among the evaluated sensors. The final SkySat flood mask delineates a total flooded area of approximately 7.41 km², capturing both the main floodplain inundation and a wide range of fine-scale flood features that are not fully resolved in medium-resolution products. The SkySat flood-extent map is shown in Figure 5-7. Flooded areas are mapped with sharp boundaries and high spatial continuity, revealing narrow flooded features, small depressions, localized ponding, and detailed flood margins. This level of spatial detail enables explicit representation of inundation patterns within urban, peri-urban, and heterogeneous land-cover environments, where mixed pixels and spatial generalization affect coarser sensors.

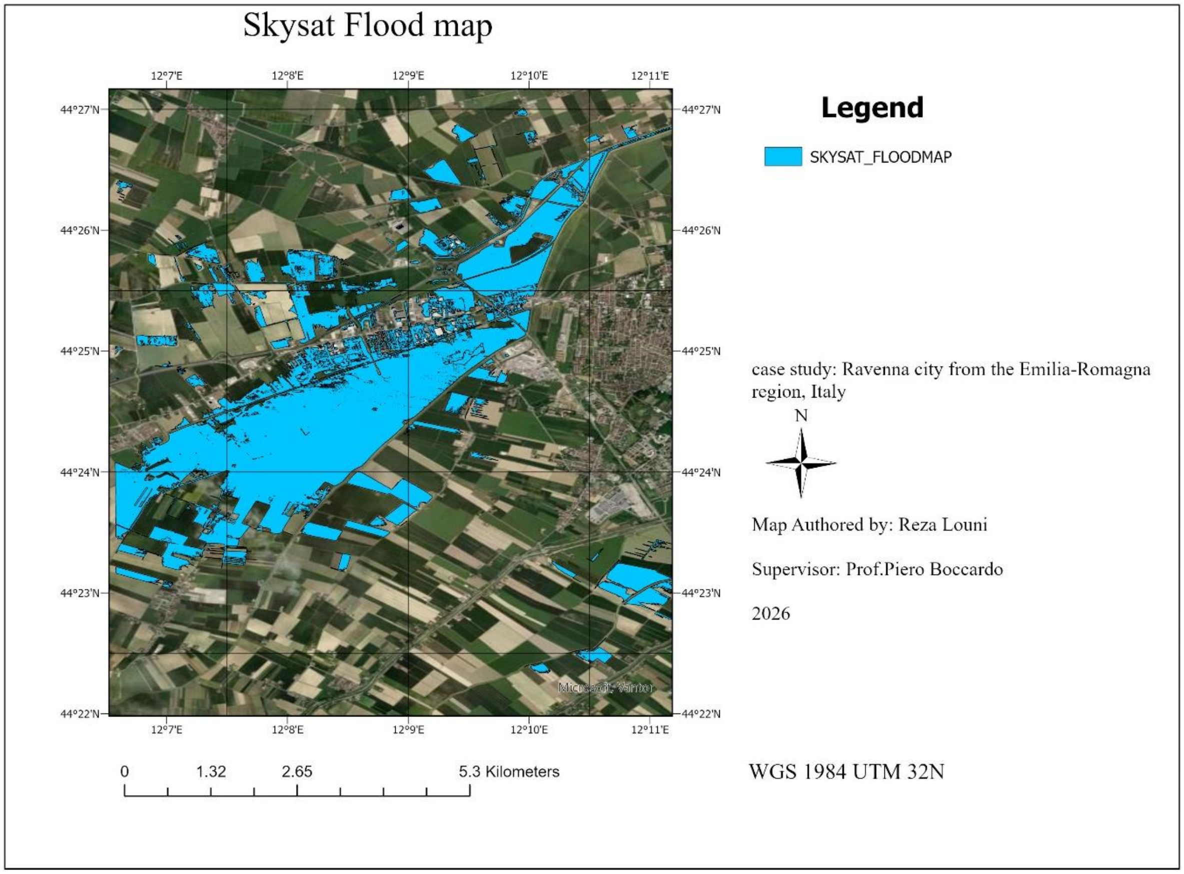

Figure 5-7: SkySat flood-extent map derived from NDWI change detection using a threshold of $\Delta NDWI \geq 0.15$, highlighting detailed inundation patterns at very-high spatial resolution.

Validation against the Copernicus Emergency Management Service (CEMS) related to the grading AOI-07 of Ravenna province flood delineation is presented in Figure 5-8. Visual comparison indicates strong spatial agreement across the main inundated areas, while SkySat additionally identifies localized flooding in areas characterized by complex land cover and built-up structures. In several locations, SkySat resolves fine-scale flood patterns that are spatially generalized or omitted in the CEMS reference, reflecting differences in spatial resolution rather than misclassification.

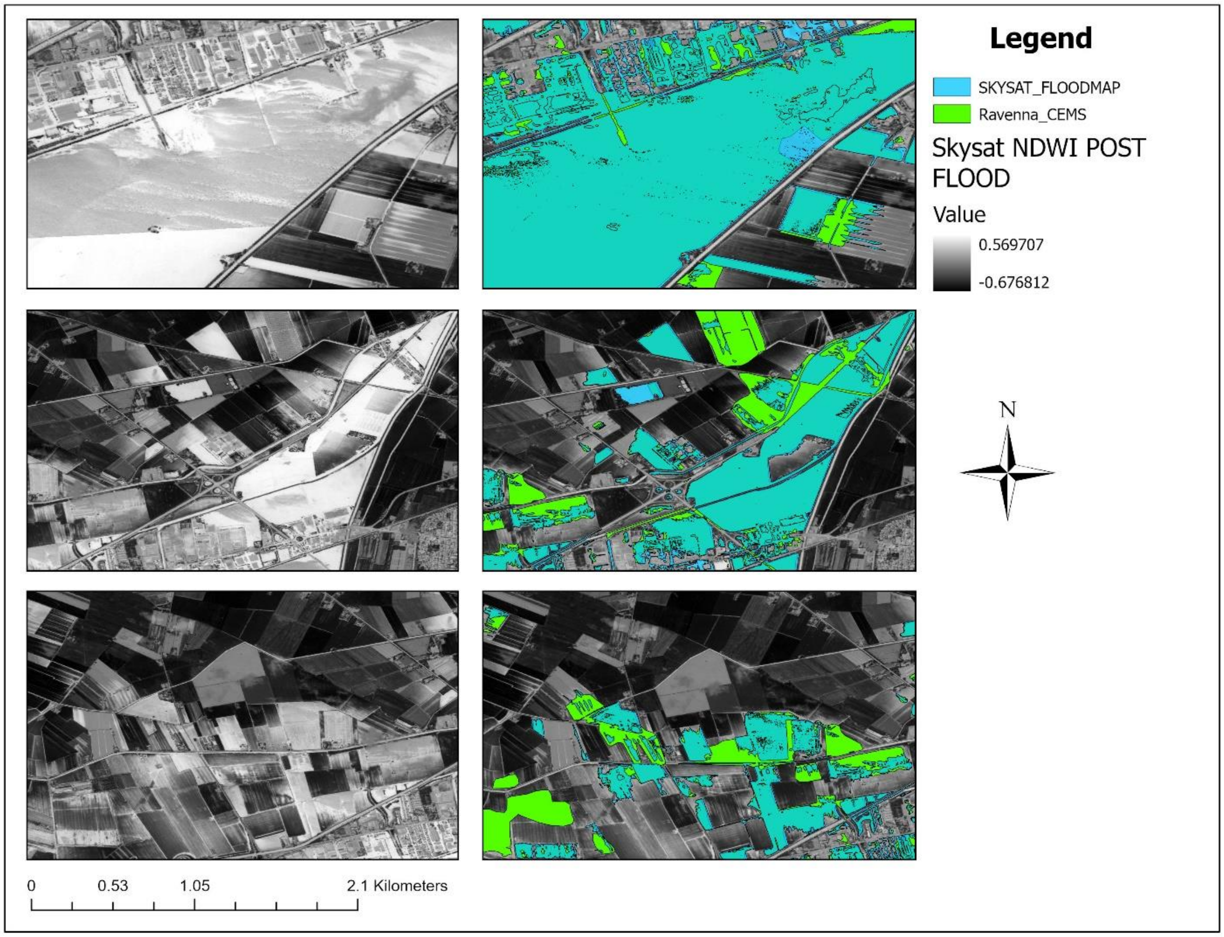

Figure 5-8: Visual comparison between the SkySat flood-extent map and the Copernicus Emergency Management Service (CEMS) of Ravenna province reference flood delineation, illustrating strong agreement and enhanced boundary detail captured by SkySat.

To further support visual validation, detailed views of the SkySat flood extent are provided in Figures 5-9 and 5-10. Figure 5-9 shows the flood mask overlaid on the NDWI post event background in an urban area, highlighting localized inundation between buildings and along narrow corridors. Figure 5-10 displays the same flood extent over the post-event SkySat optical image in a mixed vegetation and urban setting, allowing direct visual assessment of flood occurrence across different surface types.

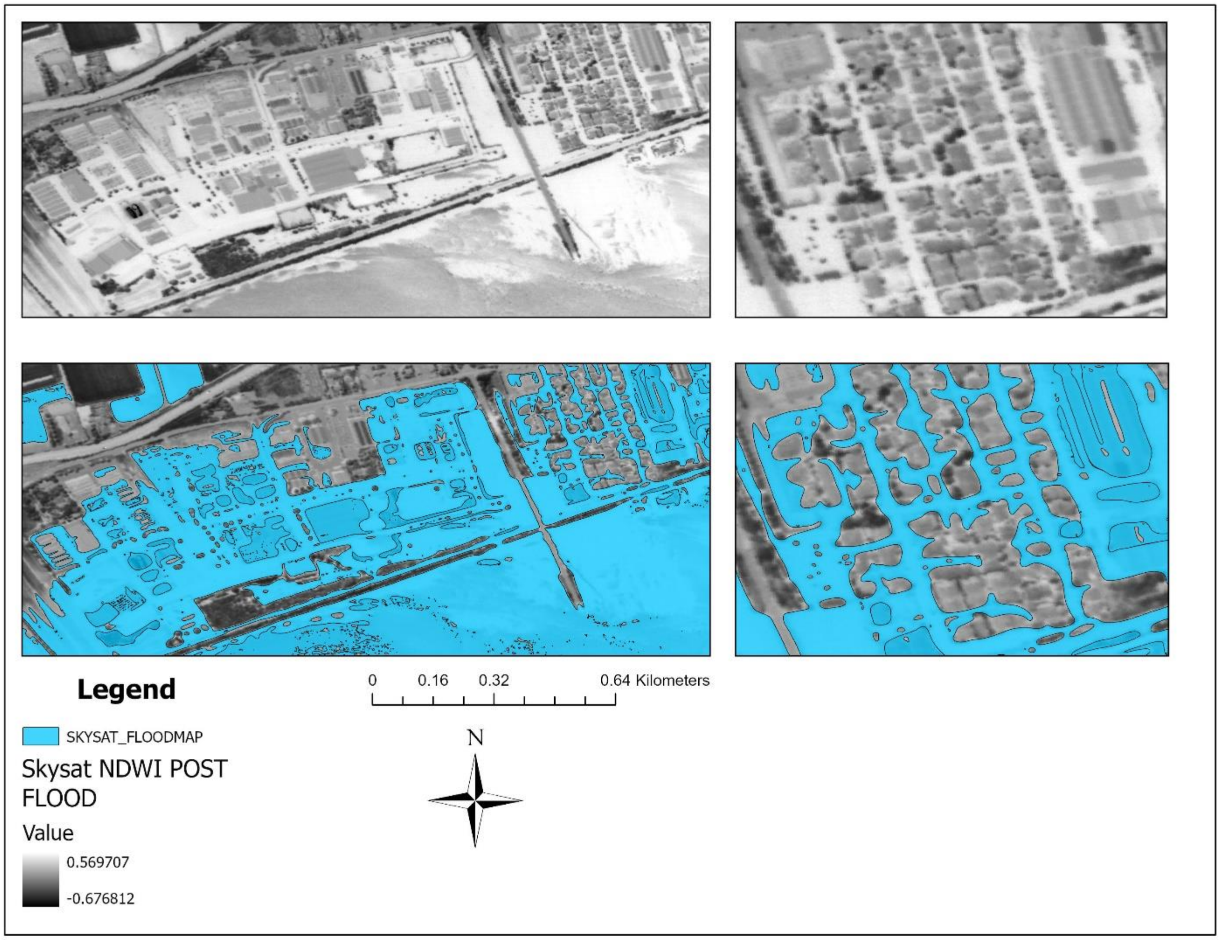

Figure 5-9: Detailed view of SkySat flood extent (NDWI ≥ 0.15) overlaid on the NDWI post event background in a built-up area, highlighting localized inundation between buildings and within urban blocks.

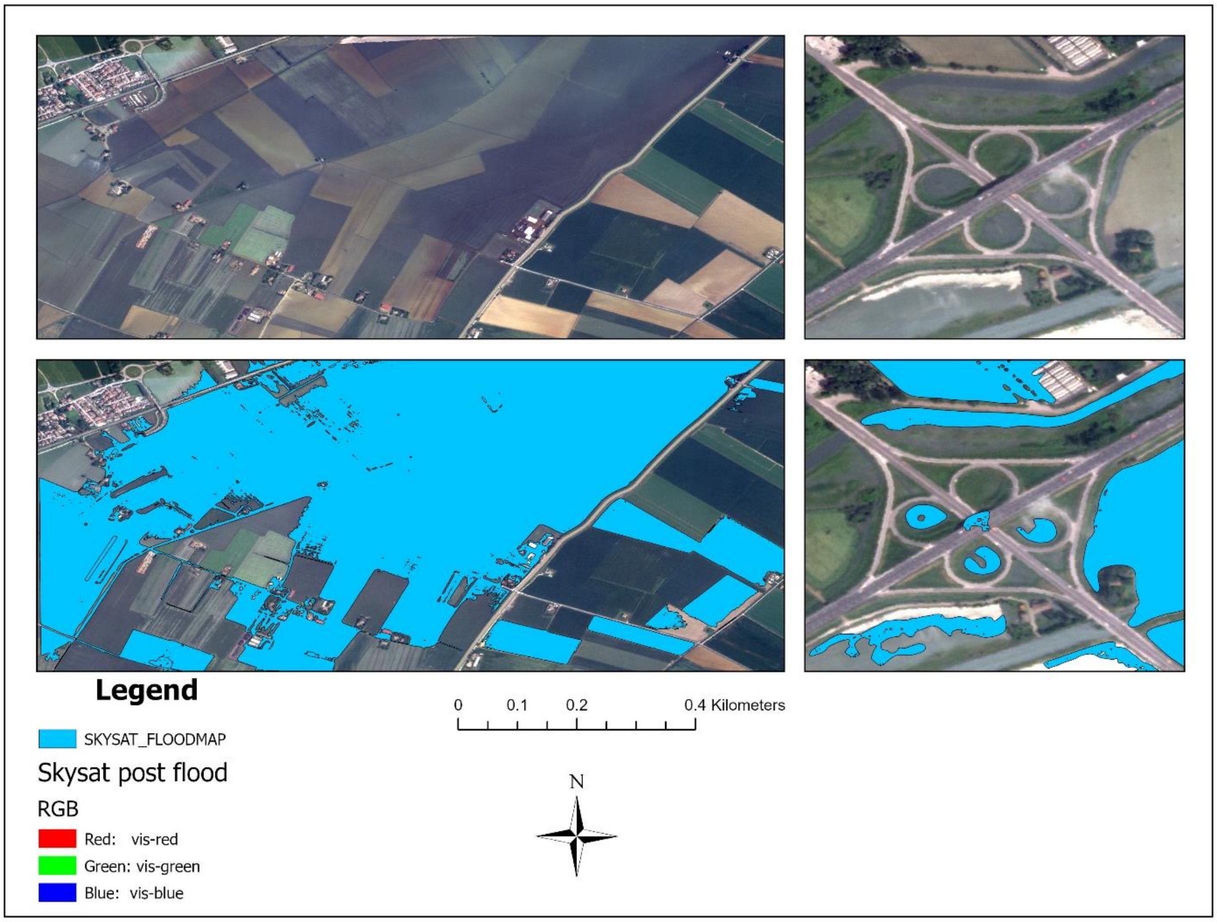

Figure 5-10: Detailed view of SkySat flood extent (NDWI ≥ 0.15) overlaid on the SkySat optical background in an area characterized by mixed vegetation and urban land cover, illustrating flood occurrence across different surface types.

Cross-sensor comparison against the CEMS reference delineation

Comparison of flood-extent maps derived from Sentinel-1, Sentinel-2, and SkySat reveals systematic differences in both the mapped inundation extent and the spatial representation of flooding when evaluated against the Copernicus Emergency Management Service (CEMS) reference delineation. Sentinel-1 produces the most conservative flood map, reliably capturing clearly inundated open areas while omitting a substantial fraction of flooding in vegetated, urban, and shallow-water environments. Sentinel-2 identifies a broader and more spatially continuous flood extent, reducing omission in floodplain margins and shallowly inundated zones under favorable atmospheric conditions. SkySat provides the most spatially detailed and exhaustive flood representation, resolving fine-scale inundation patterns and localized flooding that are generalized or not represented in medium-resolution products. Across all sensors, observed discrepancies with the CEMS reference are primarily controlled by sensor spatial resolution, observation modality, and land-cover complexity, rather than inconsistencies in flood mapping logic. These systematic differences motivate the quantitative accuracy assessment presented in the following section, where sensor performance is evaluated using confusion-matrix–based metrics.

4. Multi-sensor Accuracy Assessment and Comparative Analysis

The accuracy of flood-extent maps derived from Sentinel-1, Sentinel-2, and SkySat was quantitatively evaluated using the Copernicus Emergency Management Service (CEMS) Delineation Monitoring 3 (EMSR664) flood product as reference. The assessment was conducted in vector format, comparing sensor-derived flood polygons directly against the CEMS reference delineation. Sentinel-1 and Sentinel-2 flood extents were validated against the CEMS Delineation Monitoring 3 reference over the full available mapping domain for the study area. In contrast, SkySat validation was restricted to EMSR664 AOI07, which corresponds to the spatial footprint of the SkySat acquisition, due to its limited coverage relative to the full CEMS mapping extent. Accuracy metrics were derived from polygon-based confusion matrices, with emphasis placed on F1-score, Intersection over Union (IoU), and Cohen’s Kappa, which are particularly suitable for evaluating flood-extent agreement under class-imbalanced conditions.

Table 5-1 quantitative results of the accuracy assessment

Product	**FN**	**FP**	**TN**	**TP**	**F1**	**IoU**	**kappa**	**Overall Accuracy**	**Precision**	**Recall**	**Samples_n**
Sentinel 1	1709	60	4940	1597	0.64	0.47	0.51	0.79	0.96	0.48	10000
Sentinel 2	1285	79	4921	2021	0.75	0.6	0.63	0.84	0.96	0.61	10000
Skysat	1007	0	5000	3993	0.90	0.80	0.80	0.90	1	0.8	10000

The quantitative results reported in Table 5-1 highlight clear differences in flood-extent agreement across the evaluated sensors when validated against the CEMS Delineation Monitoring 3 (EMSR664) reference. Given the strong class imbalance between flooded and non-flooded areas, interpretation focuses primarily on F1-score, Intersection over Union (IoU), and Cohen’s Kappa, which provide a more informative measure of spatial agreement than overall accuracy alone.

- Sentinel-1 exhibits very high precision (0.96), indicating that areas classified as flooded are rarely false positives. However, recall is comparatively low (0.48), showing that a substantial portion of flooded areas present in the reference delineation is not captured. This imbalance results in a moderate F1-score of 0.64 and an IoU of 0.47, with a Cohen's Kappa of 0.51, indicating moderate spatial agreement. These results quantitatively reflect the conservative nature of Sentinel-1 flood mapping, characterized by limited commission errors but significant omission of flooded areas.
- Sentinel-2 demonstrates a more balanced detection behavior. Precision remains high (0.96), while recall increases to 0.61, indicating improved detection of flooded areas relative to Sentinel-1. This improvement is reflected in a higher F1-score of 0.75, an IoU of 0.60, and a Cohen's Kappa of 0.63, corresponding to substantial agreement with the reference delineation. The reduction in false negatives relative to Sentinel-1 indicates enhanced spatial completeness of the Sentinel-2 flood extent.
- SkySat achieves the highest agreement with the reference delineation among the evaluated products. The absence of false positives (FP = 0) results in perfect precision (1.00), while recall reaches 0.80, indicating that most flooded areas within the EMSR664 AOI07 domain are correctly identified. Consequently, SkySat attains an F1-score of 0.90, an IoU of 0.80, and a Cohen's Kappa of 0.80, reflecting strong spatial agreement with the reference flood delineation. These metrics confirm the ability of very-high-resolution imagery to capture detailed and spatially complete flood extents within its acquisition footprint.

Across all sensors, Overall Accuracy values range from 0.79 to 0.90, largely reflecting the dominance of non-flooded areas in the validation samples. This reinforces the need to prioritize F1-score, IoU, and Cohen's Kappa when comparing flood-extent performance across sensors.

5.2 FWDET-based Water-Depth Estimation

Floodwater depth and volume were estimated using the Flood Water Depth Estimation Tool (FWDET) applied to the binary flood extent derived from the optical flood mapping results. The FWDET outputs are analyzed by combining the same flood mask with topographic data at different spatial resolutions, including a 30 m DEM, a 5 m LiDAR-derived DTM, and a 0.5 m LiDAR-derived DTM. This comparison allows direct evaluation of how terrain resolution influences floodwater surface reconstruction, depth distribution, and total estimated flood volume. The discussion focuses on spatial depth patterns and quantitative differences among the datasets, highlighting the role of high-resolution topographic information in reducing artifacts and improving the physical realism of water-depth estimates.

1. FWDET results using DEM 30 m

When FWDET is applied using the 30 m resolution DEM, the resulting floodwater depth map (Figure 5-11) exhibits a spatially smooth water-surface reconstruction with limited representation of small-scale topographic variability. Due to the coarse resolution of the terrain input, local depressions and subtle elevation differences within the floodplain are not resolved, leading to generalized depth patterns over large areas. As a result, floodwater depth appears relatively uniform within broad inundated zones, and depth gradients near flood boundaries are gradual rather than sharply defined. The total floodwater volume estimated under this configuration is approximately 3.54 million cubic meters (Mm³). These characteristics reflect the influence of coarse topographic representation on FWDET outputs and provide a baseline for comparison with higher-resolution LiDAR-derived terrain datasets.

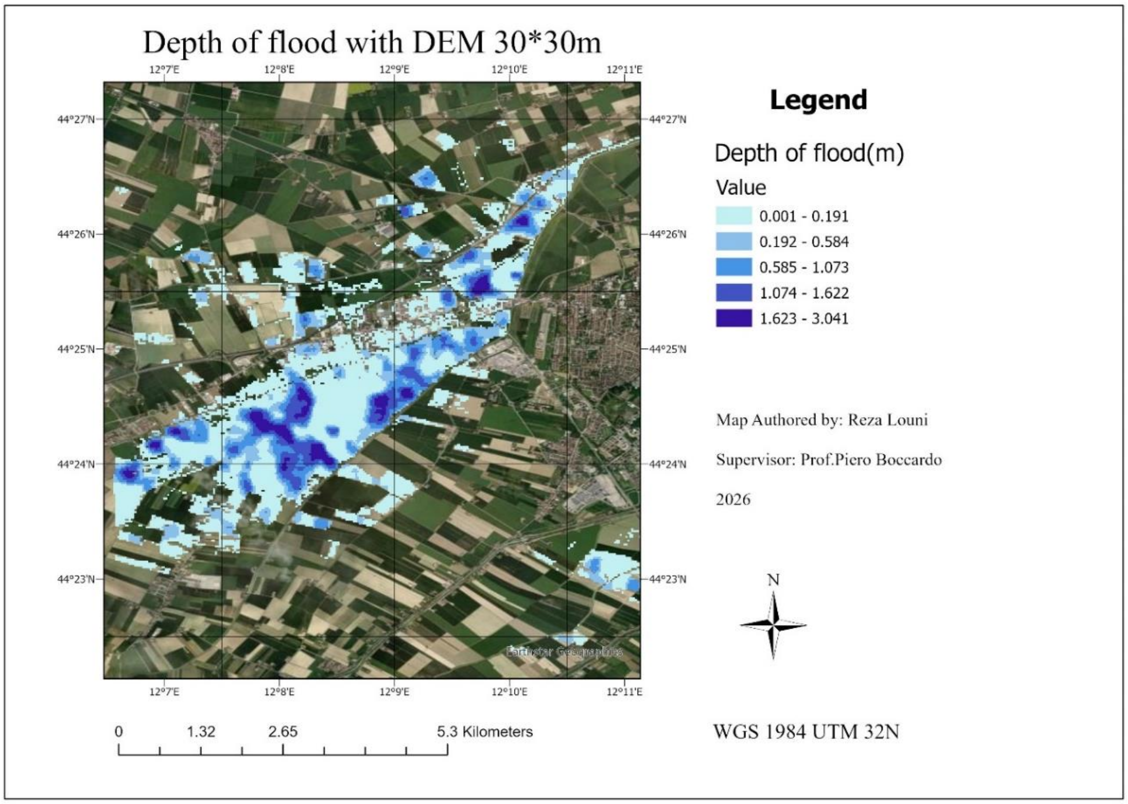

Figure 5-11: FWDET-derived floodwater depth map obtained using a 30 m resolution DEM as terrain input. The coarse topographic representation results in spatially smoothed depth patterns and a generalized floodwater surface reconstruction.

2. FWDET result with LiDAR DTM 5 m

When FWDET is applied using the 5 m resolution LiDAR-derived DTM, the resulting floodwater depth map (Figure 5-12) shows a markedly higher level of spatial detail compared to the 30 m DEM case. The finer terrain representation allows local depressions, drainage features, and subtle elevation gradients within the floodplain to be resolved, leading to more heterogeneous and spatially variable depth patterns. Depth gradients near flood boundaries appear sharper, and the reconstructed floodwater surface better follows the underlying topography. Under this configuration, the estimated total floodwater volume is approximately 1.66 million cubic meters (Mm³), substantially lower than the volume obtained with the coarser DEM. The observed differences in depth distribution and volume highlight the sensitivity of FWDET outputs to terrain resolution and illustrate the effect of incorporating higher-resolution LiDAR topographic data.

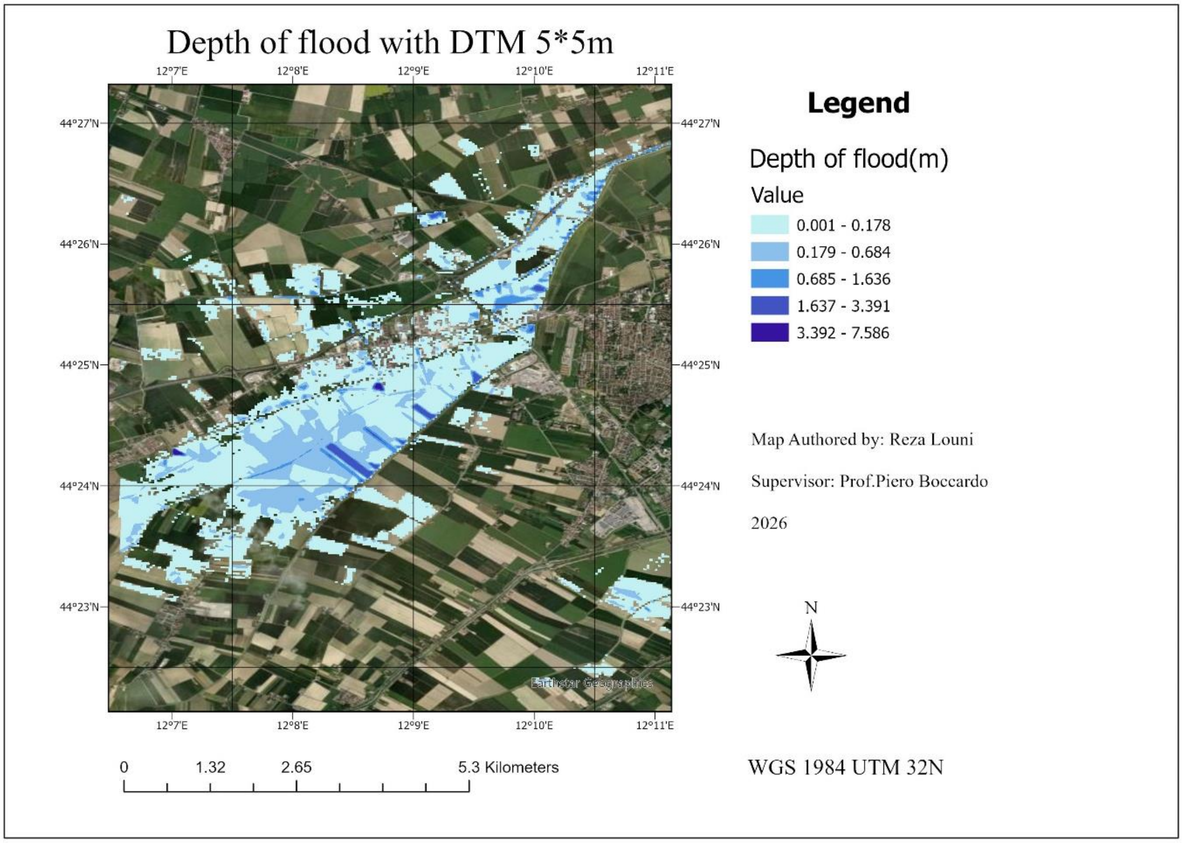

Figure 5-12: FWDET-derived floodwater depth map obtained using a 5 m resolution LiDAR DTM as terrain input. The higher-resolution topography enables improved representation of local terrain variability and more spatially heterogeneous depth patterns.

3. FWDET result with LiDAR DTM 0.5 m

When FWDET is applied using the 0.5 m resolution LiDAR-derived DTM, the resulting floodwater depth map (Figure 5-13) exhibits the highest level of spatial detail among the tested terrain datasets. The very-high-resolution topographic input allows fine-scale micro-topographic features, small depressions, and subtle elevation changes within the floodplain to be explicitly resolved, resulting in highly localized and spatially heterogeneous depth patterns. Flood boundaries are sharply defined, and the reconstructed floodwater surface closely follows the underlying terrain geometry. The total floodwater volume estimated under this configuration is approximately 1.64 million cubic meters (Mm³), which is very close to the value obtained using the 5 m DTM. This similarity indicates a convergence of volume estimates as terrain resolution increases, while differences in the depth maps primarily reflect increased spatial detail rather than large changes in total inundated volume.

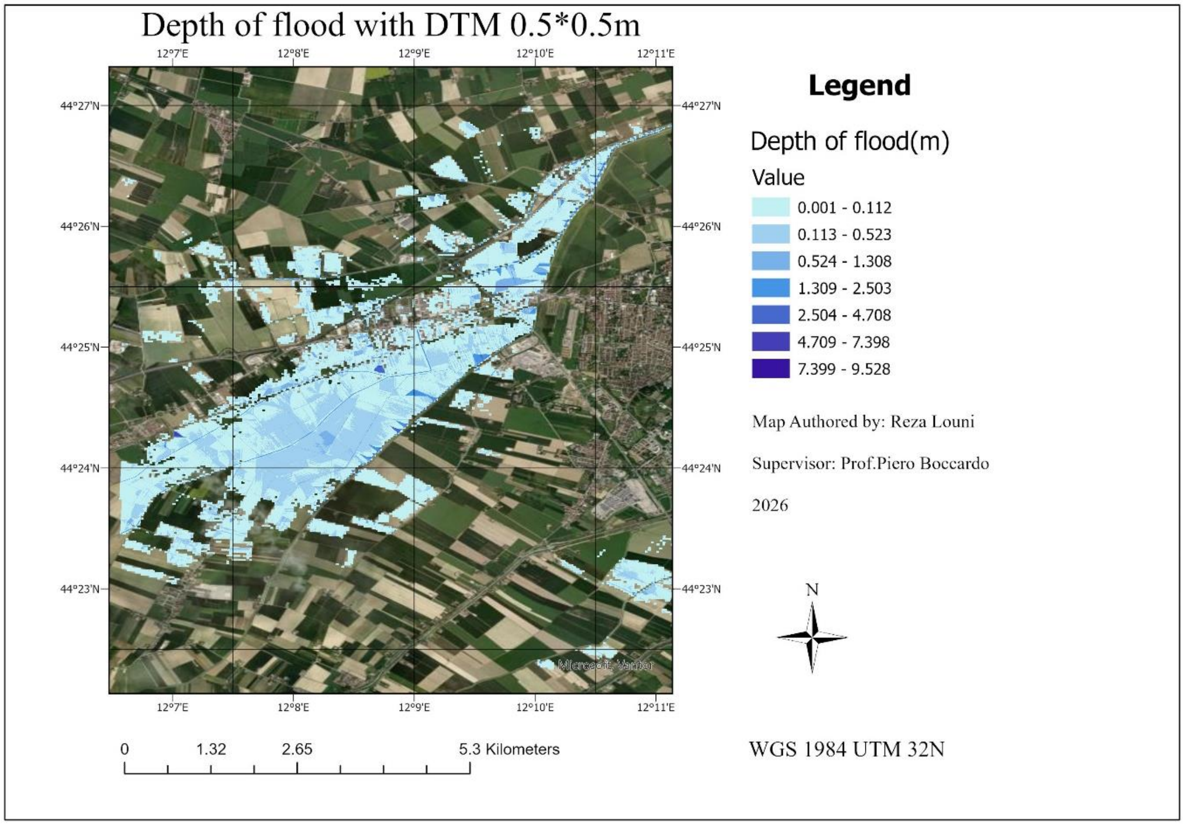

Figure 5-13: FWDET-derived floodwater depth map obtained using a 0.5 m resolution LiDAR DTM as terrain input. The very-high-resolution topography enables detailed representation of micro-topographic features and fine-scale floodwater depth variability.

Accuracy assessment of the floodwater depth result

Floodwater depth estimates derived from FWDET were quantitatively validated against the Copernicus Emergency Management Service EMSN154 water-depth product, which was adopted as the reference dataset. Validation was performed at locations where both FWDET-derived depth values and EMSN154 depths were available, and accuracy metrics were computed using Bias, Mean Absolute Error (MAE), and Root Mean Square Error (RMSE). These metrics allow assessment of systematic over- or underestimation as well as overall deviation between estimated and reference depths. The validation results for the three terrain configurations are summarized in Table 5-2.

Table 5-2 quantitative results of the flood depth accuracy assessment

Configuration	**Bias (m)**	**MAE (m)**	**RMSE (m)**	**Evaluation scale (m)**	**Valid pixels**	**Validation point**
DEM30m vs EMSN154	0.47	0.53	0.72	30	7549	364
DTM 5m vs EMSN154	0	0.31	0.54	5	167529	368
DTM 0.5m vs EMSN154	-0.07	0.25	0.44	0.5	19,514,028	392

- FWDET results using DEM 30 m

When FWDET is applied using the 30 m DEM, flood-depth estimates show a positive bias of 0.47 m, indicating systematic overestimation relative to the EMSN154 reference. The corresponding MAE of 0.53 m and RMSE of 0.72 m reflect relatively large deviations in estimated depth. These errors are associated with the coarse spatial representation of terrain, which smooths local depressions and flow pathways, leading to inflated water-surface reconstruction and exaggerated depth values. A total of 7,549 valid pixels and 364 validation points contributed to this assessment.

- FWDET results using LiDAR DTM 5 m

Using the 5 m LiDAR-derived DTM, flood-depth accuracy improves substantially. The bias is effectively zero, indicating the absence of systematic over- or underestimation. Error magnitudes decrease markedly, with an MAE of 0.31 m and an RMSE of 0.54 m, demonstrating improved agreement with the EMSN154 reference depths. The finer terrain representation enables a more realistic reconstruction of floodwater surfaces by capturing local elevation variability within the floodplain. This configuration was validated using 16,7529 valid pixels and 368 validation points.

- FWDET results using LiDAR DTM 0.5 m

The 0.5 m LiDAR-derived DTM yields the highest overall accuracy among the evaluated configurations. Flood-depth estimates show a slight negative bias of 0.07 m, indicating minimal underestimation relative to the reference. Error metrics further decrease to an MAE of 0.25 m and an RMSE of 0.44 m, reflecting the most accurate depth reconstruction. The very-high-resolution terrain allows FWDET to resolve micro-topographic features and subtle elevation gradients that strongly control local floodwater depth. Validation in this configuration was supported by 19,514,028 valid pixels and 392 validation points, providing robust statistical support for the results.

Comparative assessment of terrain configurations and limitations

Across all configurations, flood-depth accuracy improves systematically with increasing terrain resolution. The transition from a coarse DEM to LiDAR-derived DTMs results in reduced bias and substantial decreases in MAE and RMSE. While the largest improvement occurs between the 30 m DEM and the 5 m DTM, further refinement to 0.5 m resolution yields additional reductions in error magnitude and bias, primarily enhancing local depth accuracy rather than introducing large changes in overall depth magnitude. These results demonstrate the dominant influence of terrain resolution on FWDET-based flood-depth estimation accuracy.

5.3 Implications of the findings for regional flood-risk assessment

The results discussed earlier have direct implications for regional flood-risk assessment, especially regarding the reliability of flood characterization under different data and resolution scenarios. The observed differences in flood extent detection and water depth estimation highlight how sensor characteristics and terrain representation impact the spatial depiction of inundation processes in low-lying and heterogeneous landscapes. Comparing flood-extent maps shows that different satellite sensors capture complementary aspects of flooding. SAR-based observations offer consistent flood detection under adverse weather conditions, ensuring continuous flood monitoring when optical imagery is limited. Optical sensors are more sensitive to shallow and continuous inundation where clear skies are available, improving flood boundary delineation in agricultural and peri-urban areas. Very-high-resolution imagery further improves the depiction of inundation in complex environments, especially in urban and mixed land-cover settings, where flooding occurs at fine spatial scales that medium-resolution sensors cannot resolve. These differences influence the identification of exposed areas and the distribution of flood impacts across land-use types. The FWDET-based water-depth estimates demonstrate the significant effect of terrain resolution on reconstructed floodwater surfaces and volume calculations. Coarser elevation data produce smoother depth profiles and larger volume estimates due to generalized terrain representations, while LiDAR-derived DTMs enable a more detailed reconstruction of depth variations by capturing local depressions and subtle elevation gradients. The convergence of floodwater volume estimates between the 5 m and 0.5 m DTMs shows that higher terrain resolutions have reduced impact on volumetric results, while differences in depth maps mainly reflect increased spatial detail rather than changes in overall inundation extent. Overall, these findings show that flood-extent and water-depth products are highly influenced by sensor type and terrain resolution. Combining multi-sensor flood mapping with FWDET-based depth estimation offers a consistent framework for understanding how data choice affects flood process representation at regional scales, supporting better interpretation of flood products derived from satellite data and topographic information.

Chapter6: Conclusions and further developments

6.1 Conclusions

This study addressed two central research questions: first, how effectively different satellite sensors can map flood extent in complex flood-prone environments, and second, how terrain resolution influences the reliability of satellite-based floodwater depth and volume estimation. Through a systematic evaluation of flood-extent products derived from SAR, optical, and very-high-resolution imagery, together with an analysis of FWDET-based floodwater depth estimates using elevation data at multiple spatial resolutions, the research provides a structured assessment of satellite-based flood characterization approaches within an emergency management context. With respect to flood-extent mapping, the results demonstrate that sensor modality and spatial resolution exert a strong control on the representation of inundation. SAR-based flood mapping provides robust and reliable detection of clearly inundated open areas under all weather conditions, supporting timely flood monitoring during emergencies. However, this robustness is accompanied by reduced spatial completeness in vegetated, urban, and shallowly flooded environments. Optical imagery improves flood delineation where atmospheric conditions permit, enabling a more continuous representation of inundation and better identification of marginally flooded areas. Very-high-resolution imagery further enhances flood mapping by resolving fine-scale inundation patterns and complex flooding dynamics in heterogeneous landscapes, particularly within urban and peri-urban environments. These findings clarify how different satellite sensors contribute complementary information and support distinct phases and information needs within flood emergency management workflows. Regarding floodwater depth and volume estimation, the FWDET analysis shows that terrain resolution is a dominant factor controlling the reliability and spatial realism of reconstructed floodwater surfaces. Coarse elevation models tend to smooth local topographic variability, leading to generalized water-surface representations and inflated estimates of flood severity. In contrast, high-resolution LiDAR-derived digital terrain models enable more accurate representation of floodplain morphology and local elevation gradients, improving the consistency and physical realism of depth estimates. As terrain resolution increases, depth reconstruction becomes increasingly controlled by local topography rather than grid discretization, resulting in more stable and spatially coherent floodwater representations.

Overall, the results demonstrate that effective emergency flood mapping depends on the combined consideration of sensor characteristics and terrain representation. Comparative evaluation of satellite-derived flood-extent products highlights the strengths and limitations of different sensors for operational use, while FWDET-based depth analysis emphasizes the critical role of high-quality topographic data for reliable flood severity characterization. Together, these findings provide a scientifically grounded basis for interpreting satellite-derived flood information used in emergency response, post-event damage assessment, and flood-risk analysis.

6.2 Further Developments

Future developments building on this work could primarily focus on extending the proposed evaluation framework to a broader set of flood events and geographic contexts. Applying the same multi-sensor flood-extent comparison and FWDET-based depth analysis across different hydrological regimes, landscape types, and degrees of urbanization would allow assessment of the robustness and transferability of the findings. Additional work could investigate the sensitivity of flood-extent and flood-depth results to key methodological choices, such as flood-extent delineation strategies, terrain preprocessing, and representation of complex surface conditions. Such analyses would help clarify the extent to which the observed differences are event-specific or systematic across different flood scenarios. Finally, further integration of multi-sensor satellite observations within operational emergency mapping workflows could improve consistency and interpretability of flood products used for post-event assessment. In this context, the combined use of SAR, optical, and very-high-resolution imagery offers a practical pathway for balancing robustness, spatial detail, and data availability in real-world flood monitoring applications.

References:

Aati, S., & Avouac, J. P. (2020). Optimization of optical image geometric modeling, application to topography extraction and topographic change measurements using planetscope and skysat imagery. *Remote Sensing*, *12*(20), 1–25. https://doi.org/10.3390/rs12203418

Ahmad, R., Abdul Maulud, K. N., Bin Zamir, U., Mohd Razali, S. F., Yaseen, Z. M., Pradhan, B., Khan, M. N., & Eshquvvatov, B. (2025). A systematic literature review of digital elevation models and hydrological models integration for advanced flood risk management. In *Geomatics, Natural Hazards and Risk* (Vol. 16, Number 1). Taylor and Francis Ltd. https://doi.org/10.1080/19475705.2025.2549487

Ahmed, R. U., Rashid, M. M., Biswas, N. K., & Sharma, S. (2025). Flood Mapping from Satellite Imagery: A Response-Based Framework for Quantifying Flood Hazard and Uncertainty. *Earth Systems and Environment*. https://doi.org/10.1007/s41748-025-00862-1

Bates, P. D., Quinn, N., Sampson, C., Smith, A., Wing, O., Sosa, J., Savage, J., Olcese, G., Neal, J., Schumann, G., Giustarini, L., Coxon, G., Porter, J. R., Amodeo, M. F., Chu, Z., Lewis-Gruss, S., Freeman, N. B., Houser, T., Delgado, M., … Krajewski, W. F. (2021). Combined Modeling of US Fluvial, Pluvial, and Coastal Flood Hazard Under Current and Future Climates. *Water Resources Research*, *57*(2). https://doi.org/10.1029/2020WR028673

Bentivoglio, R., Isufi, E., Jonkman, S. N., & Taormina, R. (2022). Deep learning methods for flood mapping: a review of existing applications and future research directions. In *Hydrology and Earth System Sciences* (Vol. 26, Number 16, pp. 4345–4378). Copernicus GmbH. https://doi.org/10.5194/hess-26-4345-2022

Betterle, A., & Salamon, P. (2024). Water depth estimate and flood extent enhancement for satellite-based inundation maps. *Natural Hazards and Earth System Sciences*, *24*(8), 2817–2836. https://doi.org/10.5194/nhess-24-2817-2024

Bryant, S., McGrath, H., & Boudreault, M. (2022). Gridded flood depth estimates from satellite-derived inundations. *Natural Hazards and Earth System Sciences*, *22*(4), 1437–1450. https://doi.org/10.5194/nhess-22-1437-2022

CEMS. (2023). *Copernicus EMS Risk & Recovery Mapping Technical Report FRAMEWORK SERVICE CONTRACT FOR COPERNICUS EMERGENCY MANAGEMENT SERVICE RISK & RECOVERY MAPPING Copernicus EMS Risk & Recovery Mapping Technical Report*.

Chai, T., & Draxler, R. R. (2014). Root mean square error (RMSE) or mean absolute error (MAE)? -Arguments against avoiding RMSE in the literature. *Geoscientific Model Development*, *7*(3), 1247–1250. https://doi.org/10.5194/gmd-7-1247-2014

Chen, Z., & Zhao, S. (2022). Automatic monitoring of surface water dynamics using Sentinel-1 and Sentinel-2 data with Google Earth Engine. In *International Journal of Applied Earth Observation and Geoinformation* (Vol. 113). Elsevier B.V. https://doi.org/10.1016/j.jag.2022.103010

Cohen, S., Brakenridge, G. R., Kettner, A., Bates, B., Nelson, J., McDonald, R., Huang, Y. F., Munasinghe, D., & Zhang, J. (2018). Estimating Floodwater Depths from Flood Inundation Maps and Topography. *Journal of the American Water Resources Association*, *54*(4), 847–858. https://doi.org/10.1111/1752-1688.12609

Cohen, S., Peter, B. G., Haag, A., Munasinghe, D., Moragoda, N., Narayanan, A., & May, S. (2022). Sensitivity of Remote Sensing Floodwater Depth Calculation to Boundary Filtering and Digital Elevation Model Selections. *Remote Sensing*, *14*(21). https://doi.org/10.3390/rs14215313

Composto, R. W., Tulbure, M. G., Tiwari, V., Gaines, M. D., & Caineta, J. (2025). Quantifying urban flood extent using satellite imagery and machine learning. *Natural Hazards*, *121*(1), 175–199. https://doi.org/10.1007/s11069-024-06817-5

Cort J. Willmott, K. M. (2005). *Advantages of the mean absolute error (MAE) over the root mean square error (RMSE) in assessing average model performance*. www.int-res.com

D. N. Moriasi, J. G. A. M. W. V. L. R. L. B. R. D. H. T. L. V. (2007). Model evaluation guidelines for systematic quantification of accuracy in watershed simulations. *American Society of Agricultural and Biological Engineers*.

Das, P., Jensen, K., De, S., & Ganguly, A. R. (2023). Flood Depth Estimation Using Synthetic Aperture Radar (SAR) Imagery and Topography: A Case Study of the 2021 and 2022 Floods in Hawkesbury Valley, Australia. *International Geoscience and Remote Sensing Symposium (IGARSS)*, *2023-July*, 2402–2405. https://doi.org/10.1109/IGARSS52108.2023.10282474

DeVries, B., Huang, C., Armston, J., Huang, W., Jones, J. W., & Lang, M. W. (2020). Rapid and robust monitoring of flood events using Sentinel-1 and Landsat data on the Google Earth Engine. *Remote Sensing of Environment*, *240*. https://doi.org/10.1016/j.rse.2020.111664

EEA. (2023). *https://www.eea.europa.eu/en/analysis/publications/eea-signals-2023-health-and-environment-in-europe*. https://www.eea.europa.eu/en/analysis/publications/eea-signals-2023-health-and-environment-in-europe

ESA. (2024). *COPERNICUS SPACE COMPONENT DATA ACCESS PORTFOLIO: DATA WAREHOUSE 2024 CHANGE LOG Copernicus Contributing Mission Activity: Data Access Portfolio for 2024 Issue Nr Revision Number Date*.

Esposito, G., & Ravanelli, R. (2024). *L'ALLUVIONE DI MAGGIO 2023 IN EMILIA-ROMAGNA: MONITORAGGIO DELLE COLTURE CON IMMAGINI SATELLITARI*.

Farhadi, H., Ebadi, H., Kiani, A., & Asgary, A. (2024a). A novel flood/water extraction index (FWEI) for identifying water and flooded areas using sentinel-2 visible and near-infrared spectral bands. *Stochastic Environmental Research and Risk Assessment*, *38*(5), 1873–1895. https://doi.org/10.1007/s00477-024-02660-z

Farhadi, H., Ebadi, H., Kiani, A., & Asgary, A. (2024b). Near Real-Time Flood Monitoring Using Multi-Sensor Optical Imagery and Machine Learning by GEE: An Automatic Feature-Based Multi-Class Classification Approach. *Remote Sensing*, *16*(23). https://doi.org/10.3390/rs16234454

Farr, T. G., Rosen, P. A., Caro, E., Crippen, R., Duren, R., Hensley, S., Kobrick, M., Paller, M., Rodriguez, E., Roth, L., Seal, D., Shaffer, S., Shimada, J., Umland, J., Werner, M., Oskin, M., Burbank, D., & Alsdorf, D. E. (2007). The shuttle radar topography mission. *Reviews of Geophysics*, *45*(2). https://doi.org/10.1029/2005RG000183

Foody, G. M. (2020). Explaining the unsuitability of the kappa coefficient in the assessment and comparison of the accuracy of thematic maps obtained by image classification. *Remote Sensing of Environment*, *239*. https://doi.org/10.1016/j.rse.2019.111630

Gašparovič, M., & Klobučar, D. (2021). Mapping floods in lowland forest using sentinel-1 and sentinel-2 data and an object-based approach. *Forests*, *12*(5). https://doi.org/10.3390/f12050553

Ghouri, A. Y., ur Rehman, A., Rasheed, F., Miandad, M., & Rehman, G. (2024). Flood Mapping Using the Sentinel-1 SAR Dataset and Application of the Change Detection Approach Technique (CDAT) to the Google Earth Engine In Sindh Province, Pakistan. *Ecological Questions*, *35*(2). https://doi.org/10.12775/EQ.2024.024

Gorelick, N., Hancher, M., Dixon, M., Ilyushchenko, S., Thau, D., & Moore, R. (2017). Google Earth Engine: Planetary-scale geospatial analysis for everyone. *Remote Sensing of Environment*, *202*, 18–27. https://doi.org/10.1016/j.rse.2017.06.031

Hamidi, E., Peter, B. G., Munoz, D. F., Moftakhari, H., & Moradkhani, H. (2023). Fast Flood Extent Monitoring With SAR Change Detection Using Google Earth Engine. *IEEE Transactions on Geoscience and Remote Sensing*, *61*. https://doi.org/10.1109/TGRS.2023.3240097

Johansen, K., Dunne, A. F., Tu, Y. H., Jones, B. H., & McCabe, M. F. (2022). Monitoring coastal water flow dynamics using sub-daily high-resolution SkySat satellite and UAV-based imagery. *Water Research*, *219*. https://doi.org/10.1016/j.watres.2022.118531

Kussul, N., Drozd, S., Skakun, S., Duncan, E., & Becker-Reshef, I. (2023). Fusion of very high and moderate spatial resolution satellite data for detection and mapping of damages in agricultural fields. *2023 13th International Conference on Dependable Systems, Services and Technologies, DESSERT 2023*. https://doi.org/10.1109/DESSERT61349.2023.10416533

Lan, L., & Wang, X. (2025). Large-scale flood mapping using Sentinel-1 and Sentinel-2 imagery: Spatio-temporal analysis of the 23·7 Haihe basin-wide extreme flood. *Journal of Hydrology*, *653*. https://doi.org/10.1016/j.jhydrol.2025.132777

Liou, Y. A., & Hoang, D. V. (2024). Improved flood depth estimation with SAR image, digital elevation model, and machine learning schemes. *Journal of Hydrology: Regional Studies*, *53*. https://doi.org/10.1016/j.ejrh.2024.101775

Liu, Y., Zhang, H., Zhang, M., Cui, Z., Lei, K., Zhang, J., Yang, T., & Ji, P. (2022). Vietnam wetland cover map: using hydro-periods Sentinel-2 images and Google Earth Engine to explore the mapping method of tropical wetland. *International Journal of Applied Earth Observation and Geoinformation*, *115*. https://doi.org/10.1016/j.jag.2022.103122

Mai Sy, H., Luu, C., Bui, Q. D., Ha, H., & Nguyen, D. Q. (2023). Urban flood risk assessment using Sentinel-1 on the google earth engine: A case study in Thai Nguyen city, Vietnam. *Remote Sensing Applications: Society and Environment*, *31*. https://doi.org/10.1016/j.rsase.2023.100987

Mehmood, H., Conway, C., & Perera, D. (2021). Mapping of flood areas using landsat with google earth engine cloud platform. *Atmosphere*, *12*(7). https://doi.org/10.3390/atmos12070866

Meyer, R. P., Søgaard, M. G., Schødt, M. P., Horion, S., & Prishchepov, A. V. (2022). *EMERGENCY FLOOD MAPPING IN AUSTRALIA WITH SENTINEL-1 AND SENTINEL-2 SATELLITE IMAGERY CARTOGRAPHIE D'URGENCE DES INONDATIONS EN AUSTRALIE À PARTIR D'IMAGES SATELLITAIRES SENTINEL-1 ET SENTINEL-2* (Vol. 78). https://kurser.

Moharrami, M., Javanbakht, M., & Attarchi, S. (2021). Automatic flood detection using sentinel-1 images on the google earth engine. *Environmental Monitoring and Assessment*, *193*(5). https://doi.org/10.1007/s10661-021-09037-7

R. G. Congalton. (1988). A comparison of sampling schemes used in generating error matrices for assessing the accuracy of maps generated from remotely sensed data. *PE&RS, Photogrammetric Engineering & Remote Sensing*.

Russell G. Congalton. (1991). A review of assessing the accuracy of classifications of remotely sensed data. *Remote Sensing of Environment*, *37*(1), 35–46.

Sathyanarayanan, S. (2024). Confusion Matrix-Based Performance Evaluation Metrics. *African Journal of Biomedical Research*, 4023–4031. https://doi.org/10.53555/ajbr.v27i4s.4345

Shan, W., Liu, J., & Guo, Y. (2025). Rapid Flood Mapping and Disaster Assessment Based on GEE Platform: Case Study of a Rainstorm from July to August 2024 in Liaoning Province, China. *Water (Switzerland)*, *17*(16). https://doi.org/10.3390/w17162416

S.K.McFEETERS. (1996). The use of the Normalized Difference Water Index (NDWI) in the delineation of open water features. *International Journal of Remote Sensing*.

Slagter, B., Tsendbazar, N. E., Vollrath, A., & Reiche, J. (2020). Mapping wetland characteristics using temporally dense Sentinel-1 and Sentinel-2 data: A case study in the St. Lucia wetlands, South Africa. *International Journal of Applied Earth Observation and Geoinformation*, *86*. https://doi.org/10.1016/j.jag.2019.102009

Soria-Ruiz, J., Fernandez-Ordoñez, Y. M., Ambrosio-Ambrosio, J. P., Escalona-Maurice, M. J., Medina-García, G., Sotelo-Ruiz, E. D., & Ramirez-Guzman, M. E. (2022). Flooded Extent and Depth Analysis Using Optical and SAR Remote Sensing with Machine Learning Algorithms. *Atmosphere*, *13*(11). https://doi.org/10.3390/atmos13111852

Suab, S. A., Supe, H., Avtar, R., Dambul, R., & Chen, X. (2022). Detection and mapping of May 2021 flood in Beaufort, Sabah using Sentinel-1 SAR and Sentinel-2 multispectral in Google Earth Engine. *IOP Conference Series: Earth and Environmental Science*, *1064*(1). https://doi.org/10.1088/1755-1315/1064/1/012003

Szabó, L., Abriha, D., Phinzi, K., & Szabó, S. (2021). Urban vegetation classification with high-resolution PlanetScope and SkySat multispectral imagery. *Landscape & Environment*, *15*(1), 66–75. https://doi.org/10.21120/le/15/1/9

Teng, J., Penton, D. J., Ticehurst, C., Sengupta, A., Freebairn, A., Marvanek, S., Vaze, J., Gibbs, M., Streeton, N., Karim, F., & Morton, S. (2022a). A Comprehensive Assessment of Floodwater Depth Estimation Models in Semiarid Regions. *Water Resources Research*, *58*(11). https://doi.org/10.1029/2022WR032031

Teng, J., Penton, D. J., Ticehurst, C., Sengupta, A., Freebairn, A., Marvanek, S., Vaze, J., Gibbs, M., Streeton, N., Karim, F., & Morton, S. (2022b). A Comprehensive Assessment of Floodwater Depth Estimation Models in Semiarid Regions. *Water Resources Research*, *58*(11). https://doi.org/10.1029/2022WR032031

Tran, T. P., & Nguyen, D. L. (2025). Flood Inundation Assessment on Agricultural Land: Integrating High Spatial Resolution Sentinel Data with LiDAR DEM. *International Journal of Geoinformatics*, *21*(3), 71–81. https://doi.org/10.52939/ijg.v21i3.3997

Tripathy, P., & Malladi, T. (2022). Global Flood Mapper: a novel Google Earth Engine application for rapid flood mapping using Sentinel-1 SAR. *Natural Hazards*, *114*(2), 1341–1363. https://doi.org/10.1007/s11069-022-05428-2

Vanama, V. S. K., Mandal, D., & Rao, Y. S. (2020). GEE4FLOOD: rapid mapping of flood areas using temporal Sentinel-1 SAR images with Google Earth Engine cloud platform. *Journal of Applied Remote Sensing*, *14*(03), 1. https://doi.org/10.1117/1.jrs.14.034505

Vekaria, D., Chander, S., Singh, R. P., & Dixit, S. (2023). A change detection approach to flood inundation mapping using multi-temporal Sentinel-1 SAR images, the Brahmaputra River, Assam (India): 2015–2020. *Journal of Earth System Science*, *132*(1). https://doi.org/10.1007/s12040-022-02020-x

Wedajo, G. K. (2017). LiDAR DEM Data for Flood Mapping and Assessment; Opportunities and Challenges: A Review. *Journal of Remote Sensing & GIS*, *06*(04). https://doi.org/10.4172/2469-4134.1000211

Xu. (2006). Modification of normalised difference water index (NDWI) to enhance open water features in remotely sensed imagery. *International Journal of Remote Sensing* .

Yamazaki, D., Ikeshima, D., Tawatari, R., Yamaguchi, T., O'Loughlin, F., Neal, J. C., Sampson, C. C., Kanae, S., & Bates, P. D. (2017). A high-accuracy map of global terrain elevations. *Geophysical Research Letters*, *44*(11), 5844–5853. https://doi.org/10.1002/2017GL072874